

A STUDY OF ATMOSPHERIC NEUTRINOS  
AT SUPER-KAMIOKANDE

A DISSERTATION SUBMITTED TO THE GRADUATE DIVISION OF THE  
UNIVERSITY OF HAWAII IN PARTIAL FULFILLMENT OF THE  
REQUIREMENTS FOR THE DEGREE OF

DOCTOR OF PHILOSOPHY

IN

PHYSICS

DECEMBER 1997

By

John W. Flanagan

Dissertation Committee:

John G. Learned, Chair

Stephen L. Olsen

Sandip Pakvasa

L. Thomas Ramsey

Klaus Sattler

We certify that we have read this dissertation and that, in our opinion, it is satisfactory in scope and quality as a dissertation for the degree of Doctor of Philosophy in Physics.

DISSERTATION COMMITTEE

---

Chairperson

---

---

---

---

---

# Acknowledgments

Support for this dissertation came from many sources, the first of which is the author's advisor, John Learned, whose intuition and creativity in the understanding of what is important in a physics analysis and how to get at it has been an inspiration. In addition, he care for, and enthusiastically promotes, his students. The author has also benefited from the insight, support and patience of his other thesis committee members: S. Pakvasa, S. Olsen, K. Sattler and T. Ramsey. In addition, the author benefited from discussions with S. Matsuno, and V. Stenger's healthy dose of skepticism.

This dissertation and the experiment on which it is based is highly dependent on the hard work and diligence of the many members of the Super-Kamiokande collaboration. The construction, operation and analysis of data from this detector has been, and continues to be, an enormous effort involving the participation of many universities in the US, Japan, and Poland, and the list of people to whom the author is indebted is too large to exhaustively list, and the author must apologize to anyone inadvertently omitted.

The leadership for the experiment has come from Y. Totsuka (U. Tokyo), and from H. Sobel (UCI) and J. Stone (BU), who speak for the US institutions.

During the period of construction, B. Kropp of UCI was a forceful and caring leader without whom it would be difficult to imagine the outer detector having been completed on time. His dedication to the job and to his crew got us through a year-long period of seemingly continuous crisis, without anybody getting hurt. He and H. Sobel also gave the author and other non-UCI people on-site whatever material support was needed to get the job done. J. Stone came through with assistance and support in time of difficulties with the laser calibration hardware.

During analysis, the heads of the high-energy analysis groups deserve credit for organizing the geographically spread-out members of the group: T. Kajita of the

onsite group, and E. Kearns and T. Haines of the offsite group. E. Kearns has been especially helpful to the author, having hosted the author at BU for a month during analysis, and providing guidance through the preparation for the author's first public talk on the experiment. All other members of the offsite high-energy analysis group deserve special mention as well: M. Messier, B. Viren, K. Scholberg, T. Barsczak, C. Mauger, W. Gajewski, D. Kielczewska, C.K. Jung, C. Yanagisawa, E. Sharkey, M. Earl, A. Habig, and especially C. McGrew, who was responsible for most of the backbone of the reduction.

M. Nakahata of U. Tokyo has been a dedicated leader of the calibration group. Z. Conner was a strong partner in the construction of the laser calibration system, as was R. Sanford, who along with W. Gajewski also spent a lot of time on the calibration of the outer detector. M. Rosen provided expertise in laser optics. J. George and L. Wai worked inhumanly long hours on the outer-detector DAQ. Many others should not be forgotten, among them J. Hsu Svoboda, whose efforts were critical during construction, as were those of M. Vagins. R. Svoboda gave wise advice on analysis matters, even if it wasn't always heeded. Mr. Shimoi of the Kamioka Mining Company provided much practical assistance during construction.

J. Bruce took excellent care of many an administrative mess throughout the duration of the author's tenure on the experiment. A. Kibayashi helped the author out of a time jam as the defense deadline approached.

The author's parents, John and JoAnn, have always been there for the author, even as has gradually migrated further and further across the planet from them. Eventually, he will circle around

Finally, and most importantly, has been the loving support of Mika Masuzawa, who as colleague, friend and wife has taught the author some of the most important lessons that the author has learned. (Such as, it is wiser not to schedule a wedding and thesis defense within one week of each other.) Her support and understanding greatly aided the completion of this thesis.

This experiment is made possible with the cooperation and assistance of the Kamioka Mining Company (Kamioka Kougyou K.K.). This work was supported in part by the U.S. Department of Energy (DOE) and the Japanese Ministry of Education, Science, Sports and Culture (Monbusho).

# Abstract

Several measurements of atmospheric neutrino-induced events in the range  $\sim 0.1$  to  $\sim 1$  GeV have found a smaller than expected number of muon-neutrino-induced events relative to the number of electron-neutrino-induced events detected. Super-Kamiokande is a large-scale underground water-Cherenkov detector located in Gifu prefecture, Japan, which began taking data in April 1996. The results of an analysis of contained atmospheric-neutrino-induced events from 301.4 live days of detector operation are presented, representing 18.5 kton-years of exposure. The ratio of the number of single-ring muon-like events to the number of single-ring electron-like events is found to be lower than the same ratio predicted by monte carlo:  $R \equiv \frac{(\mu\text{-like}/e\text{-like})_{Data}}{(\mu\text{-like}/e\text{-like})_{MC}} = 0.64 \pm 0.04(stat) \pm 0.06(syst)$  in the kinematic ranges used by IMB ( $0.1 \text{ GeV}/c < p_e < 1.5 \text{ GeV}/c$  and  $0.3 \text{ GeV}/c < p_\mu < 1.5 \text{ GeV}/c$ ), while in the ranges used by Kamiokande ( $0.1 \text{ GeV}/c < p_e$ ,  $0.2 \text{ GeV}/c < p_\mu$  and visible energy  $< 1.33 \text{ GeV}$ ),  $R = 0.65 \pm 0.04(stat) \pm 0.06(syst)$ . The results are discussed in the framework of the two-neutrino oscillation scenarios  $\nu_\mu - \nu_\tau$ ,  $\nu_\mu - \nu_{sterile}$ , and  $\nu_\mu - \nu_e$ .

# Contents

<b>Acknowledgments</b> . . . . .	<b>iii</b>
<b>Abstract</b> . . . . .	<b>vi</b>
<b>List of Tables</b> . . . . .	<b>x</b>
<b>List of Figures</b> . . . . .	<b>xi</b>
<b>1 Introduction</b> . . . . .	<b>1</b>
1.1 History . . . . .	1
1.2 Atmospheric Neutrinos . . . . .	3
1.2.1 $\nu_\mu$ and $\nu_e$ Separation . . . . .	5
1.2.2 Experimental Results . . . . .	5
1.2.3 Observations ( $E_\nu \sim 100 \text{ GeV}$ ) . . . . .	9
1.2.4 Interpretation of Results . . . . .	11
1.2.5 Atmospheric Neutrinos in Super-Kamiokande . . . . .	14
1.2.6 Conclusions . . . . .	14
<b>2 Detector</b> . . . . .	<b>16</b>
2.1 Super-Kamiokande detector . . . . .	16
2.2 Data Flow . . . . .	21
2.3 Detector Electronics . . . . .	22
2.3.1 Inner Detector . . . . .	22
2.4 Specifications and Principles of Operations . . . . .	23
2.4.1 ATM . . . . .	23
2.4.2 GONG . . . . .	25

2.4.3	TRG . . . . .	26
2.4.4	LIME . . . . .	27
2.5	Hitsum . . . . .	29
2.5.1	Outer Detector . . . . .	29
<b>3</b>	<b>Calibration . . . . .</b>	<b>32</b>
3.1	PMT Calibration . . . . .	32
3.2	Time Calibration . . . . .	32
3.3	Charge Calibration . . . . .	33
3.4	Laser Calibration Hardware . . . . .	34
3.4.1	Laser and Optics . . . . .	34
3.4.2	Optical Fibers . . . . .	36
3.4.3	Inner Detector Fibers . . . . .	36
3.4.4	Outer Detector Fibers . . . . .	37
3.4.5	Laser Calibration Operation . . . . .	43
<b>4</b>	<b>Analysis . . . . .</b>	<b>44</b>
4.1	Reduction . . . . .	45
4.2	Event Classification . . . . .	49
4.2.1	Single-ring Finding . . . . .	49
4.2.2	Muon Decay . . . . .	52
4.2.3	Particle ID . . . . .	58
4.2.4	Energy Determination . . . . .	59
4.3	Results . . . . .	62
4.3.1	Comparison of Analyses . . . . .	78
4.4	Interpretation . . . . .	78
4.5	Conclusions . . . . .	90

<b>A Monte Carlo Cross-sections . . . . .</b>	<b>91</b>
<b>B The Super-Kamiokande Collaboration . . . . .</b>	<b>94</b>
<b>C Author . . . . .</b>	<b>96</b>
<b>Bibliography . . . . .</b>	<b>99</b>

# List of Tables

1.1	Summary of contained events from IMB-3 and Kamiokande. . . . .	8
4.1	Fitter errors on MC muons. . . . .	47
4.2	Fitter errors on MC electrons. . . . .	48
4.3	Best-fit results for oscillation scenarios. . . . .	81

# List of Figures

2.1	Geometry of Cherenkov light from passage of relativistic charged particle through the detector medium (water). . . . .	17
2.2	Structure of detector, showing inner-detector cylinder surrounded by outer-detector shell. . . . .	18
2.3	Super-Kamiokande tank in vertical section, showing the PMTs of the inner and outer detectors separated by a 55-cm “dead space.” (Figure not to scale.) . . . . .	19
2.4	Front (inner-detector) and Back (outer-detector) views of a typical wall supermodule. . . . .	20
2.5	Left: Data path between huts on tank top. Right: DAQ cards in TKO crate. . . . .	21
2.6	Inner Detector data acquisition hardware block diagram. Shown is the data path within each of the 4 outer huts. Each online slave computer (two per outer hut) reads out the hit information for one eighth of the detector, passing the hit information to the event-builder software in the central online host computer. . . . .	22
2.7	Outer Detector data acquisition hardware block diagram. Shown is the data path within each of the 4 outer huts. The dual-port memories (DMPs) are read out in the Central Hut by the SUKANT online slave computer. . . . .	31
3.1	Laser Calibration DAQ . . . . .	38
3.2	Laser Calibration Optics . . . . .	39
3.3	Laser Fiber Runs . . . . .	40
3.4	Laser Calibration OD Fiber Mounts . . . . .	41
3.5	Laser fiber diffusers . . . . .	42
4.1	Yastef vertex and direction errors on $\sim 1$ GeV MC muons and electrons. . . . .	47
4.2	Distribution of fully-contained events within the fiducial volume. . . . .	49
4.3	Example of an event classified as multi-ring. . . . .	50

4.4	Ringer values for data and monte carlo samples. Single-ring events have a lower ringer value, and multi-ring events have a higher value.	51
4.5	Example of an event identified as muon-like. . . . .	54
4.6	Example of an event classified as a decay-electron, following previous muon event. . . . .	55
4.7	Example of an entering muon which has stopped in the tank. Note the presence of activity near the entry point in the outer detector, in the upper-right hand corner, which is absent from fully-contained events. . . . .	57
4.8	Example of an event identified as electron-like. . . . .	58
4.9	ADPID lepton misidentification rates for quasi-elastic MC events which pass the reduction cuts. . . . .	60
4.10	DOCHIRA lepton misidentification rates for quasi-elastic MC events which pass the reduction cuts. . . . .	61
4.11	Visible energy of all events and those with mu decay. . . . .	63
4.12	Visible energy of single-ring events and those with mu decay. . . . .	63
4.13	Momentum of single-ring $e$ -like events and those with a mu decay. . . . .	64
4.14	Momentum of single-ring $\mu$ -like events and those with a mu decay. . . . .	64
4.15	Adpid particle-ID distributions for data and MC, IMB cuts. . . . .	66
4.16	Adpid particle-ID distributions for data and MC, KAM cuts. . . . .	66
4.17	Dochira particle-ID distributions for data and MC, IMB cuts. . . . .	67
4.18	Dochira particle-ID distributions for data and MC, KAM cuts. . . . .	67
4.19	Distance along primary (yastef) track of decay (hayai) vertices for events identified as muons with $500\text{MeV} < E_{vis} < 5\text{GeV}$ . . . . .	69
4.20	Adpid PID distributions for data and MC, $1.5\text{ GeV} < E_{vis} < 5\text{ GeV}$ . . . . .	72
4.21	Dochira PID distributions for data and MC, $1.5\text{ GeV} < E_{vis} < 5\text{ GeV}$ . . . . .	72
4.22	Fiducial volume distribution of all events and those with a mu decay. . . . .	74
4.23	Fiducial volume distribution of single-ring events and those with a mu decay. . . . .	74
4.24	$\mu$ -like fraction vs zenith angle, 2-meter fiducial cut. . . . .	75

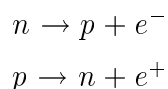
4.25 Muon-decay fraction vs zenith angle 2-meter fiducial cut. . . . .	75
4.26 $\mu$ -like fraction vs zenith angle 5-meter fiducial cut. . . . .	76
4.27 Muon-decay fraction vs zenith angle 5-meter fiducial cut. . . . .	76
4.28 $\mu$ -like fraction vs momentum. . . . .	77
4.29 Muon-decay fraction vs momentum. . . . .	77
4.30 Asymmetry vs visible energy, data. . . . .	82
4.31 Asymmetry trajectory data. . . . .	82
4.32 Asymmetry vs visible energy, MC with no oscillations. . . . .	83
4.33 Asymmetry trajectory MC with no oscillations. . . . .	83
4.34 Asymmetry vs visible energy, MC with $\nu_\mu \rightarrow \nu_\tau$ osc. . . . .	84
4.35 Asymmetry trajectory MC with $\nu_\mu \rightarrow \nu_\tau$ osc. . . . .	84
4.36 Chi-squared, MC with $\nu_\mu \rightarrow \nu_\tau$ osc. . . . .	85
4.37 Asymmetry vs visible energy, MC with $\nu_\mu \rightarrow \nu_{Sterile}$ osc. . . . .	86
4.38 Asymmetry trajectory MC with $\nu_\mu \rightarrow \nu_{Sterile}$ osc. . . . .	86
4.39 Chi-squared, MC with $\nu_\mu \rightarrow \nu_{Sterile}$ osc. . . . .	87
4.40 Asymmetry vs visible energy, MC with $\nu_\mu \rightarrow \nu_e$ osc. . . . .	88
4.41 Asymmetry trajectory MC with $\nu_\mu \rightarrow \nu_e$ osc. . . . .	88
4.42 Chi-squared, MC with $\nu_\mu \rightarrow \nu_e$ osc. . . . .	89
A.1 IMBEEast cross-sections. . . . .	93

# Chapter 1

## Introduction

### 1.1 History

The existence of a light, chargeless particle with spin  $\frac{1}{2}\hbar$  was proposed in the early 1930s as a solution to the apparent lack of energy and angular momentum conservation seen in beta decays. Beta decay is characterized by the emission of an electron from a nucleus; using the particles known to exist in 1932, the proton, neutron and the electron, the best model for beta decay available was:



i.e., the conversion of a neutron in the nucleus to a proton accompanied by the emission of an electron, or conversely the conversion of a proton to a neutron with the emission of a positron. While this conserves charge, measurements of the energy spectrum of the emitted electron or positron (also denoted  $\beta$ ) showed that not all of the momentum and energy released could be accounted for. In addition, since electrons and protons have spin  $\frac{1}{2}$ , it is not possible to combine them to create the spin of the neutron, which is also  $\frac{1}{2}$ . But no other particles were observed in these reactions.

Pauli proposed that a new, fourth particle must be carrying away some energy and angular momentum, unobserved.[1] Since the particle had not been detectable at that point, it would have a very small cross-section. The observed electron energy distribution, smoothly tapering off towards zero, suggested that it must be very light or massless so that it could sometimes take away almost all of the released energy while still conserving momentum. Conservation of angular momentum suggested

that it have spin  $\frac{1}{2}$ . Conservation of charge implied that it was electrically neutral. This particle was dubbed the *neutrino* by Fermi[2], who incorporated it into a new theory of beta decay which introduced the weak nuclear force.

The revised beta-decay formula becomes:

$$\begin{aligned} n &\rightarrow p + e^- + \bar{\nu}_e \\ p &\rightarrow n + e^+ + \nu_e \end{aligned}$$

where the neutrino subscripts indicate that they are electron neutrinos and anti-neutrinos, though the presence of multiple neutrino flavors ( $\nu_e, \nu_\mu, \nu_\tau$ ) wasn't known at the time.

The neutrino itself was not directly observed until 1956 [3] by Reines and Cowan, after preliminary experimental hints in 1953[4,5]. Using the Hanford nuclear reactor as a high-flux source, the neutrino byproducts from the fission reactions were detected by the use of a water and cadmium-chloride medium surrounded by liquid scintillator. Incoming anti-electron neutrinos interact with protons in the liquid, producing a positron and neutron:

$$\bar{\nu}_e + p \rightarrow n + e^+$$

The positron quickly annihilates with an electron to produce two 0.511 MeV gamma rays, which were detected with photomultiplier tubes by observing the light from electromagnetic showers they produce in the surrounding liquid scintillator. This is followed a few microseconds later by the capture of the neutron on a cadmium nucleus, leading to an excited nuclear state which subsequently releases a few MeV worth of gamma radiation, which was again detected. This characteristic signature of two time-separated signals was measured and compared with the detector on and off, permitting a conclusive detection.

Soon after this experiment, the existence of another type, or flavor, of neutrino was discovered at Brookhaven[6], the muon neutrino, which is produced in pion decay:

$$\pi^+ \rightarrow \mu^+ + \nu_\mu$$

$$\pi^- \rightarrow \mu^- + \bar{\nu}_\mu$$

The muon neutrino and the electron neutrino are so labelled because they carry lepton flavor, a conserved quantity in interactions, with the number of [electrons + electron neutrinos] balancing on each side of an equation, as does the number of [muons + muon neutrinos]. The discovery of the tau lepton in 1975[7] implied the further existence of a tau neutrino.

## 1.2 Atmospheric Neutrinos

Atmospheric neutrinos are generated in cosmic ray interactions in the atmosphere: a cosmic ray (predominantly hydrogen and helium nuclei, plus small amounts of heavier nuclei), interacts with a nucleus in the upper atmosphere and produces a cascade of secondaries; the secondaries (typically pions and kaons) either interact again or decay. The decay of pions generates muon neutrinos and muons, which can then further decay into electrons, electron neutrinos and muon neutrinos.

For energies below a few  $GeV$  where most muons decay in flight in the atmosphere, some estimates of the relative fluxes of muon and electron neutrinos can be made from this simple picture.[8] The first is that the neutrino energy spectrum follows the power-law primary spectrum. In such a cascade, the number of positively charged secondaries is nearly equal to the number of negatively charged secondaries. Thus, if we assume that all low-energy pions decay,

$$\begin{aligned}\pi^+ &\rightarrow \mu^+ + \nu_\mu \\ \pi^- &\rightarrow \mu^- + \bar{\nu}_\mu\end{aligned}$$

and that their muon secondaries also decay,

$$\begin{aligned}\mu^+ &\rightarrow e^+ + \nu_e + \bar{\nu}_\mu \\ \mu^- &\rightarrow e^- + \bar{\nu}_e + \nu_\mu\end{aligned}$$

then because of the asymmetry of the  $\pi \rightarrow \mu\nu$ , which gives each of the two neutrinos from muon decay about the same energy as the neutrino from the pion decay, then in a given energy range:

$$\frac{\nu_\mu}{\nu_e} \approx \frac{2}{1},$$

$$\frac{\bar{\nu}_\mu}{\nu_\mu} \approx \frac{2}{1},$$

and due to the excess of protons to neutrons in the incident cosmic rays,

$$\frac{\bar{\nu}_e}{\nu_e} \approx \frac{\mu^-}{\mu^+} < 1.$$

More detailed calculations have been made, accounting for nuclear abundances in the atmosphere, muon energy loss and polarization, and the location of neutrino measurement on the earth.[9,10, 11,12,13] For neutrinos below about 20 GeV, corrections to this picture need to be made to account for the effect of the earth's magnetic field on charged particle trajectories, and on the effects of the solar wind on the flux of incoming cosmic rays.[13] At energies greater than a few GeV, muons don't have much chance to decay before hitting the ground, which sharply reduces the neutrino fluxes further, especially the electron neutrino flux.

Atmospheric neutrino calculations have various uncertainties. Some of these, such as the composition and flux of the primary cosmic rays, are common to all of the calculations. Other uncertainties, for example, the physics assumptions in the interaction model, are not common to the different calculations. A comparison of different atmospheric neutrino flux models finds that the differences in overall neutrino flux are large, up to 30%, due primarily to different models for pion production (20%) and somewhat less due to different treatments of the geomagnetic effects (10%). However, the predicted relative rate of electron- and muon-neutrino interactions varies by only 5%.[14]

### 1.2.1 $\nu_\mu$ and $\nu_e$ Separation

The flavor of the parent neutrino is determined by identifying the lepton type produced in the interaction. Two methods have been used to discriminate between an electron- and muon-neutrino induced events: the first is to observe the muon's decay and the second is to examine in detail the nature of the particle tracks.

The first, and conceptually the simplest method, is to record muon decays that occur after the event in question. (Not all detectors have the ability to recognize the low energy electrons from stopped muon decay.) If the muon decays can be recorded, this method can help distinguish between events with and without a muon. However, this method suffers from some deficiencies. Negative muons can be captured and therefore be lost. In addition, a pion in an event can decay, producing a muon whose delayed decay is then observed. Thus, neutral current events, due to either electron- or muon-neutrinos that produce pions, can appear to be muon-neutrino induced, making calculation of the expected fraction of muon decays complicated.

The second method is more efficient but also more complicated. This “pattern recognition” approach utilizes the difference between an electron's showering track and a muon's minimum ionizing track as these particles pass through the detector. This method can also be fooled by pion production unless the detector has the ability to identify and discard such events.

These two methods are largely independent measures.

### 1.2.2 Experimental Results

Atmospheric neutrinos were first detected in underground detectors as early as the late 1960s[15, 16]. These early experiments used horizontally separated sets of instrumented scintillator elements located in mine shafts to record the path of muons passing through the entire detector. Muon tracks reconstructed as being within 40 deg of straight downward-going were assumed to be cosmic-ray muons that had penetrated from above; muon tracks closer than that to the horizontal, or

upward-going, were assumed to be the products of charged-current interactions of atmospheric neutrinos in the earth surrounding the detector. Of course, some of the straight downward-going events would also be due to neutrino interactions in the rock, but they are indistinguishable from the background of penetrating cosmic-ray muons. Upward-going muon event rates, which depend primarily on a detector's muon energy threshold, are typically  $0.3 - 0.4 m^{-2} yr^{-1}$ .

In the 1980s, underground water-Cherenkov detectors were constructed for the purpose of searching for possible proton decay. These consisted of large tanks of water, lined with photo-multiplier tubes which recorded the Cherenkov radiation produced by high-energy charged particles in the water. They sought to detect the decay products of protons in the water, and were optimized for total event energies up to and over the rest mass of the proton, 938 MeV. An important background to this search was the interaction of atmospheric neutrinos inside the detector.

Atmospheric electron- and muon-neutrinos of average energy  $\sim 1 GeV$ , which interact within the detector volume, produce “contained” events. “Fully-contained” events are those in which all visible products of the interaction stay in the detector, while “partially-contained” events may exit the detector; in general, “contained” is used to mean “fully-contained.” Contained event rates, which depend on the energy threshold and geomagnetic latitude of a detector, as well as solar activity, are typically  $0.5 kt^{-1}d^{-1}$ .

While no evidence of proton decay was found, these detectors were able to study the atmospheric neutrino “background.” Large samples ( $> 100$ ) of contained events have been collected by two general types of detectors. The rates are consistent with the expected interactions of atmospheric neutrinos. Because no conclusive evidence for nucleon decay has yet been observed, these samples have been wholly attributed to atmospheric neutrinos. The possibility that events from other sources have been observed can not be excluded because of the large uncertainty ( $\pm 20\%$ ) in the prediction of the absolute rate of atmospheric neutrino-induced events, as discussed above.

The ring-imaging water-Cherenkov detectors have the largest samples of atmospheric neutrino-induced events. These detectors operate as total absorption calorimeters. Massive particles, such as  $\mu^\pm$  and  $\pi^\pm$ , must be above Cherenkov threshold ( $\sim 180 \text{ MeV}/c$ ) to be detected. Reliable discrimination between massive and showering ( $e^\pm, \gamma$ ) particles is possible with sufficient Cherenkov light collection ( $\gtrsim 1 \text{ pe}/\text{MeV}$ ). Particle direction is unambiguous but vertex resolution is relatively poor ( $\sim 1 \text{ m}$ ).

Small samples of contained events are available from iron tracking calorimeters. These neutrino detectors require volume-intensive instrumentation, limiting their size, but providing excellent spatial resolution ( $\sim 1 \text{ cm}$ ) and reconstruction of particle tracks. Particle types are inferred from their range and ionization yield. A particle's direction is often not determined in these detectors.

**Results from IMB** The IMB-1 detector recorded 401 contained events during an exposure of  $3.77 \text{ kt} - \text{yr}$  extending from September 1982 to June 1984. These data provided an early measurement of the atmospheric neutrino spectrum and composition.[17] The fraction of events having an identified muon decay, which indicates the content of muon neutrino-induced events in the sample, was  $26\% \pm 3\%$ . Simulated data predicted  $34\% \pm 1\%$ . Separation of single- and multiple-ring events and identification of particle types in IMB-1 was not efficient enough to warrant a more sophisticated analysis of flavor composition.

The IMB-3 detector began operation in May 1986 after an upgrade in sensitivity to Cherenkov light. The added light collection allowed more efficient detection of muon decay, a lower trigger threshold, separation of single-ring and multiple-ring events, and particle identification. By March 1991 an additional 935 contained events were collected during a  $7.7 \text{ kt} - \text{yr}$  exposure. These data provided a more precise measurement of the atmospheric neutrino spectrum and particle content.[18] The muon decay fraction of this sample was  $37\% \pm 2\%$ . Simulated data based on an independent model of the atmospheric neutrino flux predicted  $44\% \pm 1\%$ . The muon decay deficiency suggested in IMB-1 data persisted in IMB-3.

A more sensitive test of the neutrino flavor composition in the atmospheric flux differentiated between non-showering and showering particles (in single ring events) using a “pattern recognition” method. These results confirmed an apparent deficit of muon neutrinos interacting in the detector. The number of non-showering, single ring events, as a fraction of the total number of single ring events, in IMB-3 was  $36\% \pm 2\%(\text{syst}) \pm 2\%(\text{stat})$ . The prediction, based on simulated data, was  $51\% \pm 5\%(\text{syst}) \pm 1\%(\text{stat})$ . Again, a shortage of muon-neutrino induced events was apparent.

**Results from Kamiokande** The Kamiokande detector collected 557 events in a 6.18 kt-yr exposure.[19] Although smaller than IMB, its resolution is better and its energy threshold lower due to a greater sensitivity to Cherenkov light. A subset of these data were the first to be analyzed using single ring event separation and particle identification by pattern recognition. Similar deficits of muon decays and  $\nu_\mu$ -induced events are observed in the Kamiokande data; they observed a fractional rate of non-showering events of  $49\% \pm 4\%$  while they expected 61%. Table 1.1 compares the IMB-3 and Kamiokande data.[20,21,22,23]

Table 1.1: Summary of contained events from IMB-3 and Kamiokande.

	IMB-3 # Evts.	IMB-3 Frac. of Total	Kam # Evts.	Kam Frac. of Total
Obs. 1 Ring	507	–	310	–
MC 1 Ring	525	–	333	–
Obs. $\mu$ decay	168	0.33	112	0.36
MC $\mu$ decay	223	0.43	162	0.49
Obs/MC $\mu$ decay	–	$0.77 \pm 0.06$	–	$0.73 \pm 0.07$
Obs. e-like	325	0.64	159	0.51
MC e-like	257	0.49	128	0.38
Obs. $\mu$ -like	182	0.36	151	0.49
MC $\mu$ -like	268	0.51	205	0.62
Obs/MC $\mu$ -like	–	$0.71 \pm 0.05$	–	$0.79 \pm 0.06$

**Fréjus, NUSEX, Soudan-2 results** Another type of neutrino detector is the iron-tracking type, characterized by tracking elements (typically streamer or drift tubes) sandwiched between sheets of iron or steel. Three detectors of this type have reported measurements of contained atmospheric neutrino events: Fréjus, NUSEX and Soudan-2.

The Fréjus detector, located in the Fréjus highway tunnel between France and Italy, collected 188 events.[24] All events with visible energy greater than 200  $MeV$  and an identified lepton are used to measure the ratio of charged current events due to electron- and muon-neutrinos. Neutral current events are identified in this analysis. These data do not show a significant deficit of  $\nu_\mu$ -induced events. They measured a fraction of muon-neutrino induced events, compared with the expected, of  $1.0 \pm 0.15 \pm 0.08$ . [25] This analysis includes upward-going stopping and horizontal muon events, but agrees with an earlier one based only on contained events.

The NUSEX detector, located under Mt. Blanc near the border of France, Italy and Switzerland, consisted of 134 horizontal iron plates with plastic streamer tubes, with a threshold energy of 200 MeV. They reported a ratio of muon-like events to electron events of  $0.96_{-0.28}^{0.32}$  relative to expectation.[26]

The Soudan 2 detector had published 42 single prong events.[27] The visible energy threshold is lower than in Fréjus and an anomalous (lower-than-expected) muon-neutrino induced fraction is observed, though with limited statistics. New results[28] indicate a result that is between that of Fréjus and those of IMB and Kamioka, with the ratio-of-ratios being  $0.75 \pm 0.19$ , thus accommodating either extreme.

### 1.2.3 Observations ( $E_\nu \sim 100 GeV$ )

External events can be used to monitor the flux of atmospheric  $\nu_\mu$  at energies typically 100 times higher than that of contained events. The direction of an upward-going muon is well correlated with that of its  $\nu_\mu$  parent. The distribution of zenith

angles, which peaks at the horizon due to the increased decay length in the atmosphere, is sensitive to possible distortions due to neutrino oscillations. The detectors provide limited information on the energy spectrum of external events, thus limiting the deduced information on the neutrino spectral shape. Large samples of external events have been collected by four experiments. Two are the large ring-imaging water Čerenkov detectors mentioned above. Others are the Baksan scintillation counter telescope and the MACRO detector.

**High energy results from IMB** The IMB detector recorded 617 upward-going muon events during an exposure of 1444 m<sup>2</sup> yr. This corresponds to a flux of  $2.54 \pm 0.10(\text{stat}) \times 10^{-13} \text{cm}^{-2} \text{s}^{-1} \text{sr}^{-1}$  above a muon energy threshold of  $\sim 1.2 \text{ GeV}$ . The predicted value, is based on a hybrid of the Volkova and Lee and Koh flux models, is  $2.46 \pm 0.49(\text{syst}) \times 10^{-13} \text{cm}^{-2} \text{s}^{-1} \text{sr}^{-1}$ .

Information about the neutrino energy spectrum is provided by measuring the fraction of upward-going muons that stop inside the detector. The measured stopping fraction is  $0.138 \pm 0.014(\text{stat})$ , while simulations predict  $0.140 \pm 0.005(\text{stat})$ .

**Kamiokande results on upward muons** The Kamiokande collaboration reports results based on 252 upward-going muon events, which were recorded during an exposure of 842 m<sup>2</sup> yr.[29] This corresponds to a flux of  $2.04 \pm 0.13(\text{stat}) \times 10^{-13} \text{cm}^{-2} \text{s}^{-1} \text{sr}^{-1}$  above a muon energy threshold of 3.0 GeV. Predicted fluxes are  $1.92 - 2.20 \times 10^{-13} \text{cm}^{-2} \text{s}^{-1} \text{sr}^{-1}$  depending of the flux model employed. Stopping muons have yet to be incorporated in the Kamiokande analysis. The zenith angle distribution of upward-going muons recorded at Kamioka is compatible with the predictions from three flux models. Insufficient statistics prevents selection of one model over another.

**Upward-Going Muons Observed in Baksan** The scintillation telescope at Baksan records upward-going muons above an energy threshold of 1 GeV. In 7.18 live years, the  $(17 \times 17 \times 13) \text{m}^3$  detector collected 421 events. This corresponds to

a flux of  $2.77 \pm 0.13(\text{stat}) \pm 0.09(\text{syst}) \times 10^{-13} \text{cm}^{-2} \text{s}^{-1} \text{sr}^{-1}$ . [30] The predicted flux is  $2.45 - 2.75 \times 10^{-13} \text{cm}^{-2} \text{s}^{-1} \text{sr}^{-1}$  depending on the atmospheric neutrino flux model.

**MACRO results on upward muons** MACRO recorded 255 upcoming muon events in 15 months of livetime, being found at the rate of 130 per year. The effective area averaged over the hemisphere is about  $400 \text{ m}^2$ , almost the same as for IMB. A significant data sample was presented in a preliminary report at the DPF meeting in August 1996 in Minneapolis, [31] showing an angular distribution that is a bit low in the two bins nearest the nadir. The results seem to be in minor disagreement with the older and larger samples from Baksan, IMB and Kamioka.

## 1.2.4 Interpretation of Results

As shown in the last section, the results from several independent *measurements* of the atmospheric neutrino flux, spectrum, and composition are in good agreement. However, low energy measurements disagree with the theoretical expectation for the relative rate of muon-neutrino induced events. The expectations are based on detailed predictions of the neutrino flux, neutrino interactions, and the response of the detector(s) in question.

On the other hand, the absolute rate of high-energy (upward-going) muon-neutrino induced events agrees with expectations, albeit with fairly large (primarily systematic) uncertainties. With less uncertainty, the rate of upward-going stopping muons is about as predicted, suggesting that the shape of the high-energy muon-neutrino spectrum is understood.

The apparent dearth of low-energy muon-neutrinos may have several different explanations. As a reminder, the predicted absolute rate of events of either neutrino type is quite uncertain; thus, it has not been possible to determine if the muon-like events are missing or if there are too many electron-like events.

**Theoretical uncertainties** Many different ingredients go into the calculation of the atmospheric neutrino rate in underground detectors: the energy spectrum and composition of the neutrino flux must be known, detailed account must be made for the interaction of the neutrinos (including the absolute cross section, kinematics, and modifications to the interaction made by nuclei), and careful consideration of the response of the detector to the interaction products. Each of these components comes with its own uncertainty. This section briefly describes the remaining uncertainties.

As previously mentioned, the absolute flux of neutrinos is known only to about 20%. However, the relative flux of electron- and muon-neutrinos is known much better. The predicted fraction of muon-like events based on three different flux models does not differ by more than about 2% and we use this to estimate the uncertainty in the relative rate of muon-like events, due to the flux uncertainty.

The absolute value of the neutrino cross section in this energy range is somewhat uncertain. The axial-vector form factor is known to about 10% and additional uncertainty must be added to account for nuclear effects. However, the uncertainty in the relative electron- and muon-neutrino cross section is substantially less.

Finally a systematic error must be added to account for the uncertainty in the particle identification efficiency. Fortunately, with detailed systematic checks performed using cosmic-ray muons and muon-decay electrons, the uncertainty in the efficiency is only about 2%.

Therefore the estimated total systematic uncertainty in the fraction of muon-like events is about 5%. However, experimental tests are required to verify these results.

**Possible new physics: neutrino oscillations** One possible explanation of the apparent dearth of muon-type events is neutrino flavor oscillations. Oscillations between neighboring neutrino families is theoretically preferred. Muon-neutrino to tau-neutrino oscillations will most effectively rid the observed atmospheric neutrino events of a muon-like component; however,  $\nu_e$ - $\nu_\mu$  oscillations are also possible.

More convincing evidence for neutrino oscillations would be found in either the observed neutrino energy spectrum (low energy neutrinos oscillate earlier) or in their zenith angle distribution (downward-going neutrinos may not have had a chance to oscillate due to their short path length). muon-like events depends on either zenith angle or energy.

Upward-going external muon-neutrino induced events (entering events with vertices in the rock below) should show evidence for oscillations. Although at higher energies, these neutrinos have all traveled great distances. Yet, the rate, and zenith-angle and energy distribution of these events have been reported to be as expected from predictions,[32,33]. Further research in this area is being carried out.

**Possible new physics: proton decay** It has been suggested[34] that the atmospheric neutrino problem is not due to a deficit of muon-like events but to an excess of low-energy electron-like events from proton decay. The analysis was based on a selected neutrino flux calculation. Corrections were necessary to compare this calculation to the observed Kamiokande data. Although these corrections are not exact, the authors conclude that there are too many low-energy electron-like events (above the expected “background” from their corrected model) and these events are compatible with  $p \rightarrow e^+ \nu \nu$  with a lifetime of about  $4 \times 10^{31}$  years.

The most obvious criticism is that, using any of the more recent neutrino flux calculations coupled to sophisticated detector simulations, analysis shows no such low-energy excess. If protons do decay by the mode  $p \rightarrow e^+ \nu \nu$ , several companion modes (such as  $n \rightarrow e^+ e^- \nu$ ) should have similar lifetimes; on the other hand, current experimental lower limits for the lifetime for the companion modes are much longer than the lifetime inferred above. Another criticism is that the anomaly seems to extend to too high an energy in Kamioka and IMB.

### 1.2.5 Atmospheric Neutrinos in Super-Kamiokande

Super-Kamiokande is a 50 kton water-Cherenkov detector. The sheer size of Super-Kamiokande is very important for refined measurements of the atmospheric neutrino flux and composition. The IMB detector recorded about 1 contained atmospheric neutrino event per day of operation whereas Super-Kamiokande records about 7. Systematic uncertainties will eventually dominate the statistical uncertainty in Super-Kamiokande but the improved statistics allow the data to be cut into different classes for systematic studies.

However, it is not only size that separates Super-Kamiokande from the earlier generation of underground detectors. The pattern recognition method of particle identification previously suffered from modest light collection (about  $1 - 5 \text{ pe/MeV}$ ) and vertex resolution (about  $1 \text{ m}$ ); for example, a misfit event vertex could turn a muon track into an apparent electron track and vice versa. Thus, the efficiency for correct particle identification in IMB-3 was slightly better than 90% and in Kamiokande it is about 98%.

### 1.2.6 Conclusions

The underground measurements of the atmospheric neutrino spectrum and composition are in good agreement. The disagreement between these measurements and the theoretical predictions is, however, statistically quite significant. The cause of the disagreement must thus be either an unidentified systematic effect in the flux calculation, neutrino model, or detector simulation, or some new physics.

Investigation of systematic effects (the neutrino model or detector simulation) requires controlled experiments. Such experiments include a charged particle beam test, now concluded, and a future neutrino beam test. Both of these tests employ a large water-Cherenkov detector at KEK. The beam test (E-261) indicated no problem with the particle identification methods employed in IMB and Kamioka. [35,36] Isolation of potential systematic problems with the neutrino flux calculations

will require, among other things, much more atmospheric neutrino data to search for energy, zenith angle, or other effects, that might indicate the nature of the problem.

The unambiguous confirmation that the atmospheric neutrino problem is actually the result of some exciting new physics will require a vast increase in the size of the neutrino event sample. The most compelling explanation involving new physics is that neutrino oscillations are causing the  $\nu_\mu$ 's to disappear before they reach the underground detectors.

Several complementary approaches are likely to be required to probe this possibility completely. One approach uses the greater statistics in the neutrino sample, along with greatly improved resolutions and particle identification efficiencies of Super-Kamiokande to allow a detailed systematic search for possible energy or path-length deviations that would indicate neutrino oscillations.

Another approach that will be used to attack this problem are accelerator based long-baseline neutrino oscillation experiments. Because of the range of neutrino masses implied by the atmospheric anomaly, such an experiment will require that the neutrino beam energy and path length satisfy  $\frac{L}{E} \geq 100 \text{ km/GeV}$ . Such possibilities have been investigated in proposals at FNAL, BNL and CERN for long-baseline neutrino experiments. An  $\sim 1 \text{ GeV}$  neutrino beam from KEK (E-362) pointed at Super-Kamiokande will fulfill this requirement with the added advantage of using an existing, well understood, very large detector with excellent resolution.

Hints of an atmospheric neutrino problem were first uncovered in data from the IMB and Kamiokande detectors. The goal of the first year of data-taking at Super-Kamiokande has been to confirm the results, and acquire better statistics.

# Chapter 2

## Detector

### 2.1 Super-Kamiokande detector

Super-Kamiokande is a 50 kton water Cherenkov detector located in the Mozumi mine of the Kamioka Mining Company in Gifu prefecture, Japan. It lies one kilometer below the peak of Mt. Ikeno, and is reached by a two-km long access tunnel. The mine, a source of zinc, copper and silver ores until 1995, is now inactive and operates chiefly as a research site; in addition to Super-Kamiokande, the mine also houses the predecessor experiment Kamiokande, the site of which is slated for conversion to the KAM-LAND long-baseline reactor experiment. The water-equivalent depth for cosmic rays is 2700 m.

Super-Kamiokande is a ring-imaging water-Cherenkov detector. Charged particles moving through the water at relativistic speeds ( $\beta (= v/c) > c/n$ ) emit a forward cone of light with half angle given by:

$$\cos(\theta) = \frac{1}{n\beta},$$

which for water, with index of refraction  $n = 1.33$ , gives a Cherenkov angle of about 42 deg for  $\beta \sim c$ . The light is emitted in a spectrum which, when folded through the transmission of water, ranges from 300 to 600 nm, and peaks at around 360 nm. This light is detected by photomultiplier tubes, where the measured timing and intensity of the light at each tube is used to reconstruct the particle track. Figure 2.1 shows the geometry of the light relative to the charged particle track and the photomultiplier tubes in the detector.

The detector comprises 11146 Hamamatsu R3600 50-cm diameter photomultiplier tubes (PMTs), lining and viewing a cylindrical volume of ultra-pure water 16.9 m

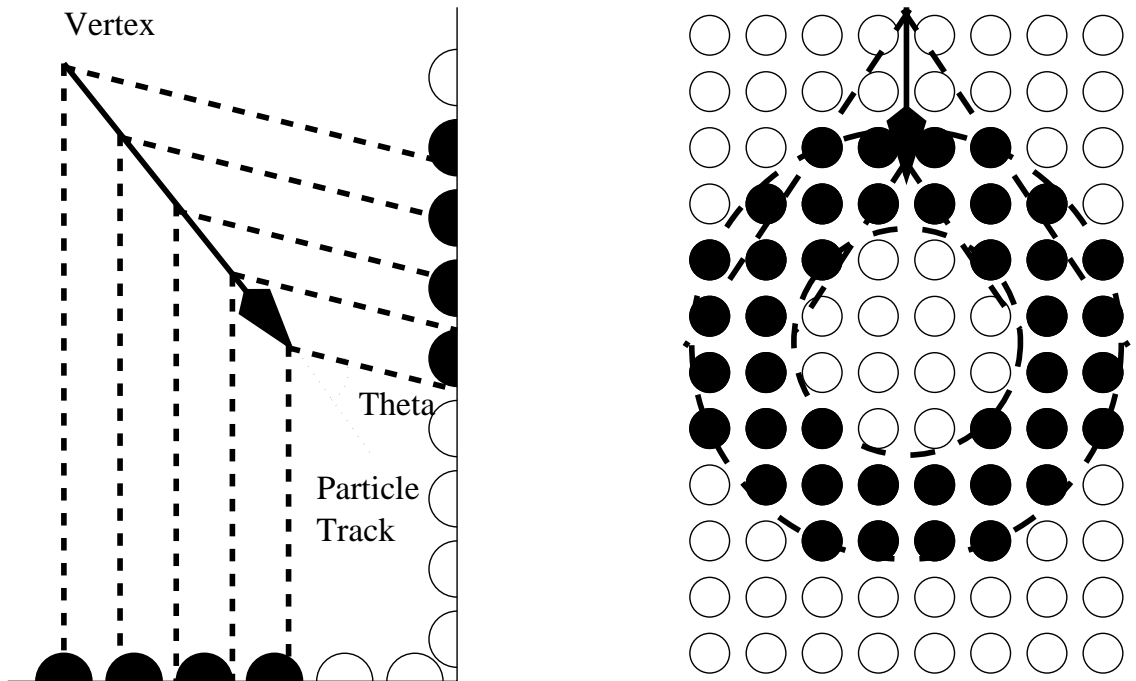


Figure 2.1: Geometry of Cherenkov light from passage of relativistic charged particle through the detector medium (water).

in radius and 36.2 m high. An outer detector and shield of 2.5 m thickness of water completely surrounds the inner detector. The outer detector is instrumented by 1885 Hamamatsu R1408 20-cm PMTs, and is used to reject incoming tracks from cosmic rays and passively shield against radioactivity from the surrounding rock. Figure 2.2 shows the relationship between the two main detector volumes.

The inner detector tubes are similar to those used in Kamiokande, redesigned for an improved timing resolution of 2.5 ns at the 1 p.e. level. [37] The outer detector tubes are the same tubes that were used in IMB, recycled. Attached to the equator of each outer-detector tube face is a “wave-shifter plate” which increases the collection efficiency by 60% over that of a bare tube. Figure 2.3 shows the tube mounting in the detector in vertical cross-section.

The tubes are mounted in units of “super-modules,” consisting of 12 inner-detector tubes on the front side and 2 outer-detector tube/wave-shifter pairs on the back side.

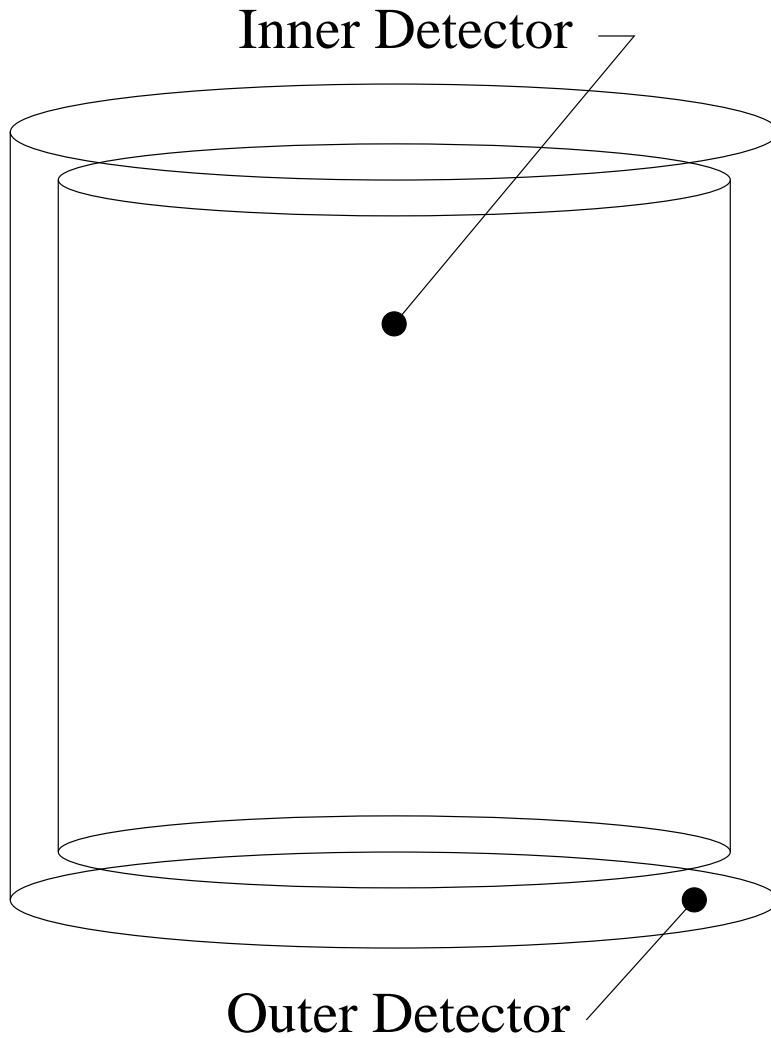


Figure 2.2: Structure of detector, showing inner-detector cylinder surrounded by outer-detector shell.

The inner and outer tubes face away from each other to view their respective detector volumes. The two detector regions are optically separated by a pair of opaque sheets which enclose a dead region 55 cm in thickness. On the inner-detector side a black plastic sheet is used to minimize reflections from an event back into the detector. On the outer-detector side of the super-module, and lining the outer walls of the tank, is white reflective Tyvek sheeting in order to maximize the light-collection efficiency of the outer detector. The Tyvek which is mounted on the frame has a black non-reflective backing, to absorb any light which makes its way into the dead

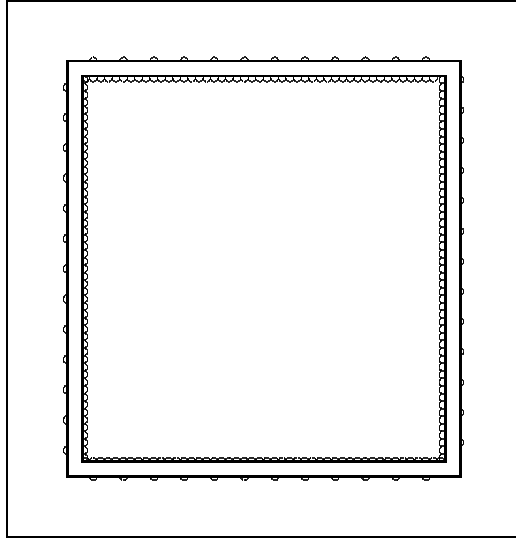


Figure 2.3: Super-Kamiokande tank in vertical section, showing the PMTs of the inner and outer detectors separated by a 55-cm “dead space.” (Figure not to scale.)

space inside the super-module or is generated there by events passing through or originating in the dead space. Figure 2.4 shows the relative positions of the tubes in a supermodule. The wall of the detector is composed of towers of supermodules, 17 high. There are 37.5 towers, Tower 28 being a half-width tower. The super-modules on the top and bottom of the detector have a different framework, but the relative tube positions are much the same.

The inner PMTs are read out with custom Analog Timing Modules (ATMs [38]), which provide 1024 ns range at 0.25 ns resolution in time and 409.5 pC range at 0.1 pC ( 0.2 photoelectron) resolution in charge for each PMT. The outer PMTs are instrumented with custom charge-to-time conversion modules, QTCs (built at BU), which output timing pulses at a fixed delay from the rising edge of the incoming PMT pulse with a time-width proportional to the integrated charge of the PMT pulse. These signals are then digitized with LeCroy 1877 TDCs with 16  $\mu$ s full-ranges. The resulting resolutions are 0.5 ns in timing and 0.1 p.e. in charge. The

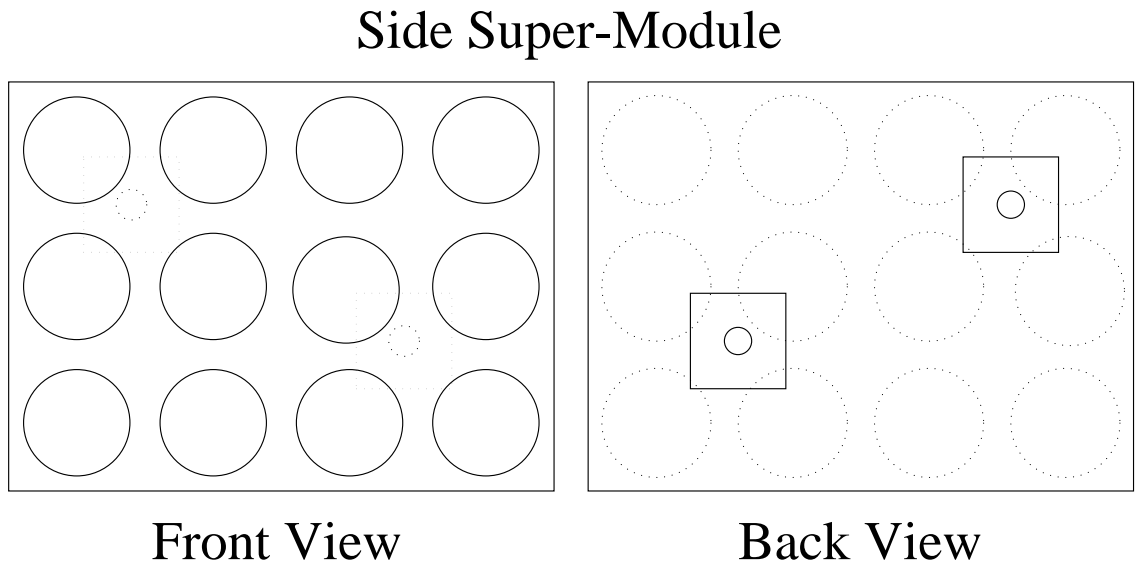


Figure 2.4: Front (inner-detector) and Back (outer-detector) views of a typical wall supermodule.

time and charge calibration of the raw data for both inner and outer detectors is done immediately offline and both analyses start with the same calibrated data.

The trigger is formed by the coincidence of PMT hits, at a threshold of 0.2 p.e. in a coincidence window 200 ns wide. The trigger threshold is set at 5.5 MeV of visible energy, defined as the energy of an electron which would produce the same number of Cherenkov photons as the given event. (Note: after the first year of data-taking, a new “super-low trigger” was installed which permits data-taking down to a threshold of 4.5 MeV, though with lower efficiency than that above 5.5 MeV.) The noise rate in each tube is 3.6 kHz. The average attenuation length for Cerenkov light is 68 m, varying  $\pm 5\%$  over the course of data-taking. The raw data are saved at a total rate of 20 GB (one DLT tape) per day.

## 2.2 Data Flow

Data from the detector is read out via 10 “online slave” computers: 8 (named sukon1 - sukon8) to read out the inner detector tubes, 1 (sukant) to read out the outer detector tubes, and 1 (sukon9) to handle the trigger electronics. Data from the online slaves is passed to the “online host” computer (sukonh), which assembles the data into events and passes the events (in “online format”) to a reformatting computer (sukrfm). This machine converts each event to offline format, and then transmits it via fiber optic link to the computer center outside the mine in the nearby town of Mozumi. There the data are further converted from raw hit counts to calibrated T (ns) and Q (p.e.). The raw data are also archived to tape in Mozumi. Figure 2.5 shows the data-flow on the top of the tank; the online-host and reformatting computers are located in the control room, in a tunnel off the top of the figure.

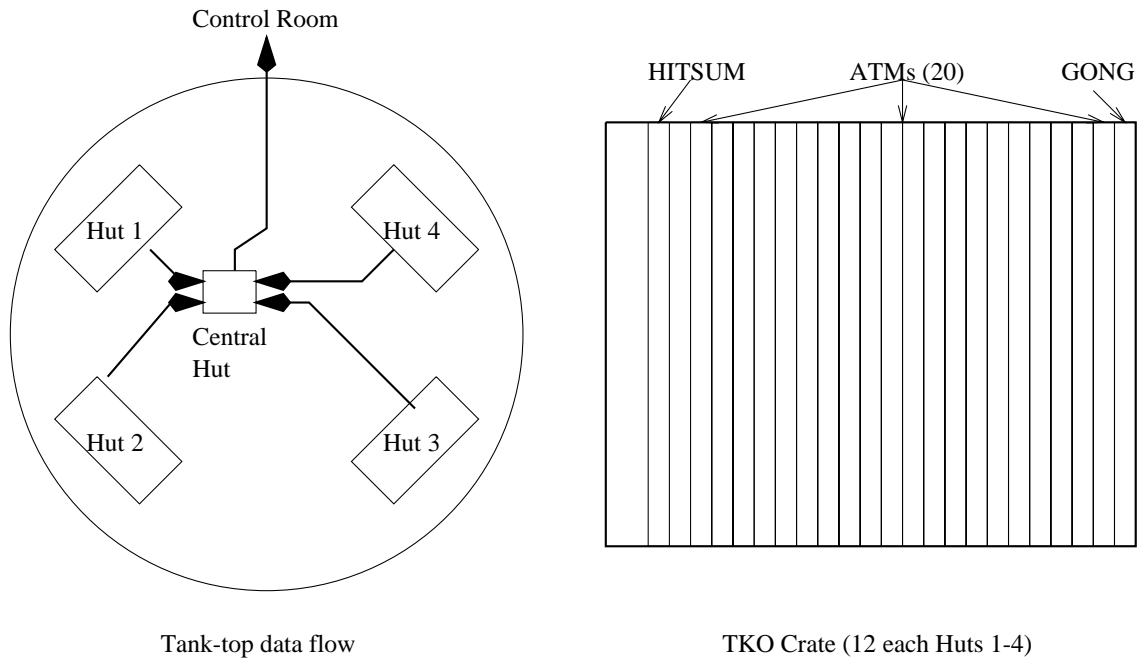


Figure 2.5: Left: Data path between huts on tank top. Right: DAQ cards in TKO crate.

The calibrated data are distributed down two paths: one is a reduction chain operated by the onsite groups (consisting largely of members of Japanese institutions,

but including participation from the University of Washington and SUNY Stony Brook); the other is a tape archiving process operated by the US institutions for shipment back to SUNY Stony Brook in the US, where it undergoes a separate, independent reduction from the onsite one for distribution to other institutions in the US. The offsite copy of the data also forms a backup for the onsite tape archive.

## 2.3 Detector Electronics

The inner and outer detectors, besides using different PMTs, also have different read-out electronics. The hit information is merged inside the mine before being transmitted to the computer center in Mozumi.

### 2.3.1 Inner Detector

Figure 2.6 shows the data path for the inner detector. The specific modules are discussed below.

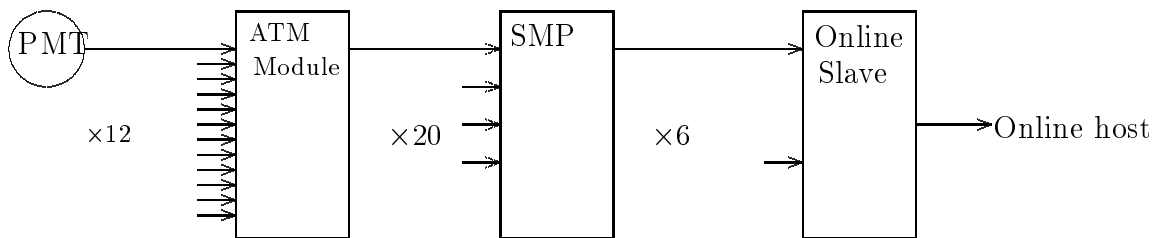


Figure 2.6: Inner Detector data acquisition hardware block diagram. Shown is the data path within each of the 4 outer huts. Each online slave computer (two per outer hut) reads out the hit information for one eighth of the detector, passing the hit information to the event-builder software in the central online host computer.

This section presents a summary of the specifications for the Super-Kamiokande front-end electronics modules (ATM, GONG, TRG, LIME).

## 2.4 Specifications and Principles of Operations

### 2.4.1 ATM

The ATM (Analog Timing Module) digitizes the charge and time information for 12 PMTs.[38] Each tube channel (0-11) is divided into two subchannels (A and B), which alternate digitizing hit information from the PMT. There are 20 ATMs per TKO crate in the Super-Kamiokande inner-detector DAQ.[39]

ATM specifications [38]:

- FIFO capacity: 1024 16-bit words.
- FIFO read-out format:
  - Word 0:** [00][8-bit event #][0/1 (A/B)][0][4-bit chan #]
  - Word 1:** [01][00][12-bit TDC data (0-1023 ns, 0.25 ns/count)]
  - Word 2:** [10][00][12-bit QDC data (0-409.5 pC, 0.1 pC/count)]
  - Word ...:** Repeat for each hit received.
- Programmable modes:
  - OPERATE:** Normal operation mode.
  - PEDESTAL:** Used for TDC calibration. TDC gate width controlled by GONG, instead of self-gating on a tube hit.
  - CAL:** Used for QDC calibration. Takes input from CAL connector on front-panel, instead of from tubes.
  - MEMTEST:** Used to test FIFO memory.
- Other programmable options:
  - Threshold (for all channels) programmable from 0 to -1.25V, in steps of 0.61 mV. (Threshold is applied after amplification; 0.1 p.e. corresponds to minus 50-60 mV.)
  - Programmable 8-bit module ID.

### ATM channel hit sequence

When a hit comes in from a PMT, the HIT one-shot (see Ref. [39], Figure 3-7) issues a 900 ns gate. This goes into the “self-gate” logic, which starts the TAC charging and opens a 400 ns acceptance gate on the QAC for whichever sub-channel (*e.g.* A) is available on that tube channel. When the trigger signal reaches the ATM, the TAC stops charging, and analog-to-digital conversion for that sub-channel can begin (but see below). However, no matter when the trigger comes in, the self-gate part is dead for 900 ns from the start of the HIT signal from the one-shot. Once that 900 ns is ended, the self-gate logic is ready to direct the next hit to the other channel (*e.g.* B). If a trigger does not come in within  $1.1 \mu\text{s}$  of the hit, the channel initiates an auto-clear operation. 200 ns later, the sub-channel (A or B) can take another hit.

If both sub-channels A and B are occupied when a hit comes in, the hit cannot be processed and is lost.

The HIT signal for a tube channel *always* causes the channel to toggle between taking data on sub-channel A or sub-channel B. (The sub-channel selection logic is simply a flip-flop with its input connected to its output through an inverter, clocked by the rising edge of the HIT signal. See Ref. [38]) Hence, if the selected sub-channel for that particular hit is busy, the hit is lost, even if the other sub-channel might be available to take the hit. However, this is a very rare occurrence, and the effect on data-taking is negligible.

### ATM hit conversion sequence

When a trigger comes in, all channels which had hits within  $1.1 \mu\text{s}$  before the trigger get registered in the HITAD register. If the HITAD register is non-empty, conversion of all hit channels begins in the order of channel priority. (The channels, in order of decreasing priority, are: 0A, 1A, ..., 11A, 0B, 1B, ..., 11B.) Conversion begins at the first hit channel in the priority list, and for each channel it consists of:

1. Writing the channel and event number to the FIFO.
2. Converting the TAC value, and writing it to the FIFO.
3. Converting the Q value, and writing it to the FIFO.
4. Resetting the channel, and clearing it from the HITAD register.

Conversion and writing to FIFO take 6  $\mu$ s per channel.

NOTE: Each trigger can lead to new hit channels being marked in the HITAD register. The highest priority channel in the HITAD register always gets converted next, so channels do not necessarily get converted on an event-by-event basis. For example, if channel 4B is being converted for a particular event, and a new trigger comes in with channel 0A being marked hit, then channel 0A will be the next channel to be converted after channel 4B, regardless of what other channels were hit in the previous trigger. This means that hits from a single event will not necessarily be contiguous in the ATM's FIFO.

## Dead time

What is the dead-time for an individual tube? A hit for a particular tube is lost if:

- it comes within 900 ns of the previous hit from that tube (this is intentional, to handle reflections); or
- the previous two hits had associated triggers, and neither channel A nor channel B for that tube has finished converting; or
- the previous hit had no associated trigger, but the hit before that *did* have a trigger and has not yet finished converting (due to the sub-channel selection mechanism described above); or
- it had no associated trigger (of course).

### 2.4.2 GONG

The GONG (GO/No Go) module is a TKO [40] module which handles triggering and gate operation for all DAQ modules (ATMs) in the crate. There is one per

TKO crate. A summary of the features of the GONG module[41] designed for Super-Kamiokande:

- Latches 16-bit event number from the TRG module (as differential ECL via ribbon cable).
  - Distributes lower 8 bits to ATMs (as TTL via ribbon cable).
  - Stores 16-bit event number internally, which gets read out when the ATMs are read out.
  - Only retains the last event number – each new trigger overwrites the previous event number.
- Distributes trigger signal from the front panel (either NIM via lemo, or differential ECL over the event- number ribbon cable – selectable by jumper switch), to the ATMs over the TKO backplane.
- Can generate programmable delay (0-1500 ns, plus 50+ ns offset) for use in calibrating ATM TDCs.

### 2.4.3 TRG

The TRG (TRiGger) module generates event numbers, and distributes trigger signals to the GONGs. It has 8 inputs, each one of which can generate a trigger. The TRG stores information about which of the input triggers (*e.g.*, inner-detector trigger(s), outer-detector trigger(s), calibration triggers) contributed to each event. For each trigger input, a bit gets set in the Trigger ID byte. This Trigger ID byte gets read out and stored with the event information by the DAQ software.

General behavior:

- Trigger fires (sends TRIGGER OUT) about 30 ns after first trigger input.
- Trigger ID is latched on second rising edge of 25 MHz clock after Trigger fires. ( $\sim 50$  ns after first trigger input).

- Further trigger inputs between first one and ID latch get lumped under first event number. Trigger inputs after that, and until Trigger CLEAR completes, are lost.
  - There is about 120 ns minimum time between successive triggers (event numbers).
  - This does not lead to dead-time, just merging of different events under the same event number.
  - Trigger event number is incremented at the end of cycle, to be ready for next time.

Two of the trigger inputs are reserved for dead-time monitoring. When the TRG is in dead-time monitoring mode, fake events are generated at the beginning and end of TRG dead-time (due to VETO assertion, e.g.) with one of the ID bits used to mark the beginning of dead-time, and the other to mark the end of dead-time.

#### 2.4.4 LIME

The LIME (LIMitEr) module monitors the event count, and regulates the readout of the TKO crates by the SMP. Its primary function is to ensure that the ATMs are read out frequently enough that the ATM 8-bit event numbers can be reconstructed properly into their corresponding 16-bit event numbers.

Every  $N_{Accept}$  events (settable via DIP switch), an ACCEPT signal is sent to the SMP. This initiates a read-out of the TKO crates. However:

- After every ACCEPT signal, there is a 120  $\mu s$  inhibitory period before the next one can be sent. This ensures that, for normal data taking, the hits for a single event in one ATM are not spread over more than two data scans.
- No ACCEPT signal is sent while BUSY is asserted by the SMP.

While BUSY is asserted, the TRG is still permitted to continue firing, up until the next modulo- $N_{Veto}$  event count. ( $N_{Veto}$ , like  $N_{Accept}$ , is settable via DIP switch.  $N_{Veto}$  must be larger than  $N_{Accept}$ .) At the  $N_{Veto}$ th event, VETO is sent from the LIME to the TRG to halt data-taking.

The LIME maintains its own internal event counter, and does not see the event-number generated by TRG. This event counter is incremented every time the TRG fires. So the LIME's modulo-N event counter may not wrap around at the same boundaries as real event numbers. However, the LIME has a “Clear” input for resetting the internal counters, which could be used to synchronize with the TRG event counter, if needed.

For high-occupancy events, such as laser calibration events at high light levels, the ATM FIFOs can overflow if  $N_{Accept}$  is set higher than 28. (Each ATM FIFO has a capacity of 1024 words, or 341 hits, so it can hold 28 12-tube events.) To handle such high-occupancy events, the LIME has a “Special Trigger” input which forces an ACCEPT to be generated regardless of the state of the internal counters.

## 2.5 Hitsum

The ATM hitsum signal can best be represented by a trapezoidal pulse, with a rise time, defined by 10% to 90% of the rising edge, measured to be  $9.4 \pm 1.1$  ns. The pulse height was measured to be  $14.4 \pm 1.3$  ns, with a flat-top duration of 151 ns. The full width of the pulse at the base (measured from 10% off baseline at the leading edge to 10% off baseline at the falling edge) is 200 ns.[42]

### 2.5.1 Outer Detector

The outer detector forms a cylindrical shell around the inner detector. Separated from the inner detector by an optically isolated dead zone 55 cm thick. It is 2.5 meters in thickness, passively shielding the inner detector from neutrons and gamma rays from the surrounding rock. In addition, it is instrumented by 1885 20-cm Hamamatsu R-1408 PMTs, which provide active detection of incoming cosmic rays. The PMTs themselves, in fact, are recycled from the old IMB detector.

Figure 2.7 shows the data acquisition path from the OD PMTs to the central hut. Each PMT is connected to a custom “paddle card,” built at LSU, from which is distributed high voltage and to which the analog signal from the PMT is passed. This signal is then passed to a discriminator and charge-to-time converter (QTC) module, built at BU. Each QTC channel self-triggers at a threshold set at 25 mV (about one-half p.e.), and integrates the charge of the PMT signal to produce a differential-ECL pulse, the width of which is proportional to the integrated charge of the PMT pulse. The leading edge of this pulse gives the time of the leading edge of the PMT pulse (plus an offset).

A QTC channel also provide a HITSUM signal, 200 ns wide and 20 mV high per hit. The individual hitsums from each channel in the outer detector are summed in each of the four outer huts, and then globally summed in the central hut and fed as an input to the TRG module. If the OD trigger goes over triggering threshold (about 19 hits), it is held for 100 ns to see if the inner detector also generates a

trigger, because it is preferable for event reconstruction to have the event trigger based on the inner-detector timing when there is inner-detector activity. Only if no inner detector trigger is generated within the hold window is the outer detector trigger released to generate an OD-only trigger. Otherwise, the two triggers are fed together into the TRG, at the time of the inner-detector trigger, to provide tags that both sections of the detector fired.

The ECL pulse from each QTC is fed into an input of a LeCroy 1877 time-to-digital converter (TDC). Five TDCs, with 96 input channels each, are located in each Fastbus crate, one per outer hut. The TDCs record the rising and falling edges of the QTC signals, and are read out by a Fastbus Smart Crate Controller, which communicates with the OD DAQ online slave in (SUKANT) via VME-mounted dual-port memory modules in the central hut.

The TDCs are capable of storing up to 8 hits (16 edges) for each event, over a window of up to 32 microseconds, providing a record covering a range both before and after an inner-detector event of what was happening in the outer detector. The primary aim of this expanded recording window is to catch “stealth muons,” cosmic muons which stop in the outer detector and then decay in the inner detector, generating a Michelle electron which might otherwise be mistaken for a neutrino interaction in the inner detector. The window for outer-detector data-taking was initially set at 16 microseconds before and 16 microseconds after the trigger time of an inner-detector event. In September 1996 (starting with run 2800) this window was shortened to 10 microseconds before and 6 microseconds after the main event; in the event of a high-intensity hit on a tube, reflections on the PMT cable can lead to additional hits being recorded in the TDC, which can overflow the 8-hit buffer in the TDC and lead to loss of the primary hit. While this does not affect the ability to determine that a cosmic muon has entered the detector (it is very clear that one entered from the number of hits in such a case!), the loss of in-time hits complicates the ability to locate the entry cluster in the outer detector.

After the end of the outer-detector recording window, the outer detector becomes busy for 2-5 microseconds (depending on the size of outer-detector data) digitizing

the hit information, and is unable to generate new OD triggers. During this digitization period, an “OD busy” bit is placed in the data stream so that the dead time can be determined.

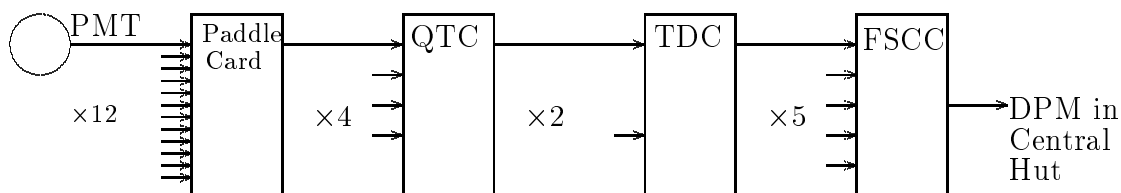


Figure 2.7: Outer Detector data acquisition hardware block diagram. Shown is the data path within each of the 4 outer huts. The dual-port memories (DMPs) are read out in the Central Hut by the SUKANT online slave computer.

# Chapter 3

## Calibration

The calibrations for the data fall into two classes:

1. Hardware calibration: converting raw digitized PMT counts to T (ns) and Q (p.e.).
2. Detector calibration: measuring the response of the detector in terms of number of measured p.e. per MeV deposited from each type of event.

The first set of calibrations are carried out at intervals by members of the calibration group, which supplies the same set of calibration constants to the data used by all members of the collaboration. The second set of calibrations are carried out by members of the different analysis groups, with customized response functions developed for their particular needs, though with cross-checks against different energy regimes as necessary.

This chapter describes the hardware calibration. Detector calibration is covered under Chapter 4.

### 3.1 PMT Calibration

### 3.2 Time Calibration

The time slopes of the PMT readout electronics (ATMs and TDCs) are measured independently of the PMTs. To measure the relative timing between each tube and the trigger a nitrogen dye laser system is used (described in the next section). Light from the laser is distributed to known points in the detector, from which the travel

time is calculated to generate a list of timing offsets based on each tube’s response to calibration pulses. In addition, each tube has a separate slewing correction that must be made for a given pulse-height; in general, the larger a pulse from a given PMT is, the earlier it will go over the triggering threshold in the readout electronics. This effect is measured by varying the intensity of the laser pulse, which allows one to make a “T-Q map” that describes the time offset correction one has to apply to a given tube for a given measured charge from it. T-Q map runs are taken every few months to provide updated slewing corrections for the inner detector. For the outer detector, where precise tube-to-tube slewing corrections are not needed, an average slewing correction that was measured soon after detector turn-on is used.

### 3.3 Charge Calibration

To calibrate raw charge (Q) readings into photoelectrons (p.e.) for each tube in the inner detector, a xenon flash lamp is used as the light source. This source has much pulse stability than the laser, which varies  $\pm 10 - 20\%$  from pulse to pulse and the intensity of which decreases over the long term as the flash cartridge wears out and the dye bleaches.

The laser is used for Q calibration of the outer detector tubes. The method is the same as that used in IMB[43]. Light pulses of varying intensity are used; at the lowest intensities, a tube will only detect less than one photon on average. The occupancy (number of times a tube fires per hundred laser pulses) of a tube at such a low light level is used to calculate the average number of p.e. it receives using Poisson statistics. This allows the single-p.e. response of the tube to be measured, from which the gain at higher light levels (100% occupancy) can be extrapolated. At high enough light levels, typically around 50 p.e. for the outer detector tubes, a tube begins to saturate. The gain for an outer detector tube is composed of a linear component, used for signals up to a measured saturation point, followed by a quadratic fit beyond that point.

The pedestals, or zero-offsets, of the tubes is also measured. The inner detector electronics have automatic pedestal measurements made every 30 minutes, which are read out as special pedestal events in the data stream. Only one-eighth of the inner detector is put into pedestal mode at a time, in order maximize detector up-time for supernova detection. Pedestal mode events are not used as part of normal data analysis. Outer detector pedestal measurements are made only occasionally, usually when there has been some change in the hardware.

## 3.4 Laser Calibration Hardware

### 3.4.1 Laser and Optics

An overview of the laser and optics section is shown in Figure 3.2. The basic scheme is similar to that used in Kamiokande and IMB[43], with the addition of multiple fiber outputs to reach different parts of the detector.

The laser is a Laser Sciences, Inc. LSI V337-ND-S, which has an average pulse energy of 300  $\mu\text{J}$ , and pulse width of 3-4 ns. It is a closed system nitrogen laser, fired by a TTL trigger. It provides a synch output from a photo-detector on the back of the flash tube which indicates the time of laser fire to within about 1 ns, but for greater precision we mounted a fiber optic pickup to the back of the flashtube, which goes to a fast (300 ps rise-time) PMT. This PMT, called ‘‘T.Mon.’’ is used to generate the detector trigger for timing calibrations.

The output of the nitrogen laser, with a wavelength of 337 nm, pumps a tunable dye laser (0.3 nm bandwidth), which generates 384 nm output using Exalite 384 dye. A logarithmically graded filter wheel is connected by fiber to the output of the dye module. and its output is fed into a two-way splitter.

The filter wheel for setting the light level is controlled by a stepper-motor controller in a CAMAC crate. The slope of the filter wheel was measured with a PMT attached

to the output of the wheel, and read out with a Caen C205 dual range charge-integrating ADC (.25 pC on low range, 30 pC on high range). The slope is  $\sim 270$  steps per decade, with about a 1500-step range beginning at step 300 (the brightest setting).

The fiber from the filter wheel is fed into a 1:2 splitter and then to two optical switches. One switch is a 1:9 splitter, the other a 1:50. By convention, the channel used for inner detector calibration is switch 1 channel 9. All 50 switches of the second switch, and 2 of the channels on the first switch, are connected to a set of optical fibers which are permanently mounted in the outer detector. This configuration permits simultaneously firing two fibers at once, which saves time and detector down-time during outer-detector calibration runs. The switches are manufactured by Dicon, and are normally operated via a CAMAC-mounted GPIB controller. They can also be operated manually if desired, and have a separate “channel 0” (no fibers selected) position. The fibers inside the switches contain a germanium dopant, which was found to fluoresce in 337 nm light from the bare nitrogen laser without dye module. (This is due to an absorption line at 330 nm.) This does not cause a problem for ordinary calibrations at 384 nm, but in the event that it is desired to operate the laser at 337 nm, the switches must be disconnected from the system.

The DAQ, shown in Figure 3.1, is CAMAC-based. The stepper-motor controller and interface to the optical switches are not shown. The laser trigger, delayed by a fixed amount, is fed into the calibration input of the TRG module, generating events which are tagged by the corresponding bit in the TRG-ID byte. Since laser triggers can (very occasionally) be lost if they are preceded within about 100 nanoseconds by other triggers – and hence, the TRG-ID bit for the laser calibration might be lost – other triggers are ordinarily disabled. It is possible to run without disabling the other triggers; this triggering scheme permits the detector to continue operating during calibration, though the non-calibration events during a calibration run has to be set aside from normal analysis, to be used only if something interesting happens (e.g. a supernova) during the run.

### 3.4.2 Optical Fibers

Connected to the outputs of the switches are 53 optical fibers of UV/Vis grade fused silica with a 200  $\mu\text{m}$  diameter core. There is a 10  $\mu\text{m}$  fused silica cladding and another 10  $\mu\text{m}$  protective layer. The fibers are strenghtened with kevlar fibers running longitudinally, and encased in waterproof Hytrel tubing made by DuPont. The fibers for the bottom of the outer detector are 110 m long. All the rest (inner detector, side outer detector, and top outer detector) are 72 m long.

The fibers in the outer detector are tipped in a mixture of optical cement and titanium dioxide, which helps diffuse the light. The fibers in the inner detector also have such a diffusing tip, but are additionally encased in UV plexiglas cylinders which are filled with Ludox, a DuPont product which consists of 20 nm diameter silica spheres held in suspension, which provides very effective diffusion at UV wavelengths. The same basic design was used in the IMB experiment. After the main detector construction was finished, but before tank-filling began, several “dry” runs were taken with a different diffuser ball design, which used reflecting mirrors from an IMB design to bounce the light back and forth in the Ludox. A new laser ball has been designed by Mark Rosen at UH, with improved isotropy over previous models. The different designs are shown in Figure ??.

The top of the detector has several penetration holes built in. Twelve holes around the circumference of the top of the tank and one hole near the middle of the top are used to feed the fibers into the outer detector. These feedthroughs are gas-sealed and semi-permanently mounted.

### 3.4.3 Inner Detector Fibers

The inner detector fiber is stored on the tank top during normal data-taking, and is fed through the central calibration hole only for laser calibration runs. The diffuser at the end of the fiber is clipped to the end of a steel wire when being lowered into the tank to a measured depth.

### 3.4.4 Outer Detector Fibers

The fibers for the top of the outer detector are fanned out from the single penetration hole. The fibers run along the top of the detector and are suspended by steel cables. The side outer detector diffusers lie at two depths: one-quarter of the way down the wall, and three-quarters of the way down the wall. There is a ring of 12 fiber mounts at each level going around the tank. This ensures that most tubes sees at least two fibers – this redundancy was necessary because it is very difficult to replace the fibers. Such an operation must wait until detector maintenance downtime. The bottom outer detector fibers run down the side of the detector in the veto region, and are then distributed in the bottom OD to provide overlapping coverage for each tube. They are mounted pointing upwards from a cable guide struts. The OD fiber mountings are shown in Figure 3.4.

14 fibers are mounted in the bottom outer detector, 14 in the top, and 24 on the side walls for a total of 52 fibers. The general layout is represented in Figure 3.3.

# Laser Calibration DAQ

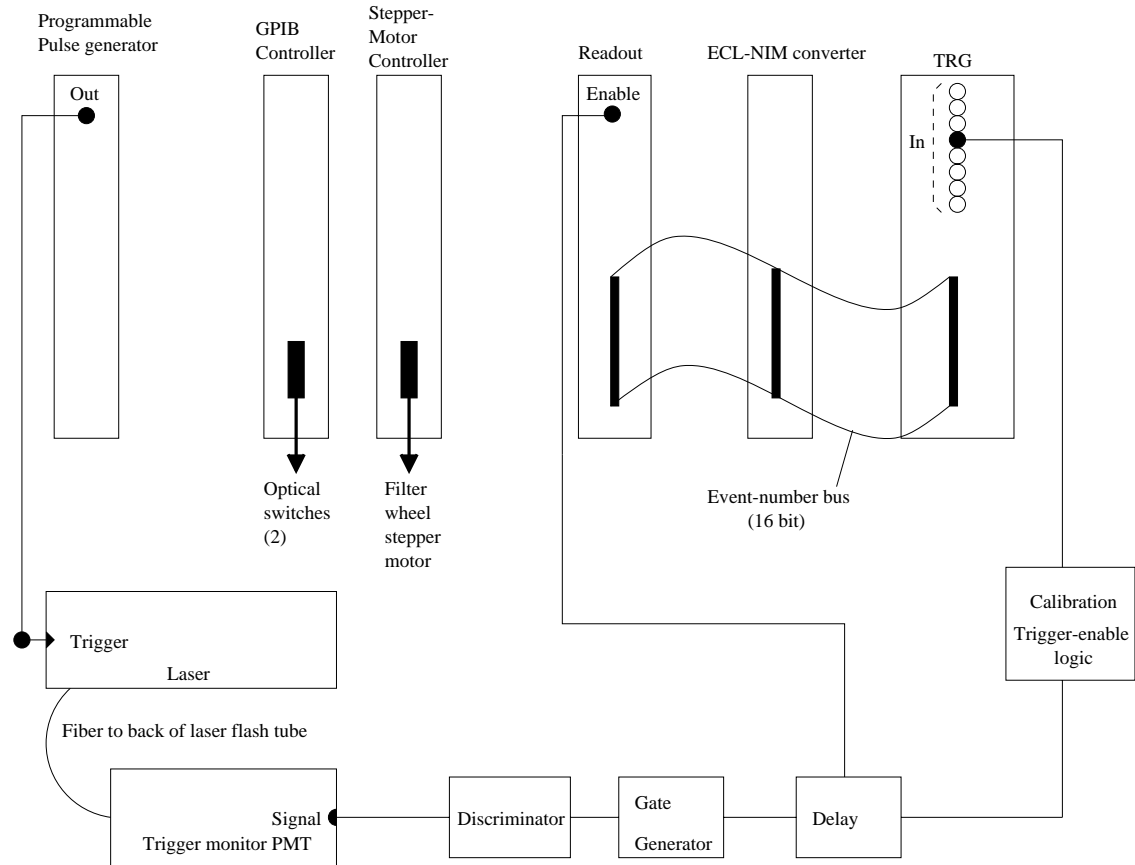


Figure 3.1: Laser Calibration DAQ

# Laser and Optics

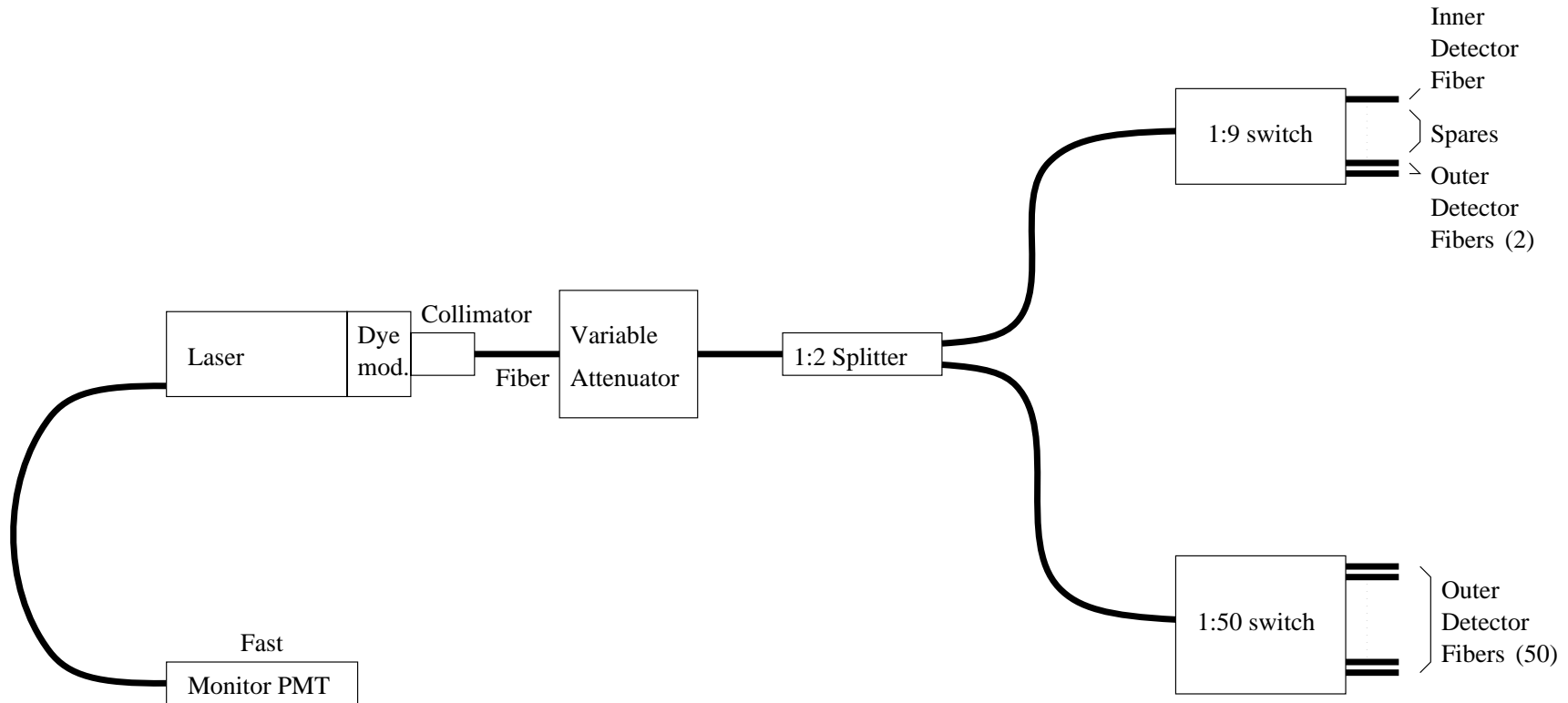


Figure 3.2: Laser Calibration Optics

# FIBERS

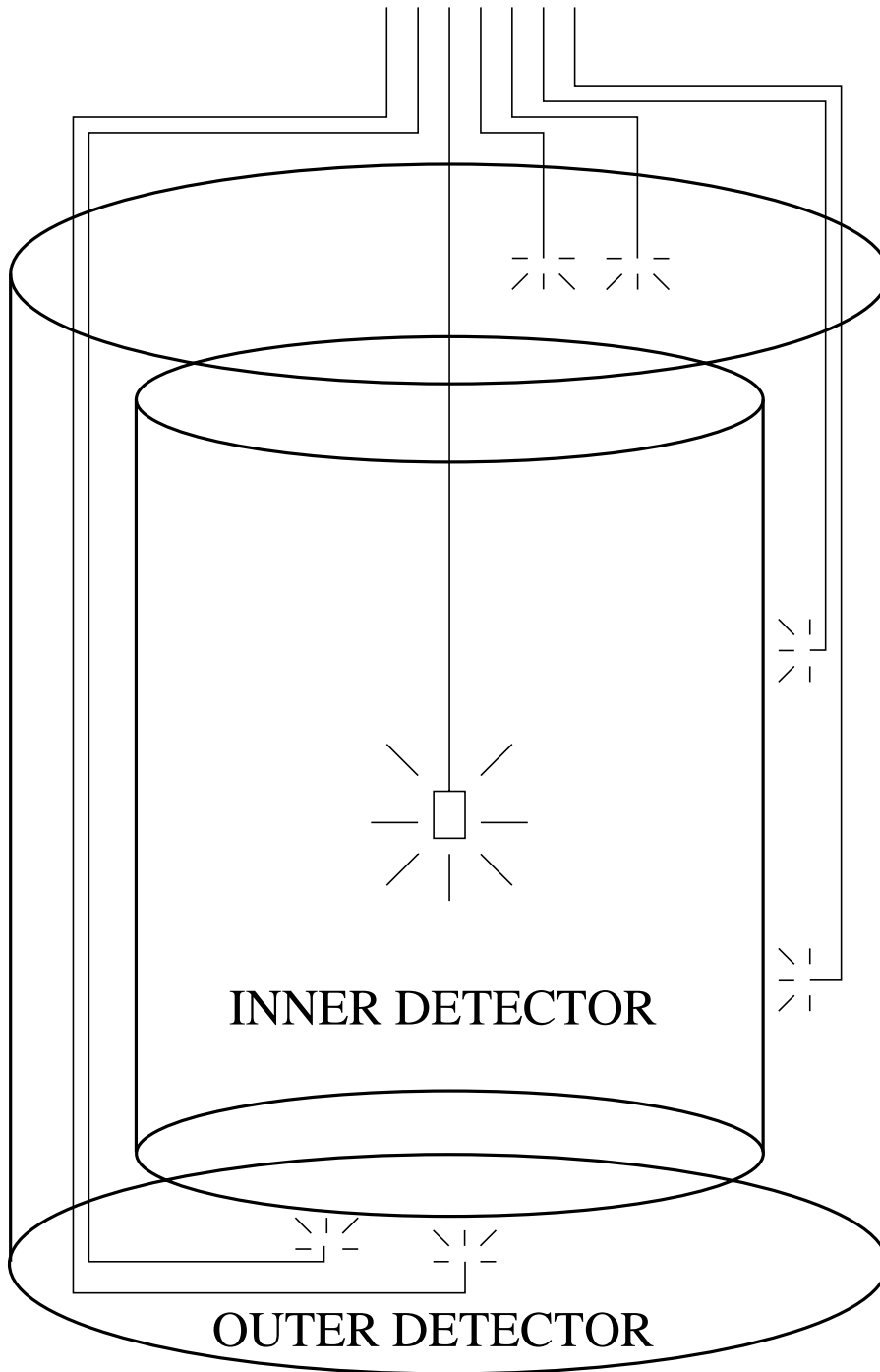


Figure 3.3: Laser Fiber Runs

## Outer Detector Laser-ball Mounting

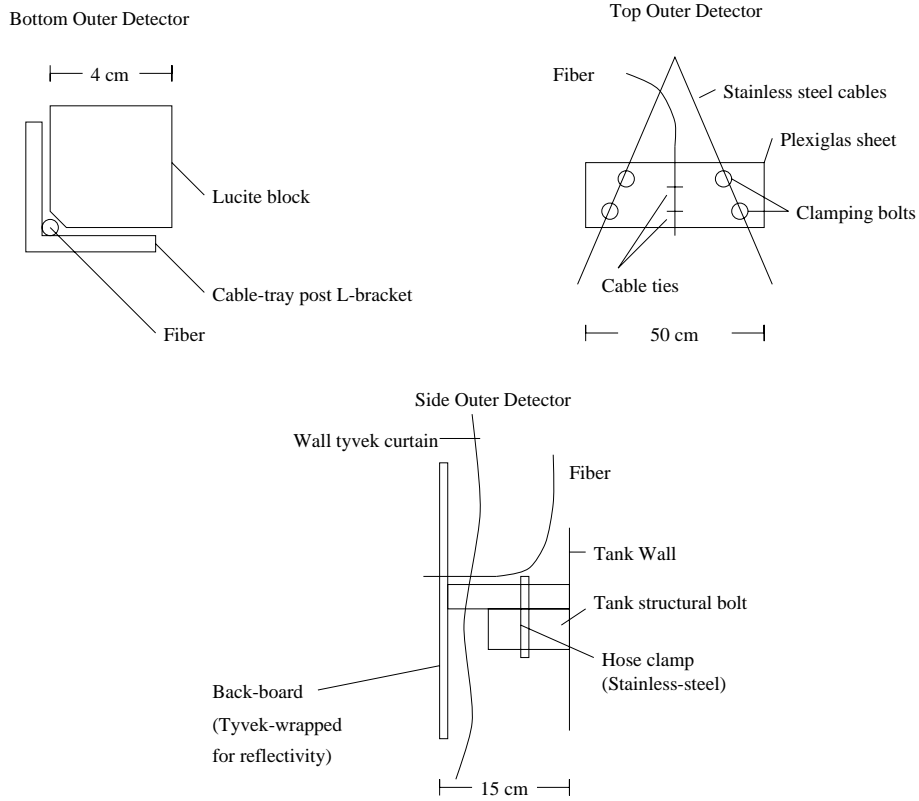


Figure 3.4: Laser Calibration OD Fiber Mounts

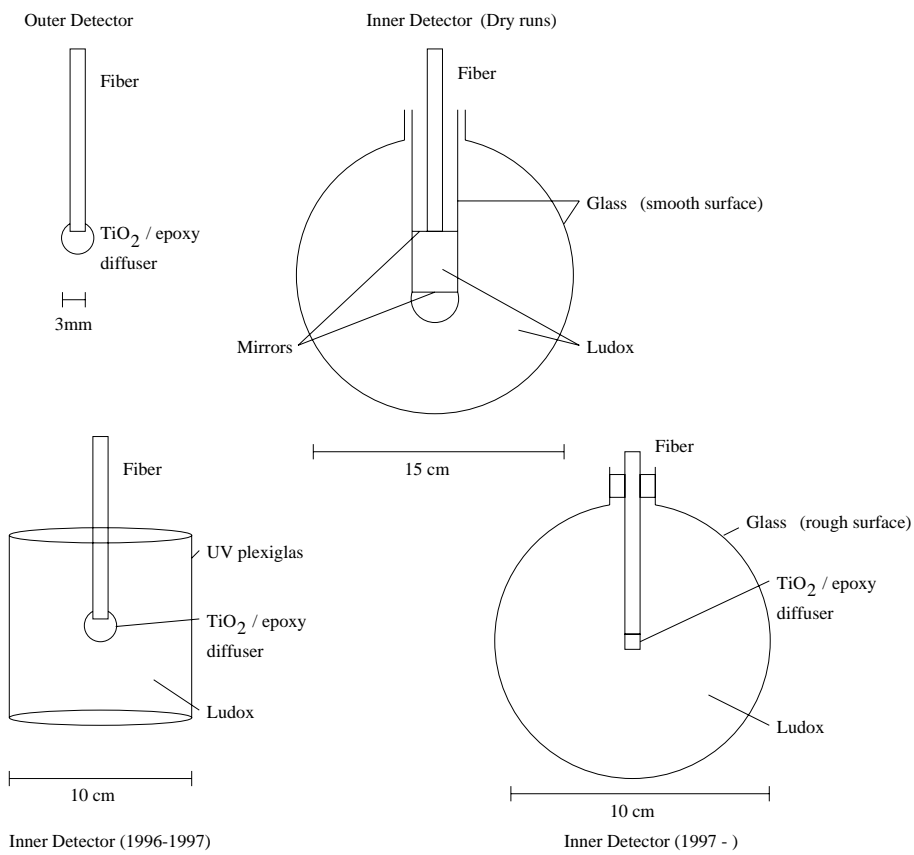


Figure 3.5: Laser fiber diffusers in use

### 3.4.5 Laser Calibration Operation

The filter wheel, optical switches and laser triggering are all controlled by a program called “lasercal,” which can be run in manual mode or accept a calibration schedule file. The 16-bit event number from the TRG is latched and read out from the CAMAC crate in order to be able to assign the filter wheel and optical switch settings to the corresponding event numbers. The output of the filtercal program is a listing, for each laser event, of the latched event number and the filter and switch settings.

The calibration events are retrieved offline and matched to the corresponding entries in the filtercal log file for the determination of outer detector calibration constants. The calibration constants are then used in the as part of the generation of the collaboration-wide common data set. This provides a uniform set of calibration constants for the various analysis groups in the collaboration. The calibration constants are stored in files on the calibration reformatting computer, and they are tagged with version numbers. These version numbers are used to associate the correct set of calibration constants with the data from different time periods. The version numbers for both inner and outer detector constants get written into the event header for later reference.

A series of outer detector gain measurements were made in the month after detector turn-on. These measurements are extremely time-consuming – one hour per fiber – so the fibers were in tandem, one fiber on each side of the detector firing at the same time.

Relative timing calibrations go much more quickly, since only one data set at one light level is needed for each fiber. Using a filtercal schedule to switch between fibers, a timing calibration completes in a little over an hour. Several timing calibrations were taken in the first few months of turn-on, as trigger hardware changes required.

# Chapter 4

## Analysis

For the first year of data-taking, two separate sets of analysis groups formed to analyze the high energy data from Super-Kamiokande, in order to detect possible mistakes and provide a comparison of reduction and reconstruction techniques. One group was the “onsite” group (led by ICRR), and the other group was the “offsite” group, consisting of several institutions including BU, SUNY Stony Brook, UCI, University of Warsaw, Los Alamos National Laboratory, and UH. The codes for both data and Monte Carlo were completely independent, as was the determination of the energy scale and systematic uncertainties. The common starting point for each analysis was the raw data with electronics calibrations (ns and p.e.) applied.

In addition to the parallel onsite and offsite high energy groups, there have also been parallel low-energy groups, which study solar neutrinos and monitor for possible supernovae, and upward-going muon groups, which study muons that have been generated in the rock below the detector by the interactions of atmospheric neutrinos which have travelled through the earth from the other side. The high energy groups engage in the study of tracks that originate within the detector from the interactions of atmospheric neutrinos. They also search for signs of nucleon decay.

The collaboration decided that the the onsite and offsite groups would gradually merge after the first year of data-taking. The high energy group has officially already done so, and so the “offsite” reduction and analysis discussed below should be understood to be those of the “old-offsite” group, as it is now called.

## 4.1 Reduction

Super-Kamiokande receives about 1 million event triggers per day. The greatest number of triggers comes from very low-energy background sources such as radon, gamma-rays from the surrounding rock and the glass of the PMTs, electronic noise, and solar neutrinos (about 30 per day). At the other end of the energy spectrum, the events which take up the largest amount of space on tape are incoming cosmic-ray muons (about 3 per second), which have long track lengths and light up a large number of tubes. Another source of high-energy noise events is “flashers,” tubes which have begun to break down and occasionally emit light. Flashers can generate light patterns which look like contained tracks; as soon as they are discovered they are turned off, and several methods are employed to identify flasher events in the reduction.

The purpose of the of the offsite high-energy data reduction code is to quickly filter these events out to get a manageable subset of contained and partially-contained (exiting) event candidates. The philosophy of the early stages of reduction is to only reject background candidates which are understood well enough that they can safely be rejected, with the goal of saving every event of possible interest to the study of atmospheric neutrinos, and also for the search for proton decay.

In the first stage of the offsite data reduction (“HIGHE1”), events are first filtered for obvious problems such as having no inner-detector or outer-detector data. The majority of entering cosmic ray muons are removed by requiring that there be fewer than 10 hits in the outer detector in a 200 ns window around the trigger time. A first pass at filtering out flashers is made by requiring that the the tube with the most charge must have less than  $0.4\times$  the total charge of the event. Events with fewer than 15 tubes in a  $\pm 12$  ns time-of-flight residuals window from anywhere in the detector are rejected as noise, as are events with fewer than 100 p.e. in  $\pm 20$  ns time-of-flight residuals window around a point-fit vertex. Events falling within 100 microseconds of a previous event excluded from consideration as contained events, but are kept and tagged as  $\mu$ -decay electron candidates.

The output of HIGHE1 is about 80,000 events per day. This large number is mainly due to the saving of one in every thousand events to form a minimum-bias sample. The minimum-bias events are removed in the next stage of filtering, HIGHC2, which is designed to restrict the data set to those events which are fully-contained.

In HIGHC2, a vertex point fit is done based on timing residuals. A minimum of 150 photo-electrons must be collected in the inner detector within a  $\pm 20$  ns timing-residuals window from this vertex. A muon track fit is applied, and events passing the fit with more than 2 outer-detector hits in a  $\pm 50$  ns window within 20 m of the projected entry point are rejected as entering events. Events which have been found from a separate analysis to have the repetitive patterns of specific flasher events are culled. The output of HIGHC2 is about 20 events per day.

In HIGHC3 a precise single-track event fitter, “yastef” (originally developed for IMB[44]) based on timing residuals and event geometry, is applied to the remaining events. The vertex resolution of this fitter is about 70 cm; Figure 4.1 shows vertex fit errors, parallel fit errors (along the track) and angular fit errors for simulated muon and electron tracks of energy around 1 GeV. As can be seen, the error is primarily parallel to the track, and depends on the event type; muon fits tend to get pulled forward along the track, and electron events tend to get pulled backward.

Tables 4.1 and 4.2 show angular resolutions (defined as the point where 68% of the events have a smaller angular deviation) and vertex deviation parallel to the track for muons and electrons in ranges of visible energy from 50 to 5000 GeV. (The visible energy of an event is defined as the energy of an electron which produces the equivalent amount of light in the detector.)

At the end of HIGHC3, events with yastef vertices less than 50 cm from the inner detector PMT wall are removed. This leaves about 10 events per day.

In HIGHC4, a final track fitter is applied to events with greater than 15000 p.e., to test whether they might be entering muons. If the vertex of this fit is within 1 m of the wall, the event is rejected. Otherwise, the results of the yastef fit are used to determine the position of the event. Events with a yastef vertex within 50 cm

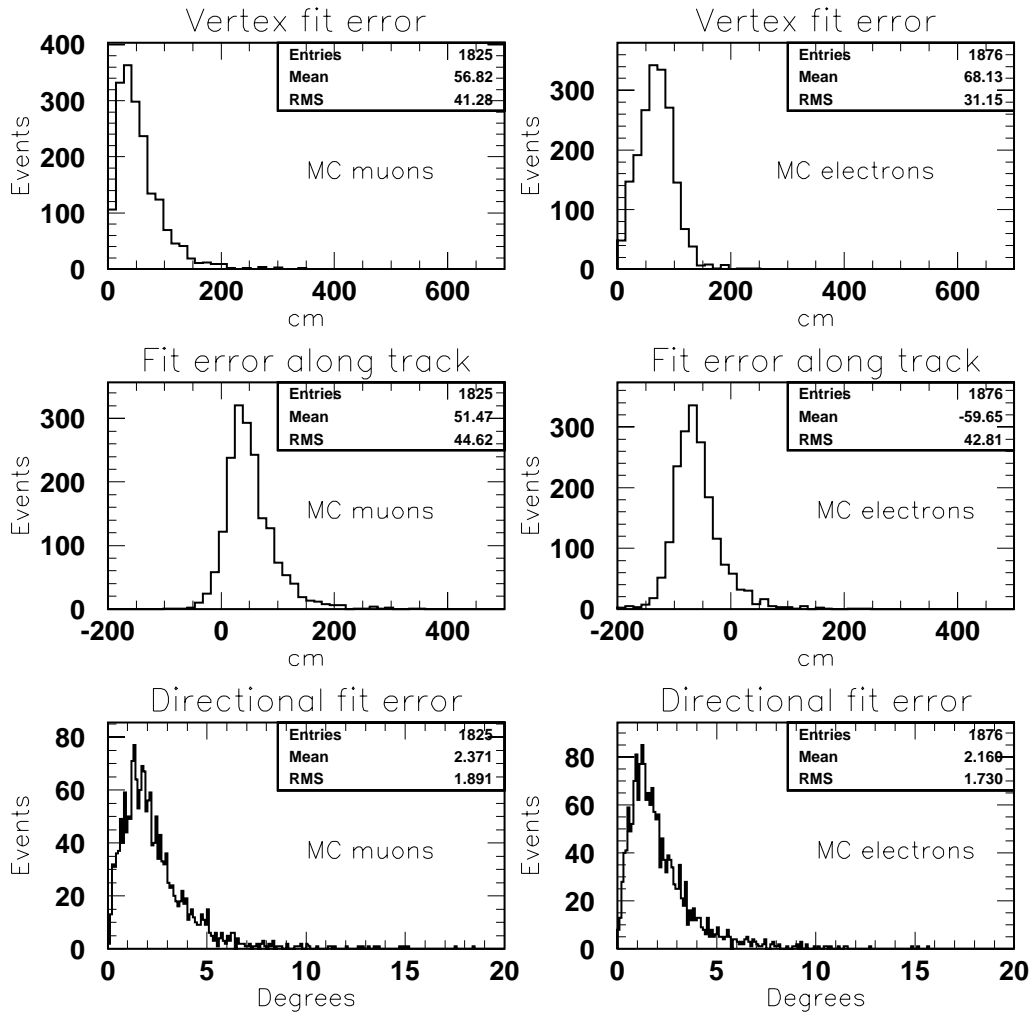


Figure 4.1: Yastef vertex and direction errors on  $\sim 1$  GeV MC muons and electrons.

Table 4.1: Fitter errors on MC muons.

$E_{vis}$ (MeV)	Ang. Res. (deg.)	Vertex creep (cm)	RMS (cm)
50-100	3.6	146	86
100-300	2.9	57	40
300-500	2.8	35	30
500-1000	2.6	42	36
1000-1500	2.9	73	54
1500-3000	3.5	125	97
3000-5000	4.6	218	141

Table 4.2: Fitter errors on MC electrons.

$E_{vis}$ (MeV)	Ang. Res. (deg.)	Vertex creep (cm)	RMS (cm)
50-100	7.1	-82	55
100-300	5.5	-82	47
300-500	3.7	-68	45
500-1000	2.7	-60	45
1000-1500	2.0	-55	39
1500-3000	1.7	-51	40
3000-5000	1.7	-32	46

of the wall are rejected. A final flasher test is also performed, to find events with characteristically broad timing residuals distributions.

The final sample is restricted to events 2 m from the PMT wall, corresponding to a 22.5 kton fiducial mass. This results in 2707 fully contained events, including those originating from atmospheric neutrino interactions. Several visual event-scanning sessions were held throughout the year to verify and tune the performance of the reduction system. However, by the end of the data-taking period under discussion, the percentage of background events found by scanning had been reduced to 0.2%. The reduction is now fully automatic, a departure from previous experiments. The remaining contamination is treated as a systematic error, and not removed.

Figure 4.2 shows the distribution of fully-contained events within the fiducial volume, 2 meters from the inner optical barrier. The vertical scale is the  $Z$ -coordinate of the event vertex, and the horizontal scale is the square of the horizontal distance of the event vertex from the centerline of the detector; such a scale maps the cylindrical interior of the detector into equal-volume bins. The distribution is smooth over the cylindrical volume.

The integrated livetime for this sample is calculated to be 301.4 days, or 18.5 kton-yrs. For comparison, Kamiokande and IMB each accumulated a little under half that amount over their entire lifetimes.

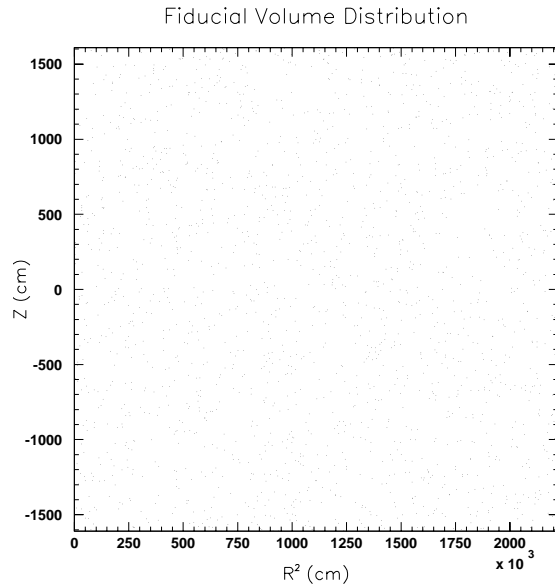


Figure 4.2: Distribution of fully-contained events within the fiducial volume.

## 4.2 Event Classification

### 4.2.1 Single-ring Finding

An algorithm called “ringer” is used to select single-ring (quasi-elastic candidate) events, based on the azimuthal distribution of light which falls behind the Cerenkov cone of the track; events with azimuthal symmetry are considered single-ring, and those with a higher asymmetry are considered multi-ring. The algorithm, developed at BU, looks at the charge deposited in the tubes from 50 deg off the track direction to 130 deg off the track direction, in a sliding window 40 deg wide. The tube charges are corrected for tube coverage and water attenuation, and a  $\chi^2$  measure of the maximum “imbalance” found is returned.

The single-ring and multi-ring results of these cuts agree with human scanners for 90% of the events, which is similar to the agreement level of two independent human scanners. Based on Monte Carlo (M.C.) studies, the single-ring sample from this

algorithm is estimated to contain 77% quasi-elastic interactions, 15% non-quasi-elastic charged-current interactions, and 8% neutral-current interactions.

Figure 4.3 shows an example of a multi-ring event which is rejected by this criterion. Figure 4.4 shows the location of the cut on data and MC samples.

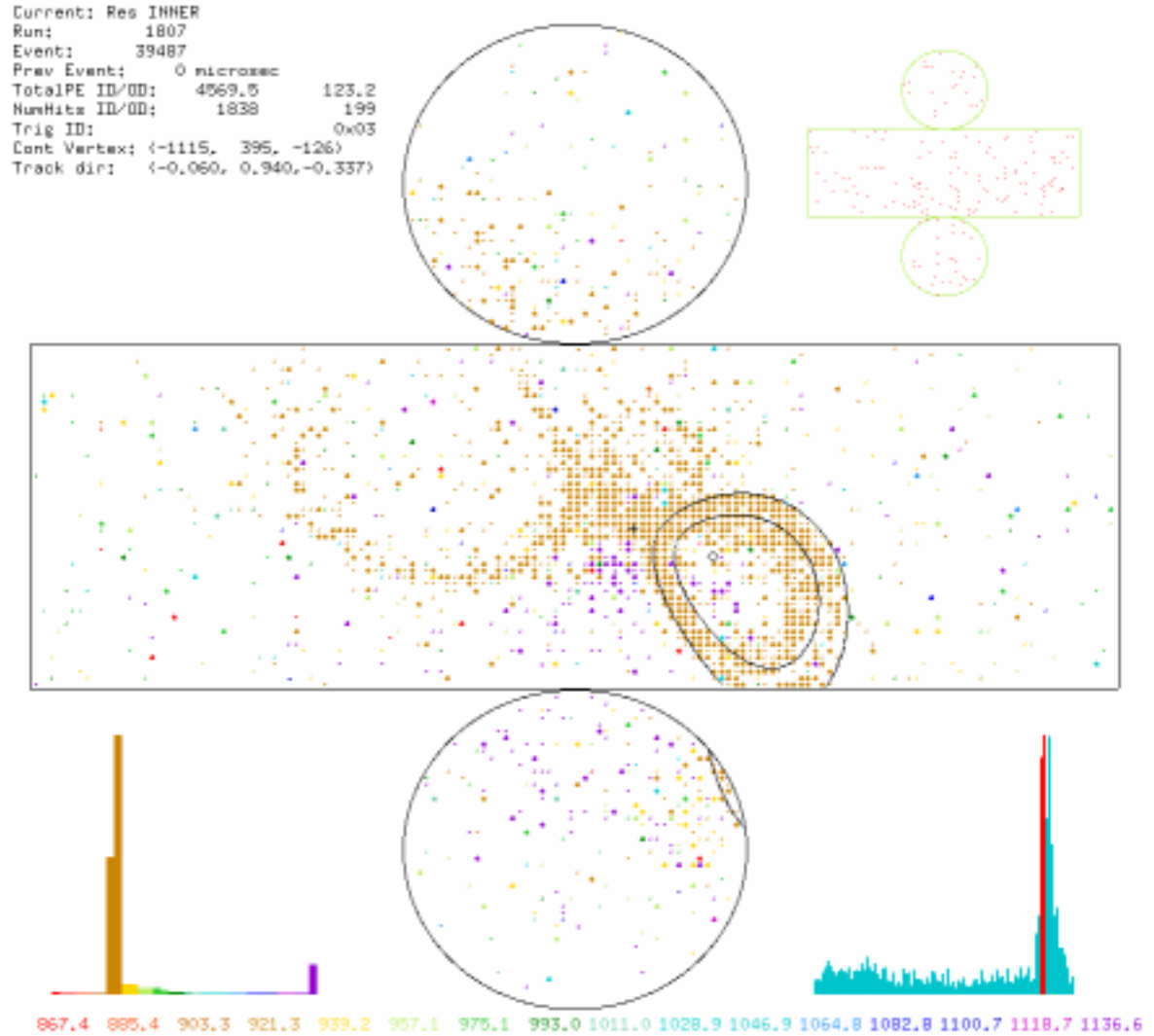


Figure 4.3: Example of an event classified as multi-ring.

## Single-ring cuts

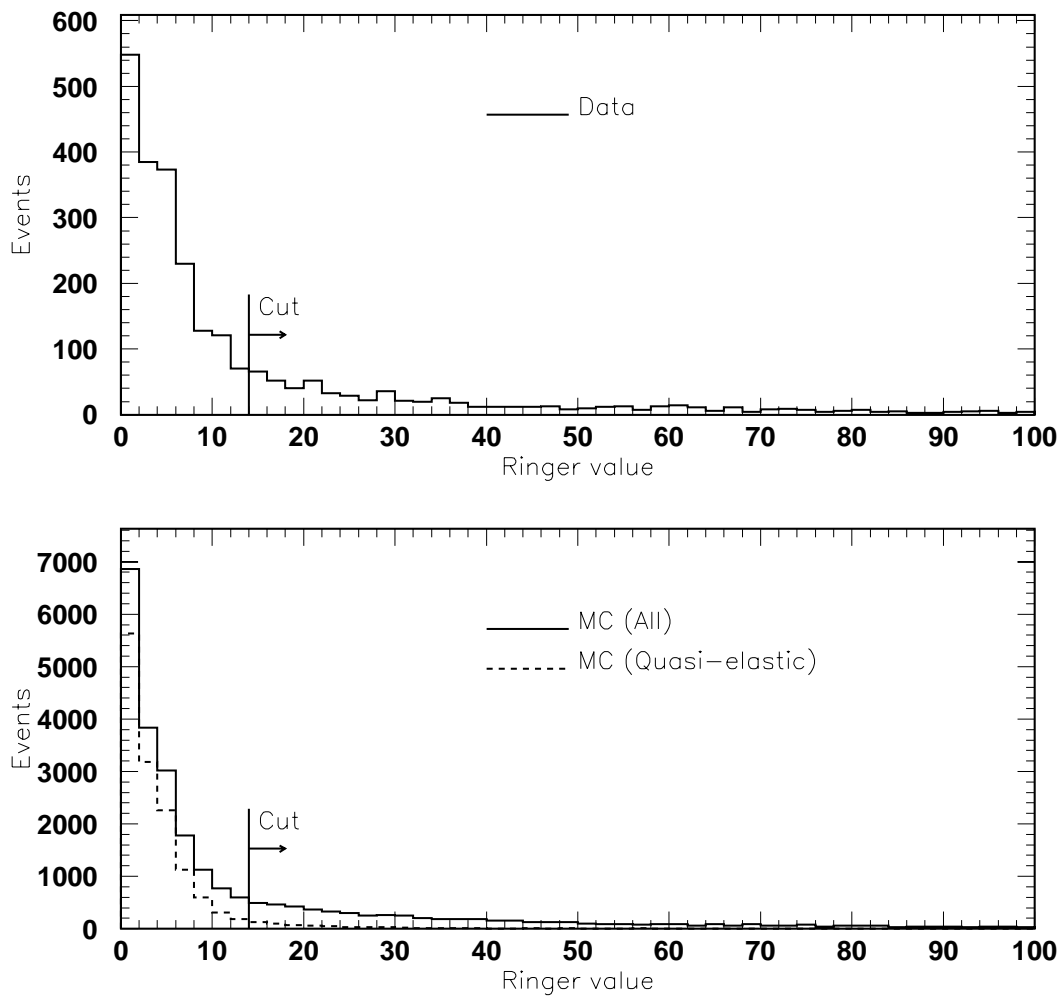


Figure 4.4: Ringer values for data and monte carlo samples. Single-ring events have a lower ringer value, and multi-ring events have a higher value.

### 4.2.2 Muon Decay

The identity of the incoming neutrino in a quasi-elastic charged-current interaction is determined from the type of lepton produced. Muon-(anti-)neutrinos give rise to (anti-)muons, and electron-(anti-)neutrinos give rise to electrons(positrons) according to:

$$\nu_\mu + n \rightarrow \mu^- + p$$

$$\bar{\nu}_\mu + p \rightarrow \mu^+ + n$$

$$\nu_e + n \rightarrow e^- + p$$

$$\bar{\nu}_e + p \rightarrow e^+ + n$$

The outgoing leptons can be identified in several ways. The easiest to use in a water-Cherenkov detector are event topology and (in the case of muons) the detection of further decay electrons:

$$\mu^+ \rightarrow e^+ + \nu_e + \bar{\nu}_\mu$$

$$\mu^- \rightarrow e^- + \bar{\nu}_e + \nu_\mu$$

The decay electrons are found in two ways: either as an extra track later in the same event if they are generated within about 1 microsecond of the original muon track, or else they can generate triggers and be found as “after-events” if they are produced later than that. These events can be identified by their characteristically low energies (up to 52 MeV), and by their timing relative to the previous event: the  $\mu^+$  lifetime is  $2.19703 \pm 0.00004 \mu\text{-sec}$ [45]; the  $\mu^-$  can be captured by a nucleus before it decays, and so has a shortened measured lifetime in pure water of  $1.7954 \pm 0.0020 \mu\text{-sec}$ . [46] The  $\mu$ -decay search software is thus divided into two parts: “samedk” (developed at BU) and “afterdk” (developed at UH).

The samedk algorithm uses the vertex of the original muon to find timing-residuals peaks later in the same event. It works well for low-energy (sub-GeV) events, because the muon tracklength at those energies is short ( $< \sim 2$  m) and the decay electron vertex (if there is one) will not be far away. At higher energies the distance between

the muon and electron vertices increases, but the number of tubes “used up” by the original event also increases as the event gets brighter; tubes which have been hit already in an event are unavailable for recording further hits from any later track.

The `afterdk` algorithm uses a low-energy point-fit, “hayai,” developed at LSU for the study of solar neutrinos. The details of its operation are given in Ref. [47]. The total charge of all tubes within a  $\pm 25$  ns time-of-flight residuals window from the vertex, corrected for water attenuation and tube coverage from the fit vertex, is required to be greater than 80 p.e., which corresponds to a lower-energy cut of about 10 MeV. If the event is in the sub-GeV range, the hayai vertex is required to be found within 8 meters of the original event. (The vertex resolution of “hayai” is better than 1 meter for events over 10 MeV.) This requirement is waived for higher-energy events where the muon tracklength is longer. After the discovery of a decay candidate, the candidate “after event” is cleared of all tubes within an 80 ns residuals window centered around the hayai vertex, and the event is searched again for a new decay candidate. Figures 4.5 and 4.6 show an example of a muon/after-decay pair.

It sometimes happens that a decay electron will appear late enough in a primary event to generate a new trigger, and straddle the two events, with half its hits in the first event and half in the second. Such events are called “bye-bye” events (after the convention of T. Hayakawa of the onsite group), and they are found by comparing the times when `samedk` and `afterdk` both find a decay candidate. If the two candidates are within 100 ns of each other, a hayai fit is applied to the `samedk` event, and the event is awarded to the event with the better hayai goodness-of-fit.

However, “bye-bye” events are rejected by a set of timing cuts designed to restrict the attention to regions of relatively flat efficiency. The `cleandk` cuts are: 250-800 nsec and 1.2-6  $\mu$ -sec. The light travel time across the detector from corner to corner is 210 nsec, so decays within 250 nsec of the original event are found with low efficiency and high background, since light from the original event is still traversing the detector. Events between 800 and 1200 nsec fall into the “bye-bye” region between events; not only is the software detection efficiency lowered there by the spreading of one track across two events, but there is also a detector trigger

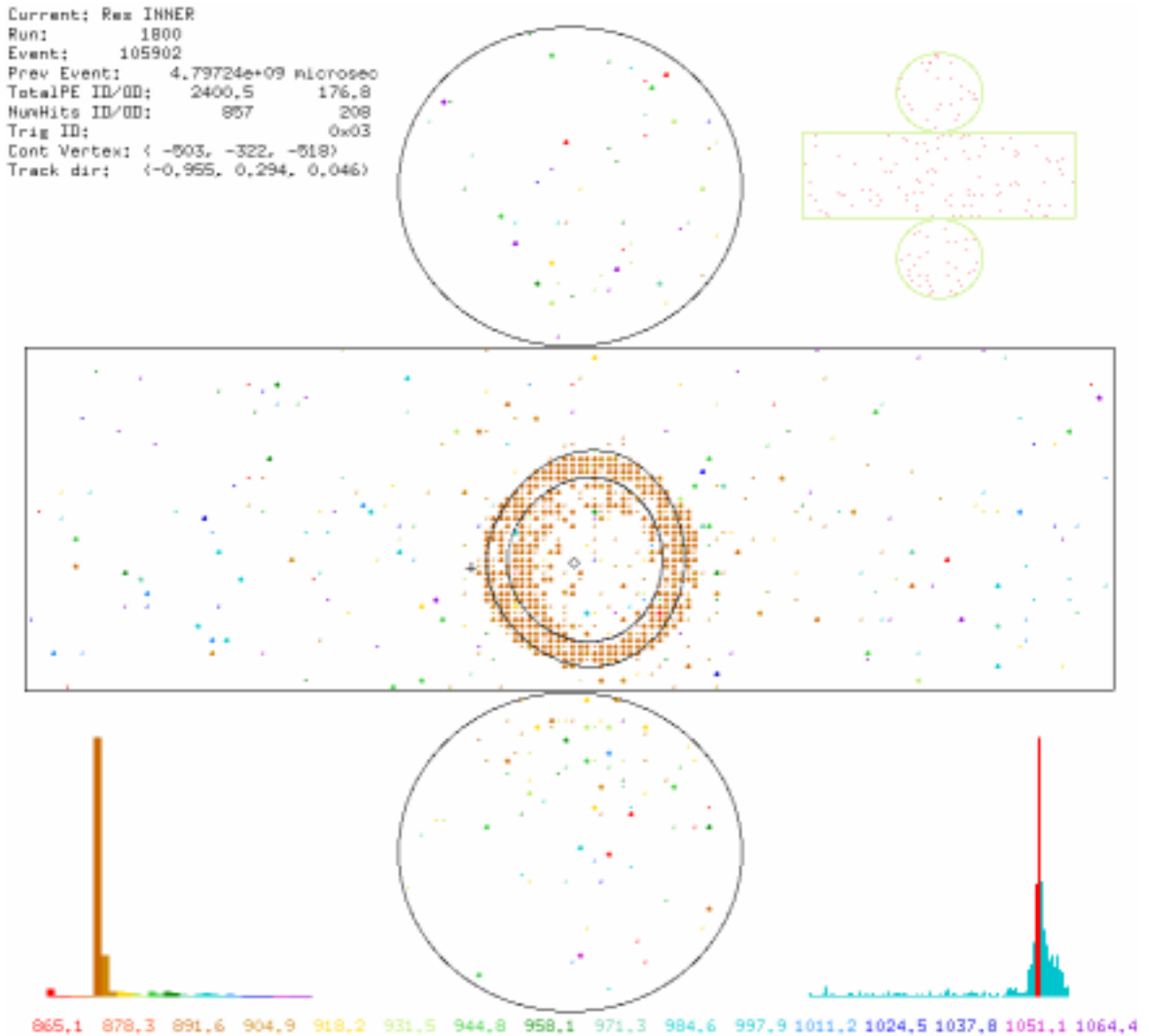


Figure 4.5: Example of an event identified as muon-like.

inefficiency in this region which grows with the size of the event. Finally, the time cut at 6 microseconds is due to the rejection of all events with no outer-detector data in the earliest stages of data reduction: for those runs which are subsequent to the outer-detector data-taking window being shortened to end 6 microseconds after than the primary event trigger (see Chapter 2), outer-detector data is missing for the 2-3 microsecond digitization period following the 6-microsecond mark.

To study the relative efficiencies of the detection of decay electrons between data and monte carlo, cosmic ray muons which have stopped in the detector were studied. (See

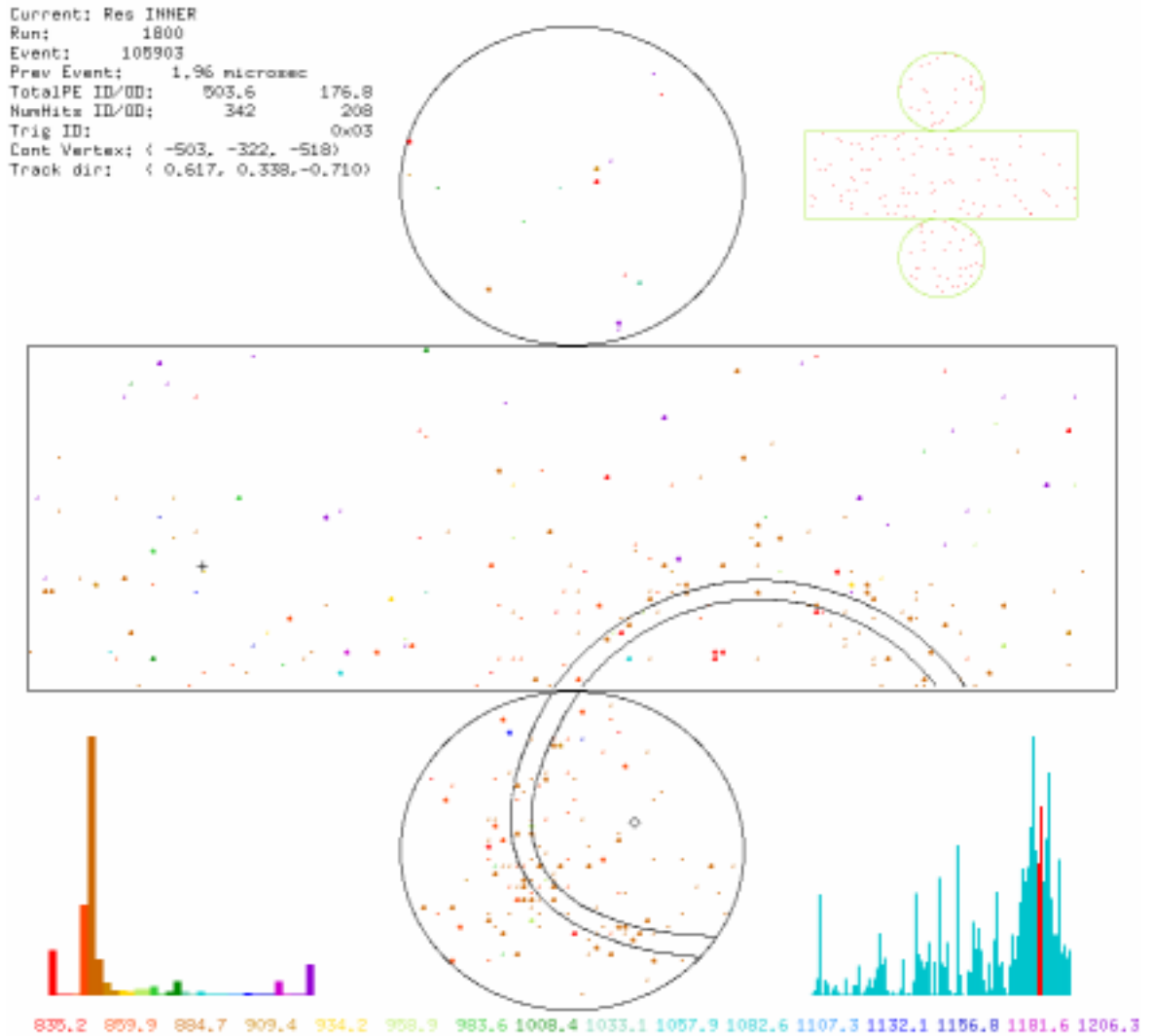


Figure 4.6: Example of an event classified as a decay-electron, following previous muon event.

Figure 4.7 for an example.) Such events have previously been studied at Kamiokande where the charge ratio  $R(\mu^+/\mu^-)$  and polarization of stopping cosmic ray muons were measured from a study of the resulting decay electrons. In that study, the charge ratio was measured by fitting the decay curve to a two-component lifetime equation of the form:

$$N(t - (t + \Delta t)) = N_+[1 - e^{(-\Delta t/\tau_{\mu^+})}]e^{(-t/\tau_{\mu^+})} + N_-[1 - e^{(-\Delta t/\tau_{\mu^-})}]e^{(-t/\tau_{\mu^-})},$$

where  $\Delta t$  is the binning width of the decay-curve histogram,  $N_+$  and  $N_-$  are the total number of positive and negative muons, respectively, and  $\tau_{\mu^+}$  and  $\tau_{\mu^-}$  are the  $\mu^+$  and effective  $\mu^-$  lifetimes, respectively. From a sample of  $1.6 \times 10^5$  muon-electron event pairs, they determined the charge ratio  $R(\mu^+/\mu^-)$  for the muons stopping at Kamiokande (400 m down the tunnel from Super-Kamiokande) to be  $1.37 \pm 0.06$  (stat)  $\pm 0.01$  (syst).[48]

Stopping cosmic-ray muons are not saved in the offsite high-energy reduction, so a sample of 16,500 provided by Robert Svoboda of LSU and the offsite low-energy group was used as a test sample. These were fit with the LSU muon fitter “muboy,” which is described in Ref. [47], but which provides entry points and end points of stopping muon tracks to better than 1 meter resolution. Such a sample is not directly comparable to the contained event sample, having different vertex, end-point and energy distributions, but it can be used to compare the relative detection efficiencies between the data and the monte carlo.

The muboy tracks were used to generate MC stopping muons for a comparison sample. The charge ratio  $R(\mu^+/\mu^-)$  in the MC sample was set to 1.37, in accordance with the Kamiokande measurement; a  $\mu^-$  capture in the MC is simulated by a fake “decay” of the  $\mu^-$  to two neutrinos, which effectively makes it disappear in the event simulation. There is no way to match the charges of the muons in the monte carlo with those in the data track-for-track, but this does not matter as long as the track distribution does not depend on the sign of the muon – a dependence which there is no reason to expect.

From these samples, the detection rate of decays is estimated to be 70% for  $\mu^+$  and 57% for  $\mu^-$ . Contamination is less than 1%, as measured by the instances of multiple decay candidates for a single stopper. Detection efficiencies between monte carlo and data agree within 3 %. This is taken as the systematic error on the relative detection rate between data and monte carlo.

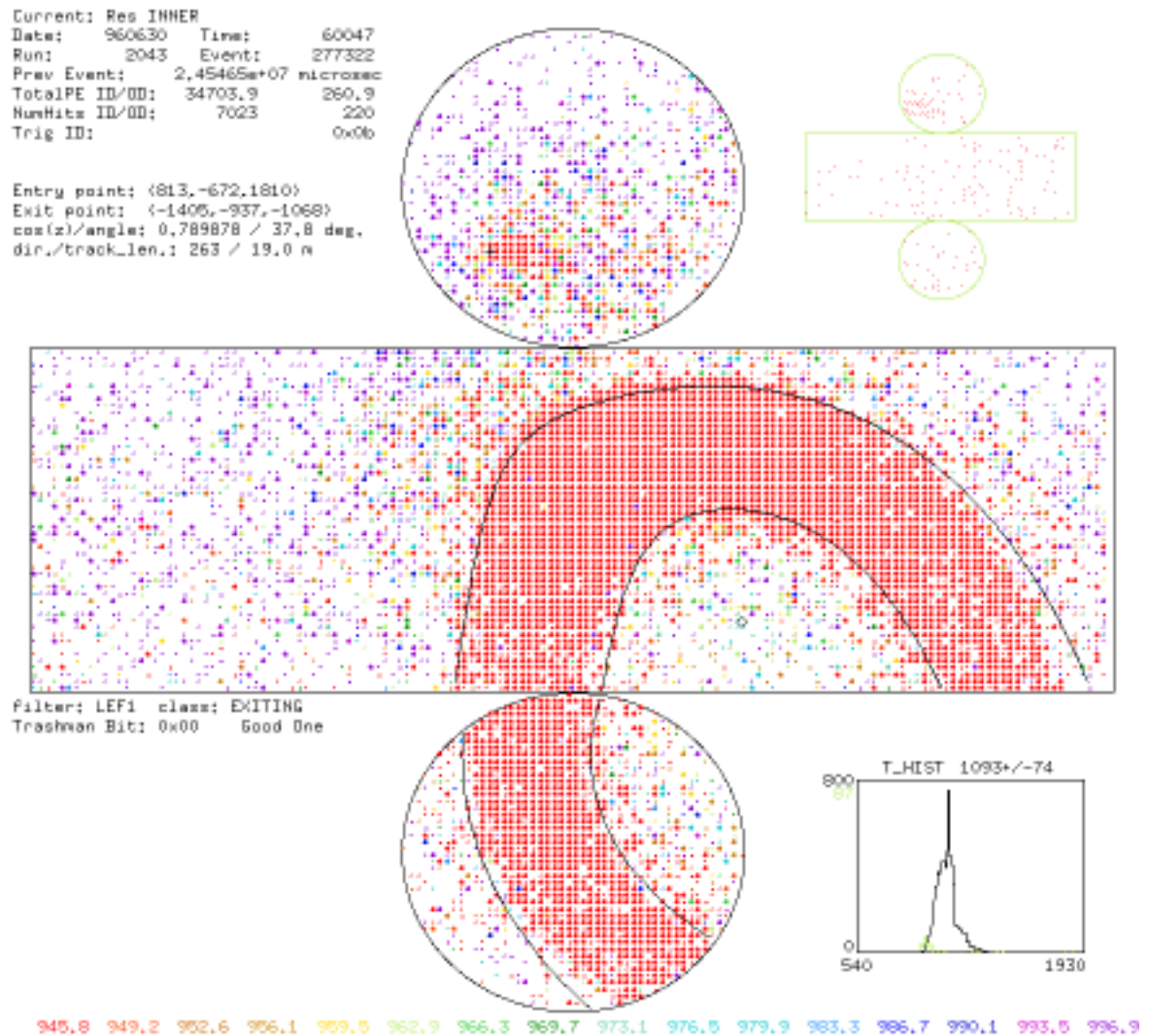


Figure 4.7: Example of an entering muon which has stopped in the tank. Note the presence of activity near the entry point in the outer detector, in the upper-right hand corner, which is absent from fully-contained events.

### 4.2.3 Particle ID

Single-ring tracks are further classified into whether they are electron-like or muon-like based on the event topology. The biggest difference between electron tracks and muon tracks is that muon tracks tend to generate fairly clean and sharp Cherenkov-cone patterns, while electrons tend to produce fuzzier distributions due to electromagnetic showers. Figures 4.8 and 4.5 show the characteristic light patterns for electron and muon tracks.

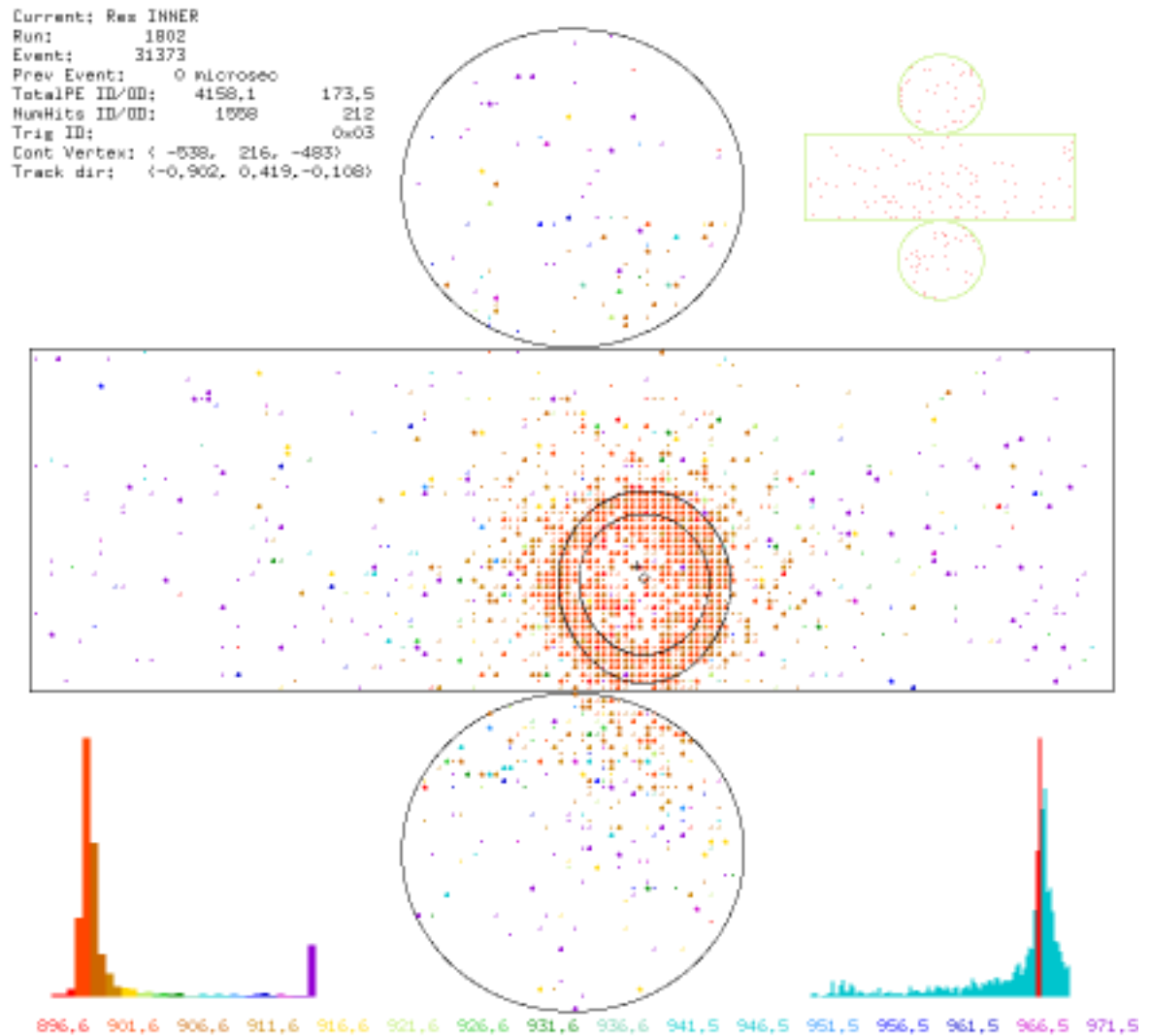


Figure 4.8: Example of an event identified as electron-like.

An algorithm called “adpid” was developed at SUNY which measures the relative amounts of Cherenkov light projected back onto the particle track before and after the vertex to determine the amount of showering.[49] Adpid takes the light from the event and projects it onto the track as though it had been emitted at the Cherenkov angle. It then compares the difference between the amount of light found 5 meters behind the vertex to that found 5 meters in front of it to distinguish  $\mu$ -like events from e-like ones. The misidentification rates for the quasielastic events in the MC which pass the reduction cuts are shown in Figure 4.9. For those events in the range 100-1500 MeV, the misidentification rates for electrons and muons are 2.4% and 1.8% respectively.

A secondary particle ID, “dochira,” was developed at UH for comparison purposes. It also uses the light pattern of the track, but applies a Kolmogorov-Smirnoff shape test to the angular distribution which is compared against the results from a set of monte-carlo muons and electrons. The misidentification rates are shown in Figure 4.10. For those events in the range 100-1500 MeV, the misidentification rates for electrons and muons are 5.5% and 4.4% respectively.

Adpid has better track discrimination especially at the bottom of the energy scale. Dochira improves somewhat with energy, where Adpid gradually worsens, especially above 5 GeV. However, by 10 GeV, contained leptons can be identified as electrons simply by the fact that they are contained – muon tracks above that energy are too long to be contained. Dochira agrees with adpid and 92 % of the time in the sub-GeV data, and 93 % of the time in the monte carlo sample.

#### 4.2.4 Energy Determination

The particle energy is reconstructed from the amount of light received at each tube, corrected for its distance from the vertex of the event. This gives first visible energy, which as mentioned before is defined to be the energy of an electron which would generate the same amount of light as the given event, regardless of the actual particle

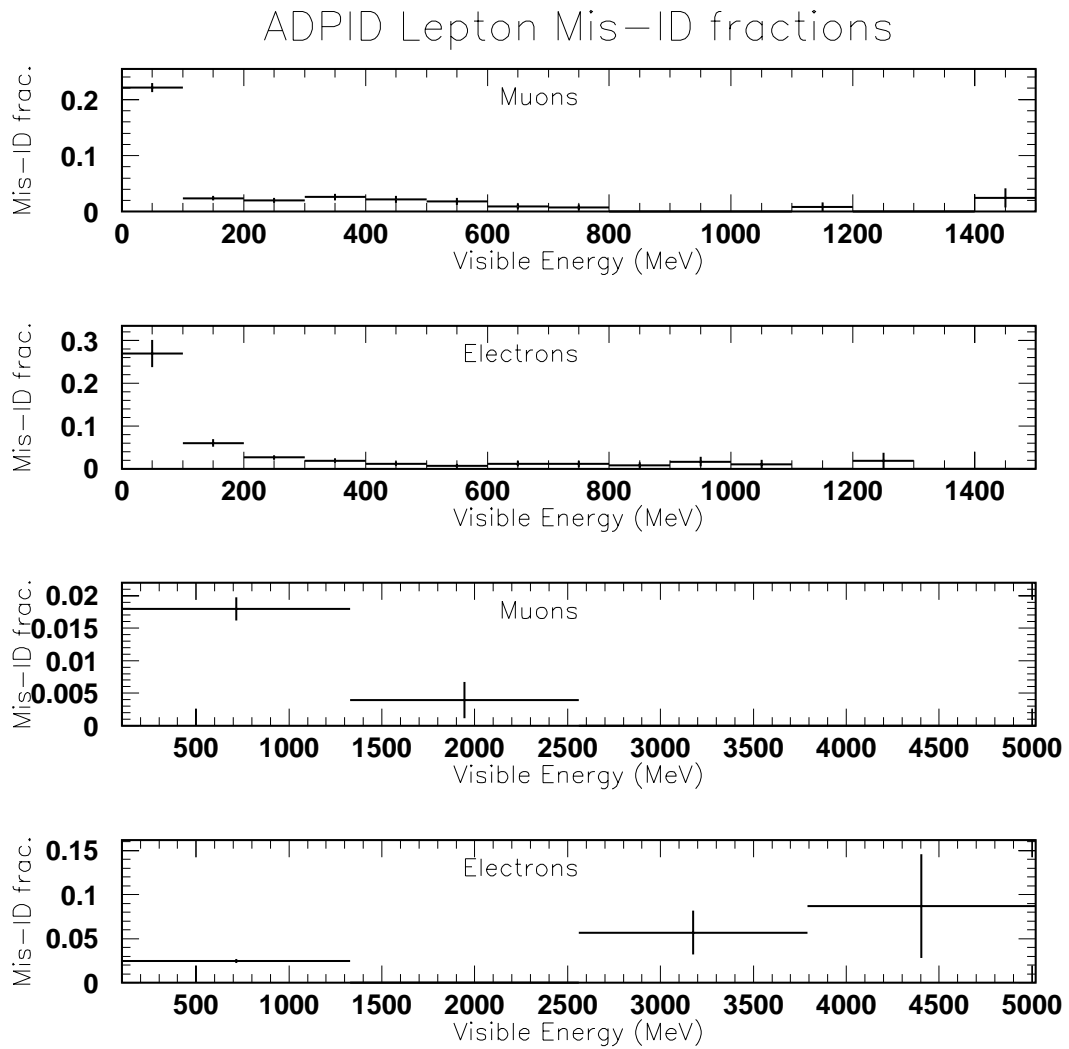


Figure 4.9: ADPID lepton misidentification rates for quasi-elastic MC events which pass the reduction cuts.

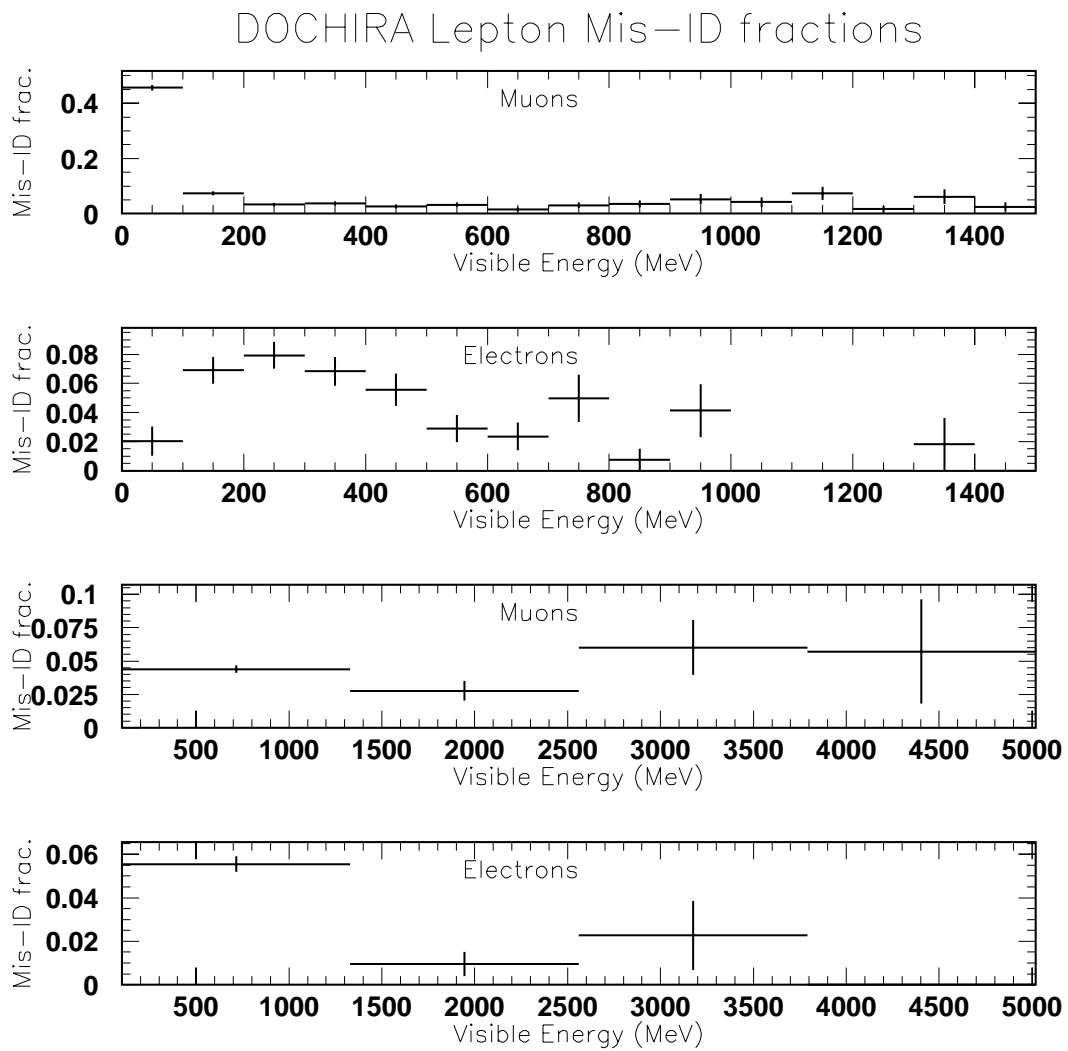


Figure 4.10: DOCHIRA lepton misidentification rates for quasi-elastic MC events which pass the reduction cuts.

type. From this, a particle momentum is assigned based on the identified particle type.

The energy scale of the monte carlo is set at the low end by calibrations using a californium-nickel source: neutrons from decay of californium are thermalized by passage through water and captured on nickel threads, leading to an excited nuclear state which emits a 9 MeV gamma ray. At the upper end of the energy scale stopping cosmic-ray muon tracks are used to set the energy scale  $>\sim 1$  GeV and above. Periodic calibrations with these sources are used to track detector gain over the course of the year, and to match water attenuation parameters in the monte carlo with that in the data. The energy calibration is checked by looking at data from a LINAC (which injects electrons up to 15 MeV directly into the detector volume), muon-decay electrons and  $\pi^0$ s produced by the neutrino interactions. The energy resolution is estimated to be  $1.74\%/\sqrt{E(\text{GeV})} + 1.1\%$ , with an estimated  $\pm 3.6\%$  uncertainty in the energy scale.

The visible energy distributions for all events and for single ring events, data and simulation, are shown in Figures 4.11 and 4.12, where all events and those with a muon decay tag are both indicated. Similarly, in Figures 4.13 and 4.14, are presented momentum distributions of the single-ring  $e$ -like and  $\mu$ -like events, data and simulation, all events and those with muon decay tags.

### 4.3 Results

After assigning particle identification, events are selected with  $0.1 \text{ GeV}/c < p_e < 1.5 \text{ GeV}/c$  and  $0.3 \text{ GeV}/c < p_\mu < 1.5 \text{ GeV}/c$ . This corresponds to the kinematic cuts used in prior analyses by the IMB experiment.[21] This analysis chain has also been performed with a minimum  $p_\mu$  of  $0.2 \text{ GeV}/c$  and a maximum visible energy of  $1.33 \text{ GeV}$ , corresponding to the Kamiokande kinematics cuts.[50] The final data sample of single-ring events, within the IMB momentum ranges, and with vertices in the  $22.5 \text{ kton}$  fiducial volume, consists of 727  $e$ -like events and 537  $\mu$ -like events.

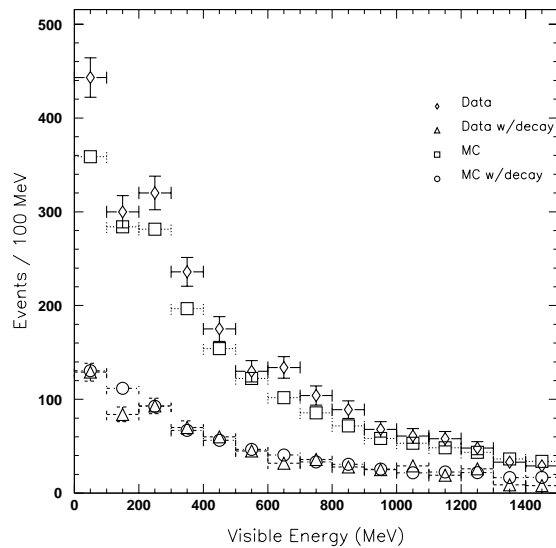


Figure 4.11: Visible energy of all events and those with mu decay.

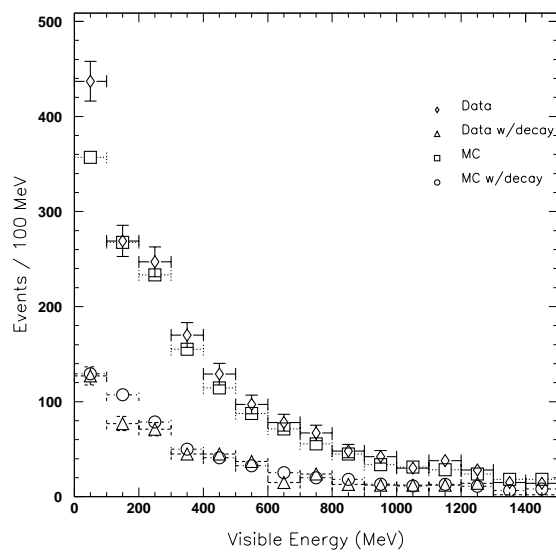


Figure 4.12: Visible energy of single-ring events and those with mu decay.

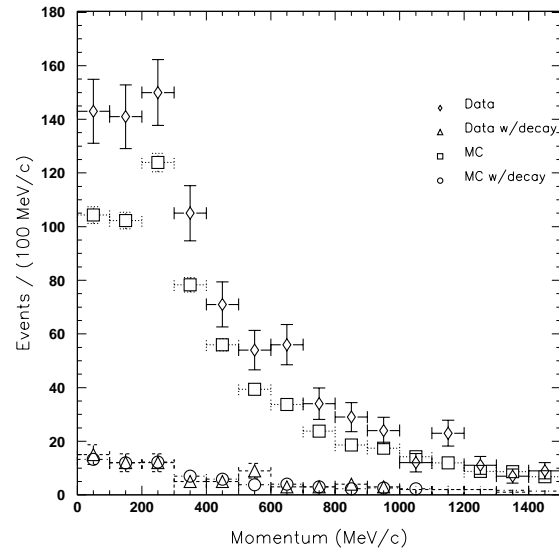


Figure 4.13: Momentum of single-ring  $e$ -like events and those with a mu decay.

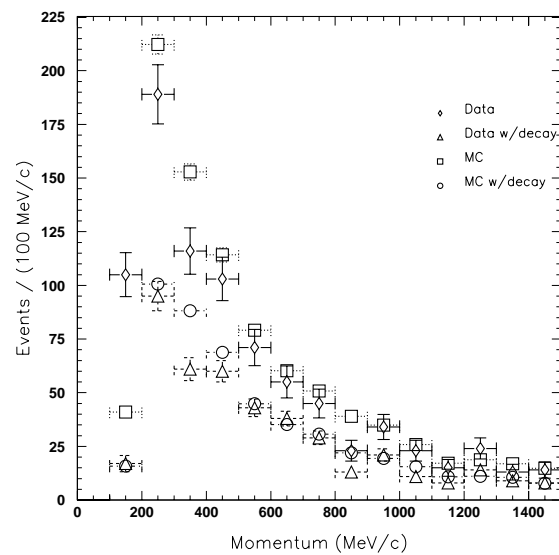


Figure 4.14: Momentum of single-ring  $\mu$ -like events and those with a mu decay.

A sample of Monte Carlo events corresponding to 7.75 years worth of exposure was generated, using the atmospheric  $\nu_\mu$  and  $\nu_e$  flux models of Agrawal, Barr, Gaisser, Lipari and Stanev[13,12,51] and the pion-production model of Rein and Seghal.[52] (See Appendix A) The M.C. events were processed through the same analysis chain as the data. This results in 6518 e-like events (of which 5723 are CC events) and 7192 mu-like events (of which 7015 are charged-current events) for the IMB cuts.

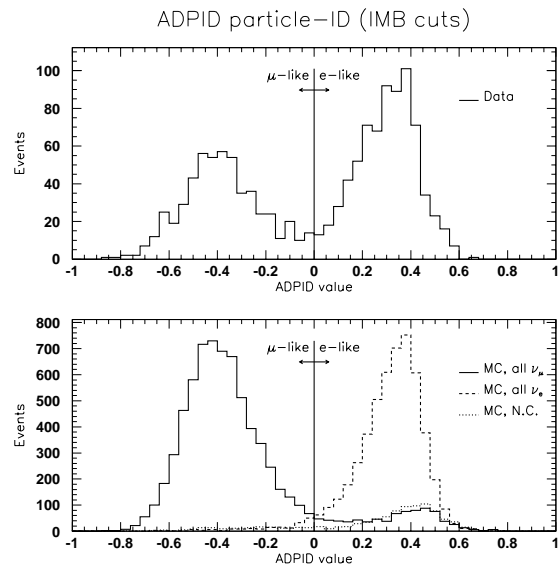


Figure 4.15: Adpid particle-ID distributions for data and MC, IMB cuts.

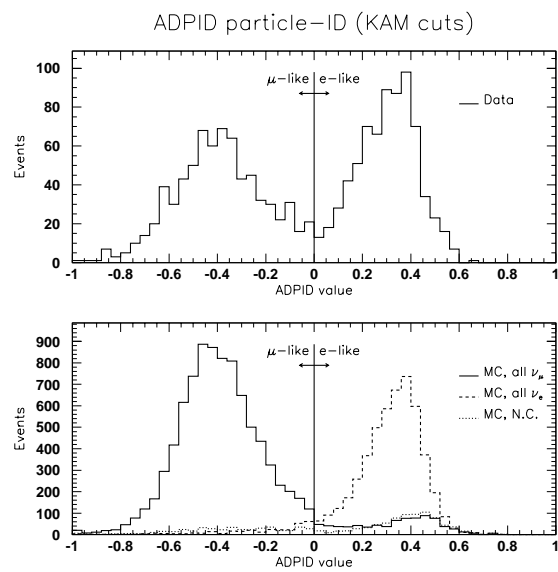


Figure 4.16: Adpid particle-ID distributions for data and MC, KAM cuts.

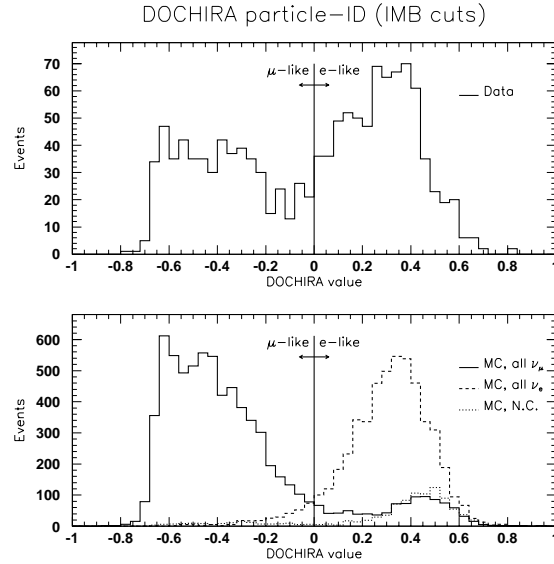


Figure 4.17: Dochira particle-ID distributions for data and MC, IMB cuts.

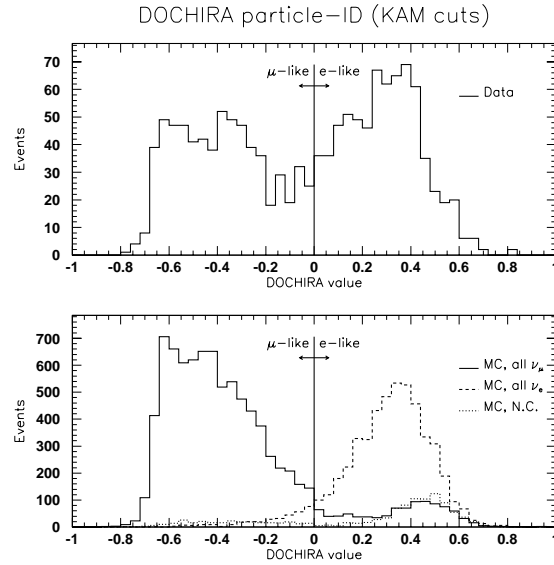


Figure 4.18: Dochira particle-ID distributions for data and MC, KAM cuts.

The fraction of  $\mu$ -like events in the data in this momentum range is  $42.5 \pm 1.3(\text{stat})\%$ , while for the monte carlo sample it is  $53.5 \pm 0.4(\text{stat}) \pm 5(\text{syst})\%$ . This leads to a double ratio  $R = \frac{(\mu\text{-like}/e\text{-like})_{\text{Data}}}{(\mu\text{-like}/e\text{-like})_{\text{MC}}} = 0.64 \pm 0.04(\text{stat}) \pm 0.06(\text{syst})$ . In com-

parison, IMB found  $36 \pm 2(\text{stat}) \pm 5(\text{syst})\%$  versus  $51 \pm 1(\text{stat}) \pm 5(\text{syst})\%$ , [21], or  $R = 0.54 \pm 0.05 \pm 0.07$ .

In the range of momentum cuts, the fraction of events with at least one associated decay is  $29.8 \pm 1.3(\text{stat})\%$ , while from the monte carlo a fraction of  $35.9 \pm 0.4(\text{stat}) \pm 0.3(\text{syst})\%$  is expected.

Applying cuts in the Kamiokande style, and calculating the double-ratio  $R$  thereby, it is found that  $R = \frac{(\mu\text{-like}/e\text{-like})_{Data}}{(\mu\text{-like}/e\text{-like})_{MC}} = 0.65 \pm 0.04(\text{stat}) \pm 0.06(\text{syst})$ . This is in good agreement with the onsite analysis.[53]

The above  $R$  values are derived using *adpid*. As a check, *dochira* is also applied. From the greater cross-over, a few percent higher double ratio is expected from *dochira*, and it is seen in  $R = 0.70 \pm 0.04 \pm 0.06$  (IMB cuts) and  $R = 0.68 \pm 0.04 \pm 0.06$  (KAM cuts).

$8.8\% \pm 1.1\%$  of the e-like events (KAM cuts) have one or more decay signals compared to the Monte Carlo prediction of  $11.2\% \pm 0.4\% \pm 0.3\%$ , where the error on the data and the first error on the Monte Carlo is statistical and the second error on the Monte Carlo is the estimated error of the muon decay detection efficiency. For  $\mu$ -like events we find  $56.6\% \pm 1.8\%$  have one or more decays and  $3.0\% \pm 0.6\%$  have two or more decays. This compares with the Monte Carlo predictions of  $55.6\% \pm 0.5\% \pm 1.7\%$  and  $3.3\% \pm 0.2\% \pm 0.1\%$  respectively.

The vertex distributions of the primary events and of the decay candidates provide information on the systematic errors due to fitting errors and due to the ratio of quasi-elastic to non-quasi-elastic events. For muon-like events with a sufficiently large energy ( $> 500\text{MeV}$ ), it is possible to discriminate between decay candidates produced at the endpoint of the muon track and those produced by pions decaying near the vertex. Figure 4.19 shows the decay vertex projected along the track for muons above 500 MeV and below 5 GeV in both data and monte carlo samples. A clear double-peaked distribution is seen: those vertices in the left peak are near the event vertex (presumably due to pions), and those in the right peak are those at the end-point of the primary muon track.

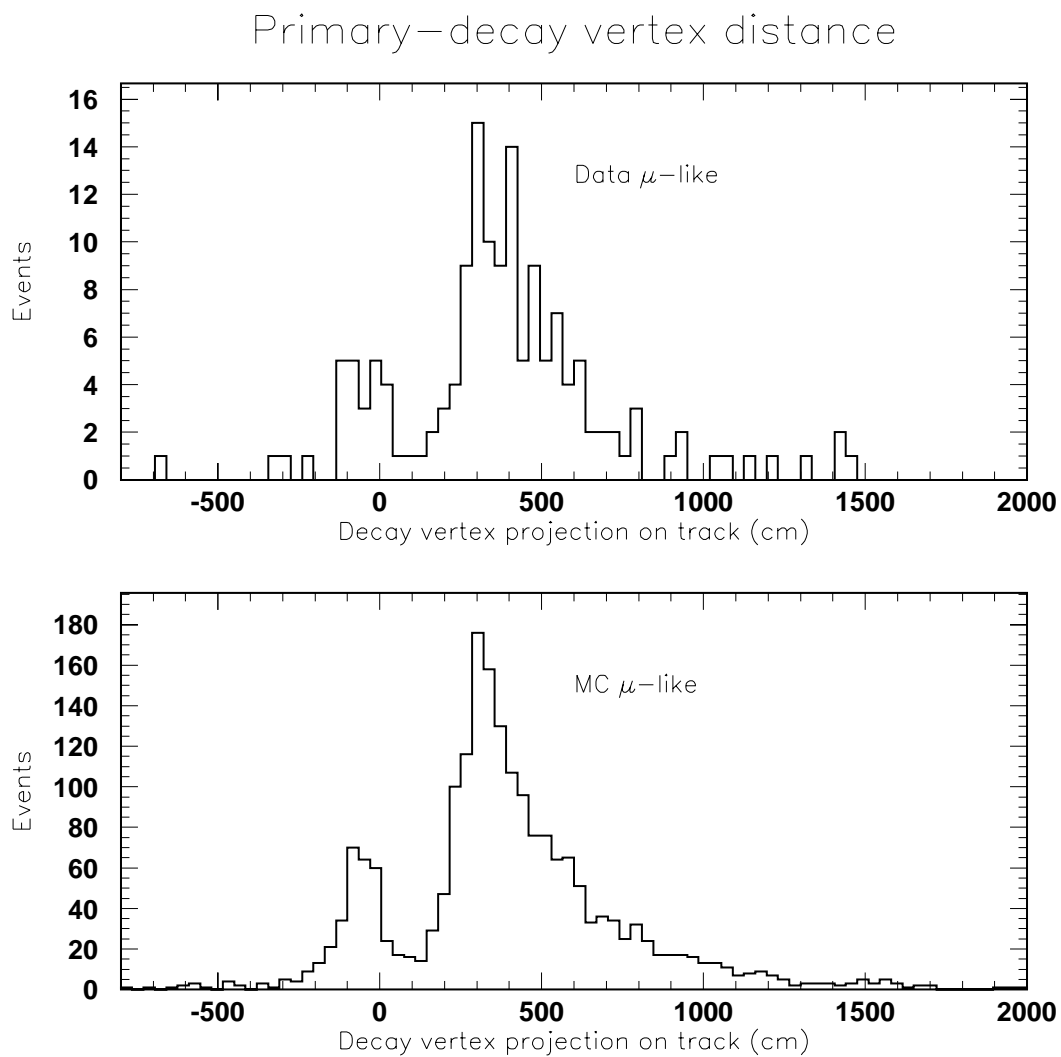


Figure 4.19: Distance along primary (yastef) track of decay (hayai) vertices for events identified as muons with  $500\text{MeV} < E_{vis} < 5\text{GeV}$ .

From the overall shift in the location of the decay vertices relative to the primary vertices, the yastef-fitted vertex is found to be pulled about 10 cm forward in real data compared to monte carlo events. This contributes 1% to the systematic in R due to the effective volume for muons changing relative to that for electrons: because muons have longer track lengths than electrons in the detector, muons with vertices near the edge of the fiducial volume which are pointing inwards can be pulled in, while those pointing outwards cannot be pushed out as much as electrons and still pass the reduction cuts.

From the ratio of the number of decay candidates in the left-hand peak to those in the right-hand peak (each candidate being inversely weighted by the number of decays in each event), the agreement between data and monte carlo in the QE/non-QE ratio for events classified as muons is  $0.7 \pm 3.1\%$ . This leads to an estimate of the systematic in R due to the QE/non-QE ratio in mu-like events of 3.2%.

From the difference in the number of electron-like events with decays found, the systematic error in R due to the ratio of quasi-elastic to non-quasi-elastic events which are counted as electrons can be estimated to be 2.7%.

The total QE/non-QE ratio contribution to the systematic error in R is then taken as 4.2%, taking the above two contributions in quadrature. (The contributions to the muon side and to the electron side are through largely non-overlapping channels – in particular, almost all of the neutral current events are counted as electrons in the monte carlo.) This agrees with a separate theoretical estimation of 3% from the uncertainty in the quasi-elastic neutrino cross-section, and 2.6% from the non quasi-elastic neutrino cross-sections, which taken in quadrature give 4.0%.

The total sources of systematic error in R are as follows: 1% from the absolute energy calibration, 1.5% from the conversion to muon momentum, 1% from fiducial volume determination, 3.1% from single-ring selection, 3.5% from particle misidentification, less than 0.5% from cosmic ray muons and other non-neutrino related backgrounds, 5% from the uncertainty in the calculation of the  $\nu_\mu/\nu_e$  ratio, 4.2% from the uncertainty in the quasi-elastic/non-quasi-elastic cross-section ratio, 2%

from the statistical error in the Monte Carlo. These errors are added in quadrature giving a total systematic error of 8.5%.

Looking at events above the sub-GeV range, the double-ratio for events in the range  $1.33 \text{ GeV} < E_{vis} < 5 \text{ GeV}$  is  $0.703 \pm 0.11(stat) \pm 0.07(syst)$ , where the total systematic error, adjusting for reduced statistics, is taken as 9.5%.

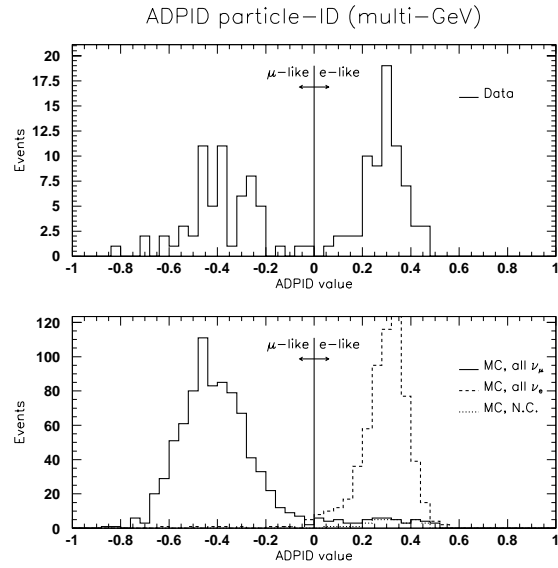


Figure 4.20: Adpid PID distributions for data and MC,  $1.5 \text{ GeV} < E_{\text{vis}} < 5 \text{ GeV}$ .

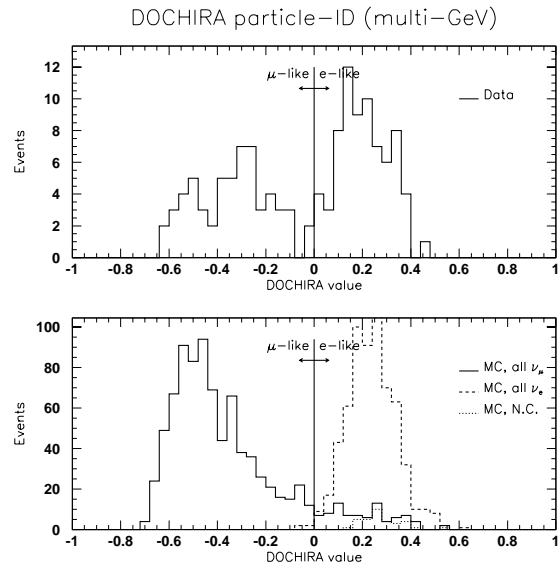


Figure 4.21: Dochira PID distributions for data and MC,  $1.5 \text{ GeV} < E_{\text{vis}} < 5 \text{ GeV}$ .

In Figure 4.22 is presented the volume fraction versus numbers of events, for both all events and those with a muon decay. In Figure 4.23, are the same quantities for single ring events and those with a muon decay. The volume fraction plot shows data in successively larger concentric shells of equal volume, zero being the innermost. This tests the data for systematic effects which might be due to proximity to the detector boundary.

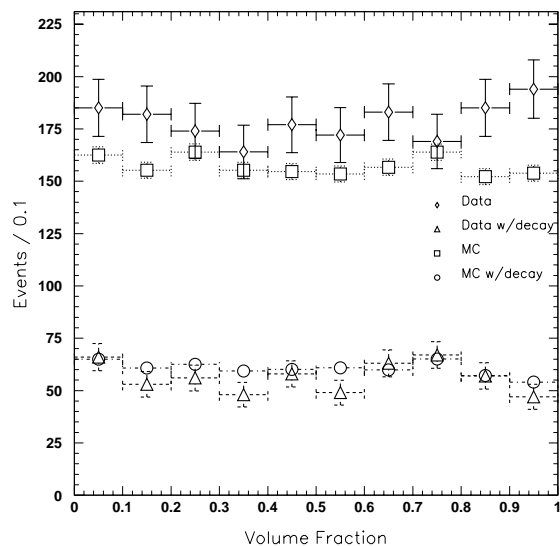


Figure 4.22: Fiducial volume distribution of all events and those with a mu decay.

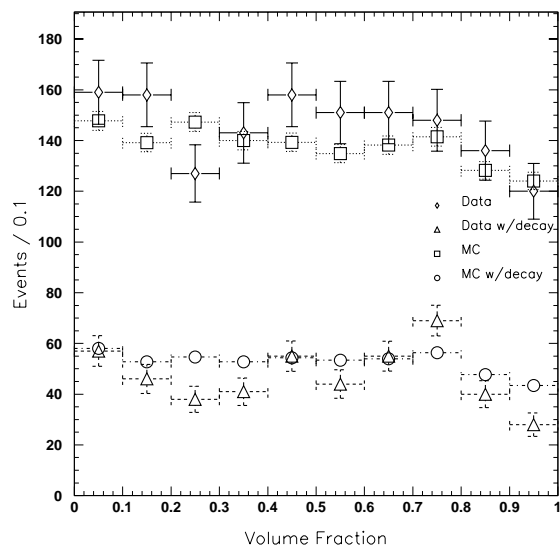


Figure 4.23: Fiducial volume distribution of single-ring events and those with a mu decay.

The angular distribution of the  $\mu$ -like fraction of the total events is illustrated in Figures 4.24 and 4.26, for topologically identified events and those with muon decay

tags, for both data and simulation. The direction cosine is +1 for downgoing and -1 for upcoming events. A trend towards more muon deficit in the lower hemisphere is visible.

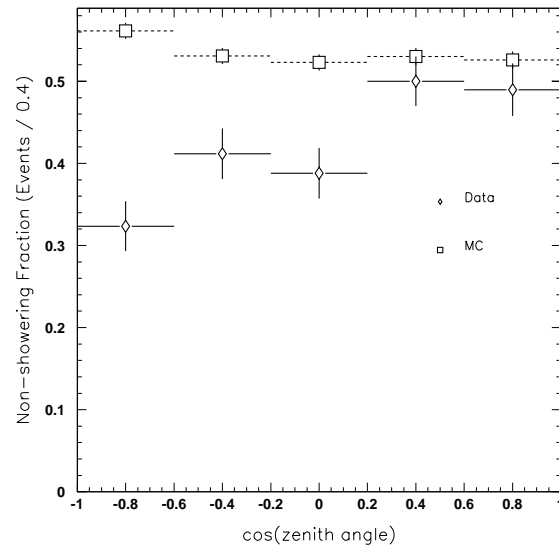


Figure 4.24:  $\mu$ -like fraction vs zenith angle, 2-meter fiducial cut.

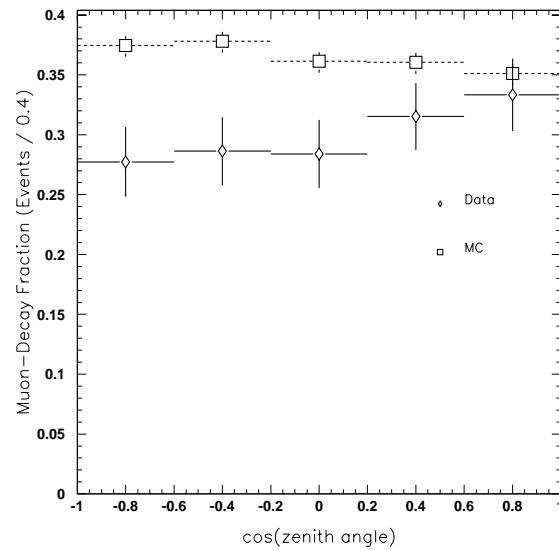


Figure 4.25: Muon-decay fraction vs zenith angle 2-meter fiducial cut.

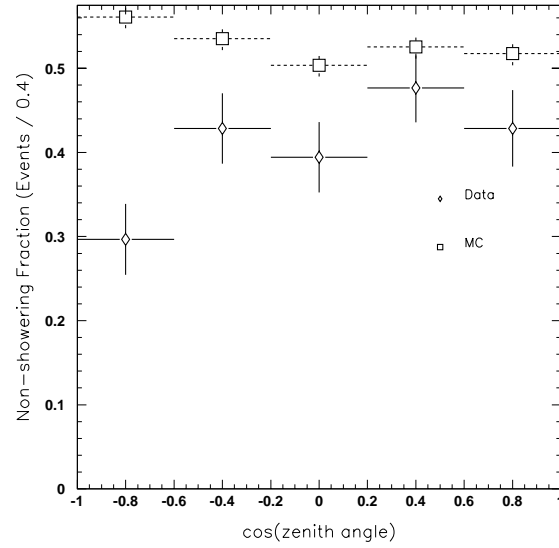


Figure 4.26:  $\mu$ -like fraction vs zenith angle 5-meter fiducial cut.

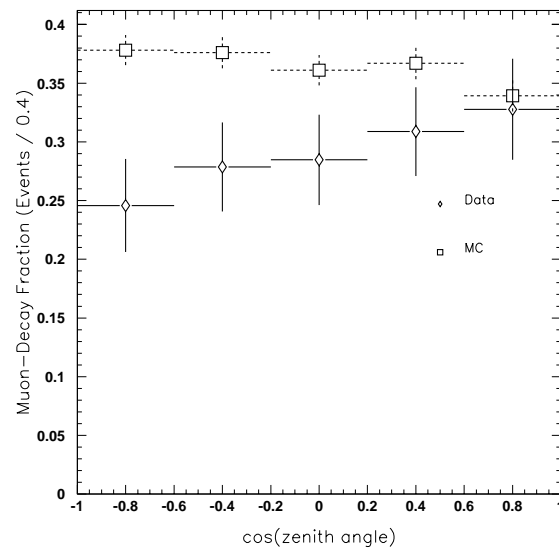


Figure 4.27: Muon-decay fraction vs zenith angle 5-meter fiducial cut.

Finally the muon-like and decay fractions plotted with respect to momentum are presented in Figures 4.28 and 4.29.

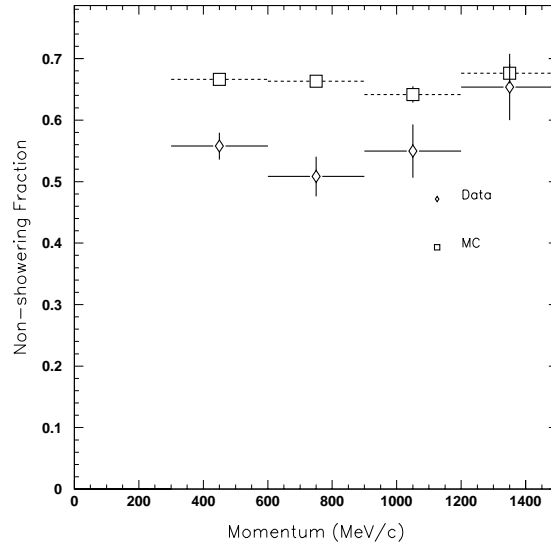


Figure 4.28:  $\mu$ -like fraction vs momentum.

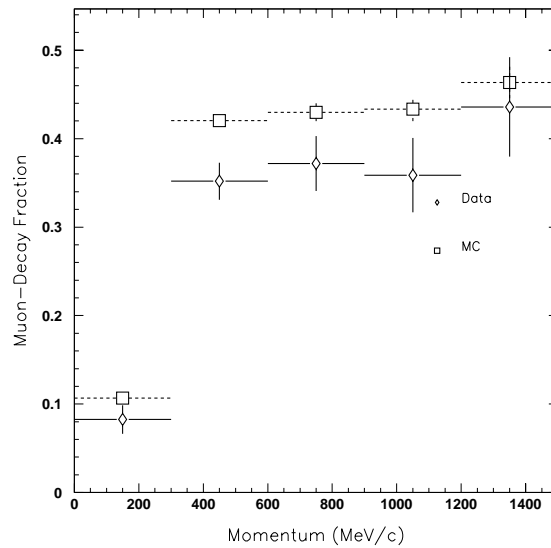


Figure 4.29: Muon-decay fraction vs momentum.

### 4.3.1 Comparison of Analyses

The collaboration conducted two independent series of data reduction, event fitting, and monte carlo simulation. Both analyses used the same data set calibrated in terms of photoelectrons and time, proceeding with independent application of conversions to energy (which involve interpretation of calibrations and such things as corrections for water transparency, etc.) and all further selections, fitting and interpretations. The results are consistent with each other and with the previous IMB and Kamiokande experiments, and confirm that the atmospheric neutrino anomaly persists.

## 4.4 Interpretation

Since Kamiokande, IMB and other experiments reported anomalously low ratios of muon-like events to electron-like events 10 years ago, there have been a number of models proposed to explain the phenomenon, ranging from contamination by neutrons from the surrounding rock [54,55] to contamination by proton decay (ironic, since atmospheric neutrinos were originally studied as background for proton-decay searches). The first of these objections was answered by Kamiokande, where they showed that the pions produced by neutron interactions are identifiable and not clustered near the walls as would be expected.[56] The second would imply that the anomalous ratio of ratios would not extend above the rest mass of the proton; the multi-GeV ratio is, however, still below expectation. A most serious possibility is that of an error in the calculation of atmospheric neutrino fluxes – this one cannot easily be ruled out, despite the agreement between different flux models.

Assuming the flux model is right, one of the most persistent proposals, predating any of the neutrino flux anomalies, is the possibility that if neutrinos have non-zero mass, their flavor (weak) eigenstates need not be the same as their mass eigenstates, and hence they can oscillate from one type to another in flight. There are several models in circulation, some of which will be discussed below, but the general scheme

can be represented by the simplest case of two-flavor mixing, for example between  $\nu_\mu$  and  $\nu_\tau$ , where the flavor eigenstates are related to the mass eigenstates by:

$$\begin{pmatrix} \nu_\mu \\ \nu_\tau \end{pmatrix} = \begin{pmatrix} \cos\theta & \sin\theta \\ -\sin\theta & \cos\theta \end{pmatrix} \begin{pmatrix} \nu_2 \\ \nu_3 \end{pmatrix},$$

where  $\theta$  is the mixing angle between the mass eigenstates and the weak eigenstates. (This use of subscripts “2” and “3” for the mass eigenstates involved in  $\nu_\mu$ - $\nu_\tau$  oscillations is conventional. Had it been  $\nu_e$ - $\nu_\mu$ , the corresponding mass subscripts would have been “1” and “2.”) The mass eigenstates propagate as:

$$i \frac{d}{dt} \begin{pmatrix} \nu_2 \\ \nu_3 \end{pmatrix} = \begin{pmatrix} E_2 & 0 \\ 0 & E_3 \end{pmatrix} \begin{pmatrix} \nu_2 \\ \nu_3 \end{pmatrix},$$

which leads to a  $\nu_\mu$  survival probability of:

$$P_{\mu\mu} = 1 - \sin^2(2\theta) \sin^2\left(\frac{1.27\delta m_{23}^2 L}{E}\right),$$

where the neutrino energy  $E$  is in MeV, the distance travelled  $L$  is in meters, and the  $\delta m^2$  is measured in  $eV^2$ .

The notable features of this expression are that first, the overall magnitude of the oscillations is set by  $\sin^2 2\theta$ , and that second, the energy  $E$  at which oscillations set in (for a given pathlength  $L$ ) is determined by  $\delta m^2$ . The case of  $\sin^2 2\theta = 1$  ( $\theta = 45$  deg) is referred to as “maximal mixing.”

The above formalism can be generalized to three flavors; this requires the use of two mass-squared differences (the third being determined by the first two) and three mixing angles. Here, only the two-flavor models are considered.

In order to discriminate between competing models, two useful metrics from the data are the “ratio-of-ratios” of relative flux rates of muon- and electron-like events, and the directional asymmetries of each of these two types of event. The directional asymmetries are defined as:

$$A_\mu = \frac{D_\mu - U_\mu}{D_\mu + U_\mu},$$

$$A_e = \frac{D_e - U_e}{D_e + U_e},$$

where  $D_\mu$  is the number of downward-going muon-like events,  $U_\mu$  is the number of upward-going muon-like events, and likewise for the electron-like events.[57] “Downward-going” means  $\cos\theta < 0$ , where  $\cos\theta$  is the z-component of the momentum vector – not to be confused with the “cosmic ray” direction, which is the (opposite) direction from which the particle came.

Figure 4.30 shows the asymmetries plotted against the visible energy (electron-equivalent energy) of the single-ring data from SuperKamiokande in 10 logarithmic visible energy bins from 100 MeV to 5 GeV. The upper curve is  $A_\mu$ , while the lower one is  $A_e$ . Figure 4.31 shows the same data as a trajectory in the  $A_\mu$ - $A_e$  plane; arrows indicates the direction of increasing energy.

Figures 4.32 and 4.33 show these same quantities for the monte carlo events.

Following that are the asymmetries and asymmetry trajectories. For those models with adjustable parameters, the asymmetries shown are the results of  $\chi^2$  minimization in the asymmetries. The  $\chi^2$  function follows a formalism used in the AMY[58] and CELLO[59] experiments: a vector  $\Delta$  of residuals a matrix  $V$  of errors is constructed, with the  $V_{nn}$ th diagonal element being the  $\sigma_{total}^2$  for each measurement, and the off-diagonal element  $V_{ij}$  being the common normalization error for the  $i$ th and  $j$ th measurements. Then the minimized expression is

$$\chi^2 = \Delta^T V^{-1} \Delta.$$

Ten residuals measurements between data and monte carlo, one for each energy bin, are taken in  $A_\mu$  and likewise in  $A_e$  for a total of twenty residuals elements. The off-diagonal elements are taken as the estimated background,  $(0.2)^2$ , and it is assumed that the muon asymmetries are uncorrelated with the electron asymmetries. The on-diagonal elements are taken as the sums of the squares of the statistical errors in the data and monte carlo and the background. The detector is assumed to be up-down symmetric. In addition, a set of ten residuals in the number of muons normalized to the number of electrons ( $R(\mu/e)_{Data} - R(\mu/e)_{MC}$ ) is fit, using the non-statistical part of the systematic errors as the off-diagonal elements.

Corrections were made in the oscillation probabilities for the effects of matter on the survival probabilities due to the different effective potentials seen by different flavors as they pass through the earth. Using the parametrization of Akhmedov *et al.*, this can be treated as a changing of the effective oscillation amplitude  $\sin(2\theta)$  and  $\delta m^2$  to values depending on the number densities of electrons in the matter (for  $\nu_\mu - \nu_e$ ) or neutrons (for  $\nu_\mu - \nu_{sterile}$ ). The case of  $\nu_\mu - \nu_e$  does not require matter effects. Sterile neutrinos, if they exist, will not interact with the matter and so will have a different effective potential than muon neutrinos.

Other than that, it is very similar to  $\nu_\mu - \nu_{sterile}$ , except that neutral-current events are not oscillated away for muon neutrinos that become tau neutrinos, while they are for sterile neutrinos, because the neutral current cross-sections are the same for tau neutrino and the muon neutrino (and the electron neutrino) but are zero for sterile neutrinos. Matter effects are zero for  $\nu_\mu - \nu_\tau$ .

The results are summarized in Table 4.3. For each model, the best-fit (if the model has adjustable parameters)  $\chi^2/d.o.f$  is given for the  $\chi^2$  measured for the variation of the relevant parameters. The first two columns show the  $\chi^2/d.o.f$  and d.o.f. for the fit to the asymmetries, the second two columns show the same quantities for the fit to the ratios, and the last two columns show the results for the combined fit.

Table 4.3: Best-fit results for oscillation scenarios.

Model	$\frac{\chi_A^2}{dof}$	dof	$\frac{\chi_R^2}{dof}$	dof	$\frac{\chi_{A,R}^2}{dof}$	dof	
No oscillations	10	2.68	20	2.14	10	2.5	30
$\nu_\mu - \nu_\tau$	1	1.29	18	0.604	8	1.04	28
$\nu_\mu - \nu_e$	2	2.21	18	0.543	8	1.62	28
$\nu_\mu - \nu_{sterile}$	9	1.3	18	0.536	8	1.04	28

The best fits are for  $\nu_\mu - \nu_\tau$  and  $\nu_\mu - \nu_{sterile}$ , which have nearly the same total  $\chi^2$  and best fit points (shown in Figs. 4.36 and 4.39), but with a slightly smaller allowed region for  $\nu_\mu - \nu_{sterile}$ .

The best-fit point for  $\nu_\mu - \nu_e$  is near that for the previous two cases, but the  $\chi^2$  is much worse, primarily due to the asymmetry. However, it is still better than the no-oscillations case.

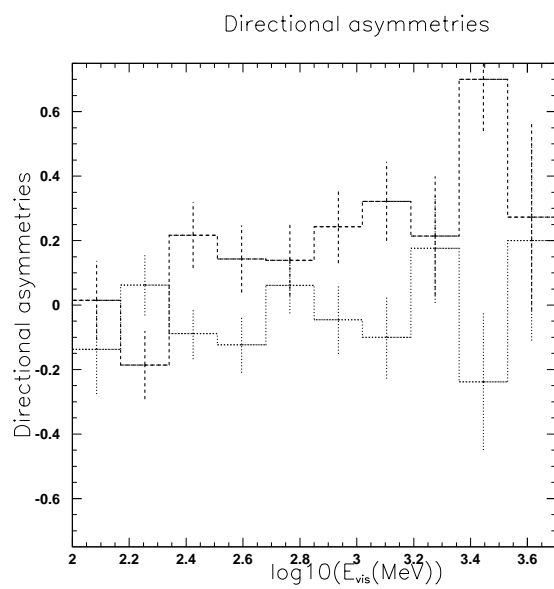


Figure 4.30: Asymmetry vs visible energy, data.

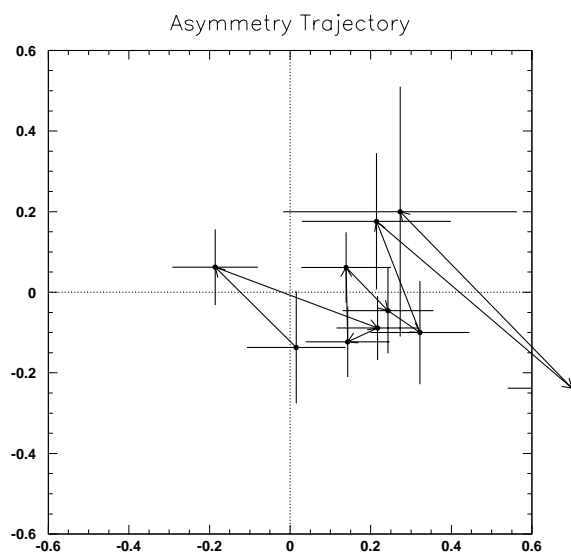


Figure 4.31: Asymmetry trajectory data.

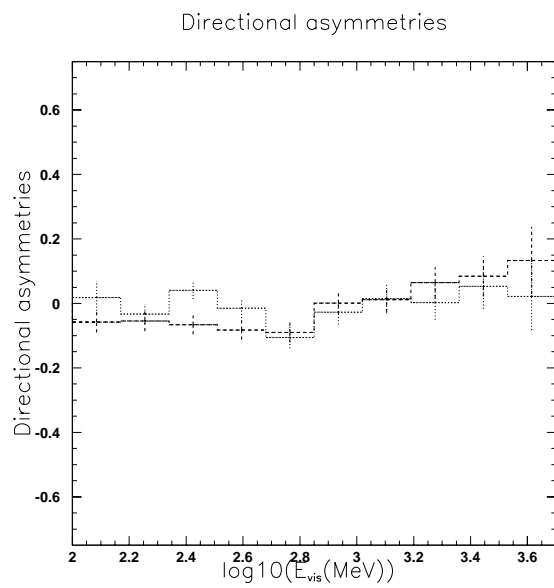


Figure 4.32: Asymmetry vs visible energy, MC with no oscillations.

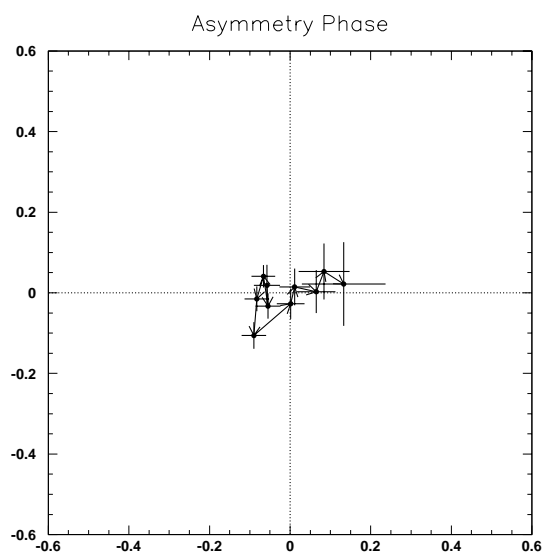


Figure 4.33: Asymmetry trajectory MC with no oscillations.

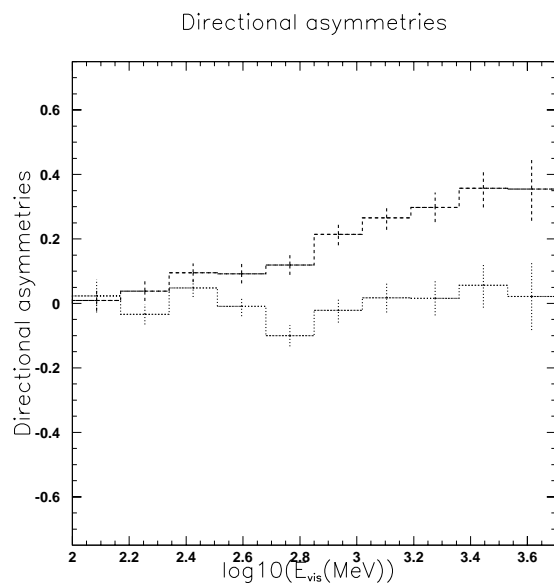


Figure 4.34: Asymmetry vs visible energy, MC with  $\nu_\mu \rightarrow \nu_\tau$  osc.

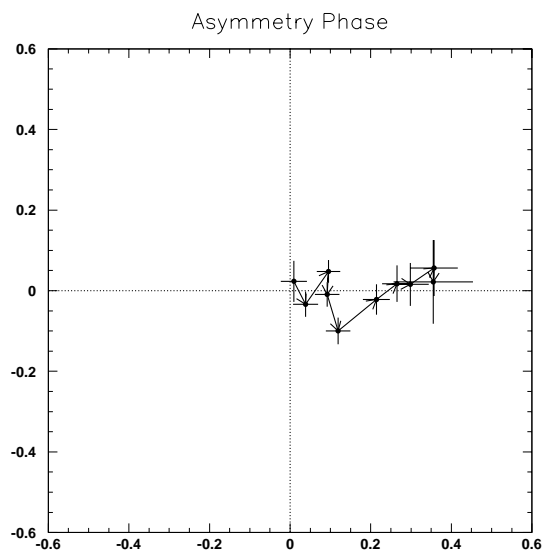


Figure 4.35: Asymmetry trajectory MC with  $\nu_\mu \rightarrow \nu_\tau$  osc.

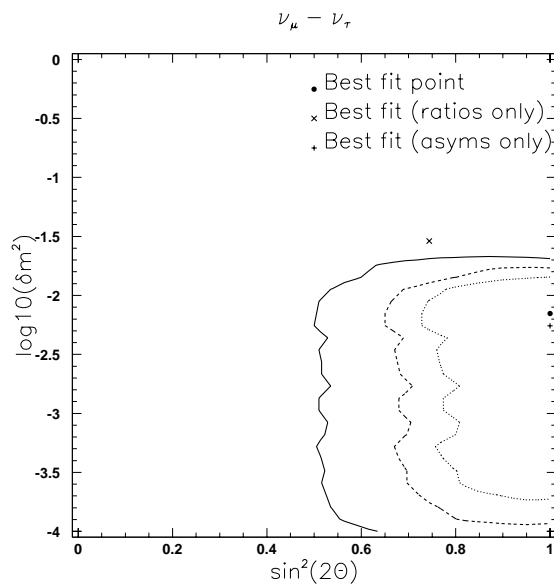


Figure 4.36: Chi-squared, MC with  $\nu_\mu \rightarrow \nu_\tau$  osc.

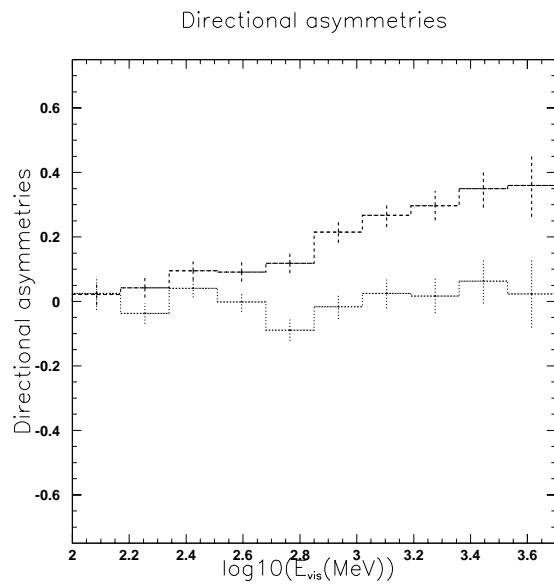


Figure 4.37: Asymmetry vs visible energy, MC with  $\nu_\mu \rightarrow \nu_{Sterile}$  osc.

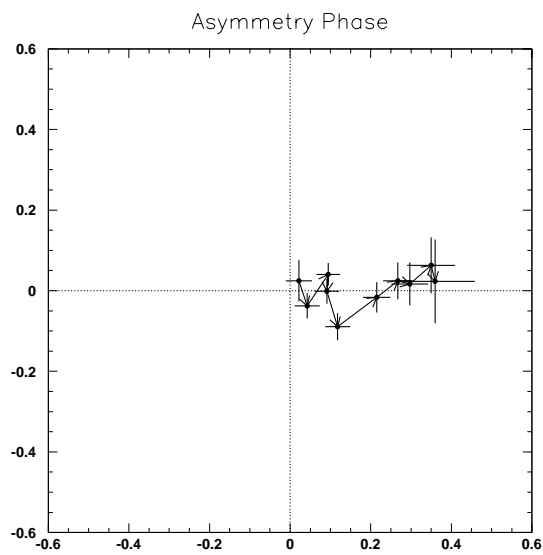


Figure 4.38: Asymmetry trajectory MC with  $\nu_\mu \rightarrow \nu_{Sterile}$  osc.

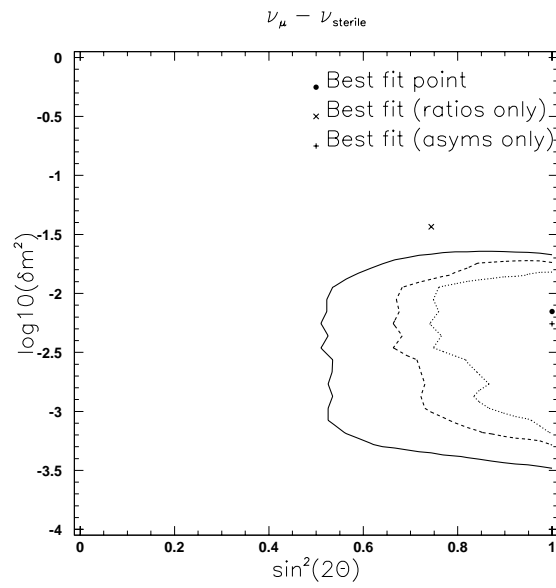


Figure 4.39: Chi-squared, MC with  $\nu_\mu \rightarrow \nu_{Sterile}$  osc.

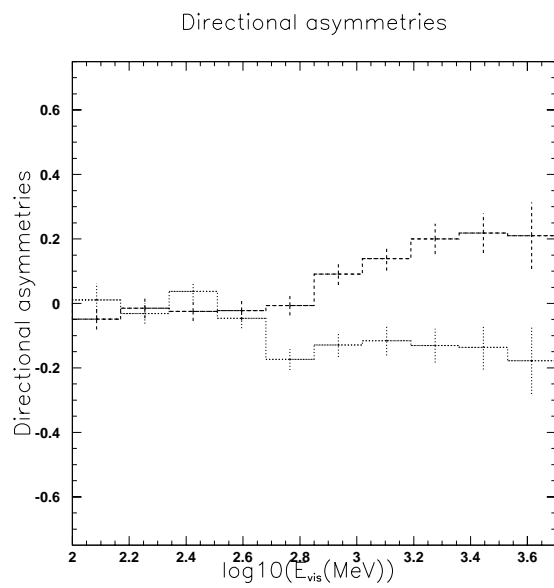


Figure 4.40: Asymmetry vs visible energy, MC with  $\nu_{\mu} \rightarrow \nu_e$  osc.

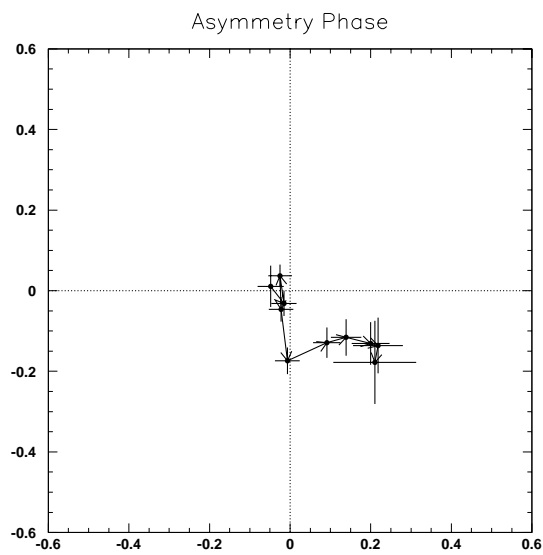


Figure 4.41: Asymmetry trajectory MC with  $\nu_{\mu} \rightarrow \nu_e$  osc.

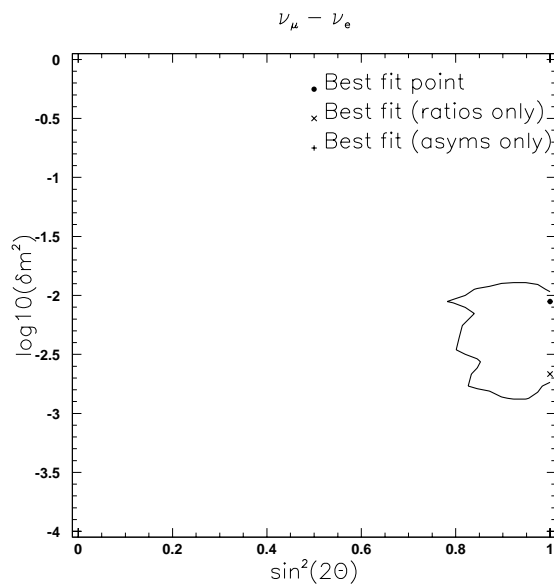


Figure 4.42: Chi-squared, MC with  $\nu_\mu \rightarrow \nu_e$  osc.

## 4.5 Conclusions

Super-Kamiokande went online at midnight, 1 April 1996, to start taking data on atmospheric and solar neutrinos, search for signs of proton decay, and monitor for supernova bursts. In its first year of operation, it has caught up to the cumulative livetime of its predecessor experiments, Kamiokande and IMB, and has been able to confirm the continued existence of the anomalous atmospheric neutrino flavor ratios reported by those experiments. In addition, it is able to gather better statistics on the angular distribution of events at energies  $>\sim 1$  GeV.

Soon, Super-Kamiokande will have enough data to more firmly indicate whether neutrino oscillations remain a viable solution to the problem, and if so at what set of parameters. In addition, it continues to take data on solar neutrinos, and will soon become the far detector for the K2K long-baseline neutrino oscillations experiment, which will aim  $\sim 1$  GeV neutrinos from the proton-synchrotron facility at KEK, 250 km away.

# Appendix A

## Monte Carlo Cross-sections

*“It is not for children.”* – Wojciech Gajewski

IMB, like Super-Kamiokande, was divided into two analysis groups: East Coast and West Coast. Each analysis group developed its own neutrino interaction model; the Super-Kamiokande offsite analysis group thus inherited two different simulation programs, which have come to be known as “IMBEast,” originally developed at the University of Michigan[60], and “IMBWest,” originally developed at UCI.[61]

Both monte carlos use the atmospheric flux calculation of Agrawal, Barr, Gaisser, Lipari and Stanev. [13,12,51] They also use common tracking code and detector model. The CERNLIB package GCALOR (version 1.03/08) is used for the propagation of the interaction products; GCALOR uses CALOR to handle most hadronic interactions, and calls on GEANT (version 3.16) to handle electromagnetic interactions, and FLUKA to handle hadronic interactions above 10 GeV.

IMBEast uses the pion-production model of Rein and, Seghal[52], while IMBWest uses one based on that of Fogli and Nardulli[62]. They agree with each other on pion-production rates to within a few percent in the sub-GeV range. The two interaction monte carlos have been modified somewhat to accommodate new values for the axial mass and Fermi momentum.

The IMBEast monte carlo has undergone more extensive updates, in particular to some of the pion-production cross-sections and its deep-inelastic cross-section calculation, which makes it preferable to IMBWest, especially in the multi-GeV range. In fact the IMBWest neutrino spectrum cuts off at 5 GeV. IMBEast is the MC used in the analysis.

The neutrino-free nucleon cross-sections used in IMB East are shown in Figure A.1.  
(Courtesy of Wojciech Gajewski.)

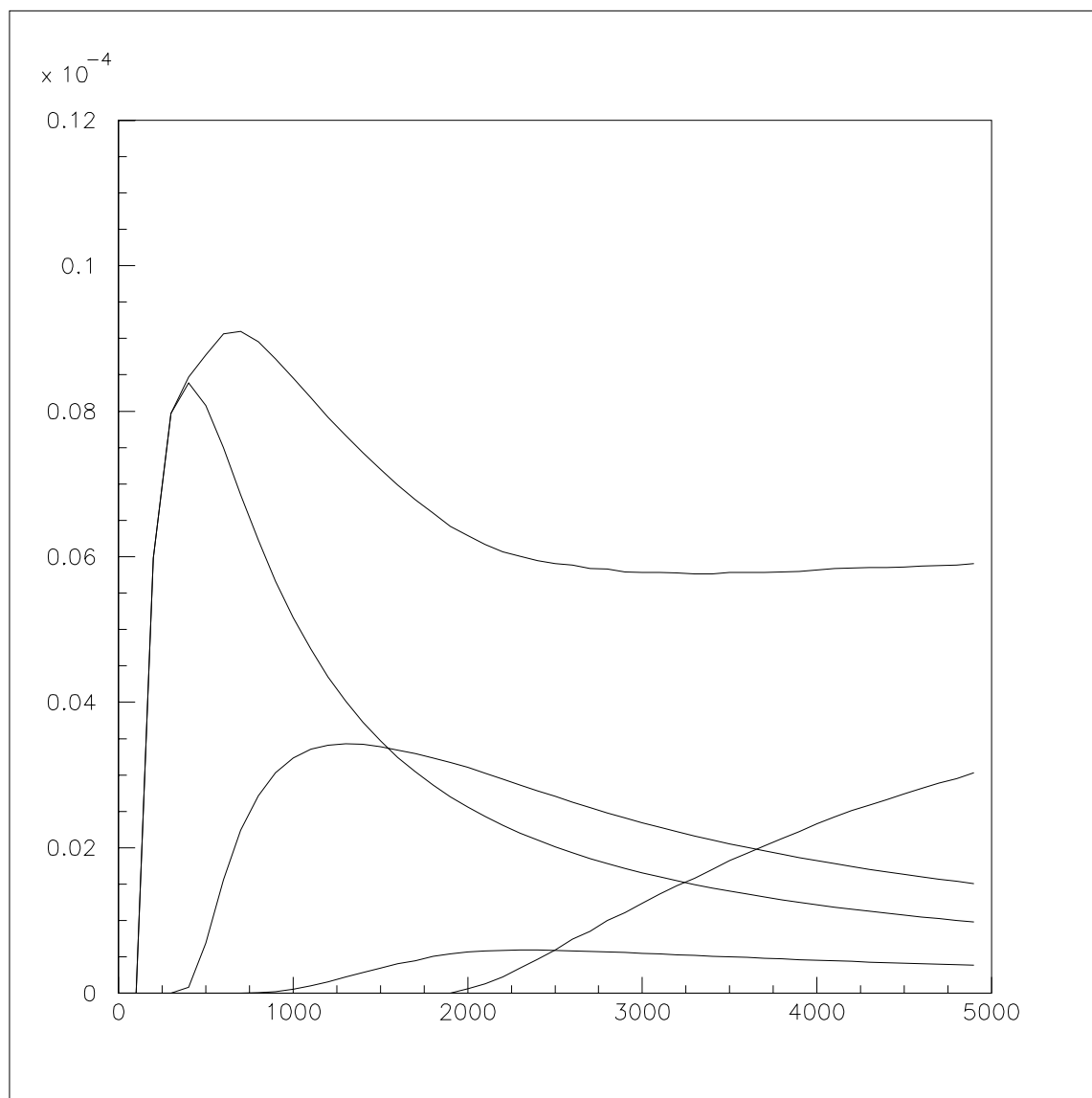


Figure A.1: IMBEast cross-sections.

# Appendix B

## The Super-Kamiokande Collaboration

**Institute for Cosmic Ray Research, University of Tokyo**

Y. Fukuda, T. Hayakawa, K. Inoue, K. Ishihara, H. Ishino,  
Y. Itow, T. Kajita, J. Kameda, S. Kasuga, Y. Koshio,  
K. Martens, M. Miura, M. Nakahata, A. Okada, M. Oketa,  
K. Okumura, M. Ota, N. Sakurai, M. Shiozawa, Y. Suzuki,  
Y. Takeuchi, Y. Totsuka (spokesman)

**National Laboratory for High Energy Physics (KEK)**

J. Kanzaki, K. Nakamura, M. Sakuda, O. Sasaki, Y. Oyama

**Bubble Chamber Physics Laboratory, Tohoku University**

K. Fujita, A. Hasegawa, T. Hasegawa, S. Hatakeyama,  
T. Iwamoto, T. Kinebuchi, M. Koga, T. Maruyama, H. Ogawa,  
M. Onada M. Saito, A. Suzuki, F. Tsushima

**Tokai University**

M. Eto, M. Koshiba, M. Nemoto, K. Nishijima

**Department of Physics, Osaka University**

A. Kusano, Y. Nagashima, M. Takita, T. Yamaguchi,  
M. Yoshida

**Niigata University**

T. Ishizuka, Y. Kitaguchi, H. Koga, K. Miyano, H. Okazawa,  
M. Takahata

**Department of Physics, Tokyo Institute of Technology**

Y. Hayato, Y. Kanaya, K. Kaneyuki, Y. Watanabe

**Gifu University**

S. Tasaka

**Miyagi University of Education**

M. Mori

**Department of Physics, Kobe University**

S. Echigo, M. Kohama, A.T. Suzuki

**Institute for Nuclear Study, University of Tokyo**

K. Chikamatsu, E. Ichihara, T. Inagaki, K. Nishikawa,  
A. Sakai

**Boston University**

M. Earl, A. Habig, E. Kearns, S.B. Kim, M. Messier,  
J.L. Stone, K. Scholberg, L.R. Sulak

**Brookhaven National Laboratory**

M. Goldhaber

**University of California, Irvine**

T. Barszczak, W. Gajewski, P.G. Halverson, J. Hsu,  
L.R. Price, W.R. Kropp, F. Reines, H.W. Sobel

**California State University, Dominguez Hills**

K. Ganezer, W. Keig

**George Mason University**

R.W. Ellsworth

**University of Hawaii**

J. Flanagan, J.G. Learned, S. Matsuno, V. Stenger,  
D. Takemori

**Los Alamos National Laboratory**

T.J. Haines

**Louisiana State University**

E. Blaufuss, R. Sanford, R. Svoboda, M.R. Vagins

**University of Maryland**

M.L. Chen, Z. Conner, J.A. Goodman, G. Sullivan

**State University of New York, Stony Brook**

J. Hill, C.K. Jung, C. Mauger, C. McGrew, B. Viren,  
C. Yanagisawa

**University of Warsaw**

D. Kielczewska

**University of Washington**

J. George, A. Stachyra, L. Wai, J. Wilkes, K. Young

# Appendix C

## Author

The author joined the Super-Kamiokande collaboration in the fall of 1993. The Kamiokande and IMB collaborations, from which the core of the Super-Kamiokande collaboration was formed, were at that time preparing to do a study of the particle identification capabilities of water Cherenkov detectors [35,36], since that had been a point of controversy when those collaborations had published their measurements of the atmospheric neutrino composition. To accomplish this a 1 kton “mini-Kamiokande” tank was built at the end of the K6 proton-synchrotron beamline at the KEK National Accelerator Laboratory in Tsukuba, Japan. This provided a set of particles of known type (electron, muon, pion) and energy (0.1 to 1 GeV), with which the instrumentation and algorithms of Kamiokande and IMB could be tested. The tank was first instrumented with DAQ and PMTs of the type used in Kamiokande, and then with the those of IMB. In the fall of 1993, the author inherited from Gary McGrath (who had graduated in August) the task of resurrecting the laser calibration system from IMB, and went to KEK in 1994 to install it and to work on the construction, calibration, data-taking and decommissioning of the IMB part of the beam-test, which occupied most of the year. While there, he also made a detailed study of the documentation for the DAQ system then in development for the Super-Kamiokande inner detector, which provided a necessary basis of understanding for the design of an outer-detector DAQ (by other US institutions), which could be integrated with it.

In early 1995, he worked on the design of the laser calibration system for Super-Kamiokande, which needed to be much more elaborate than those used in IMB and Kamiokande. Because of the geometry and narrowness of the outer detector, ultimately 52 separate optical fibers needed to be run to various positions throughout

the outer detector volume, in addition to the one for the inner detector. IMB had no outer detector and Kamiokande didn't calibrate theirs to the degree that was needed for Super-Kamiokande. (Kamiokande vetoed on the basis of a global hitsum of the outer-detector tubes. For Super-Kamiokande, a more detailed read-out was desired in order to speed up the job of finding cosmic ray entry points, and in order to be able to confirm whether suspected partially contained events really exited the inner-detector volume.) The job of procuring fibers and making diffuser balls was allocated to UM (Zoa Conner), while that of designing and procuring the rest of the system (laser, light distribution system, DAQ hardware and software) was allocated to UH (the author).

In the spring of 1995, the author took up position at the mine in Kamioka, representing UH (and for the first couple of months, the US) for the duration of preparation, construction and most of the first year of data-taking. The equipment installation and preparations for the it lasted a bit more than a year, until April 1996 when the detector turned on. Besides working on the installation and testing of outer-detector photo-tubes, the author also worked on the installation of the laser fibers to all parts of the outer detector, the development, installation and testing of the laser, optical switches, and laser calibration DAQ, various other mechanical and logistical problems, and the usual crises that come up in a construction project of that size. During the tank-filling phase in January and February of 1996, the author even had to make use of his scuba-diving license in order to fix several mechanical problems that had arisen underwater.

At the end of construction and the beginning of data-taking, besides working on construction and calibration, the author wrote the code to convert the outer-detector data from raw format to calibrated format, added several features to the event display program (especially those concerned with monitoring the performance of the detector), fixed the PMT location map for the outer detector, and worked on characterizing and debugging the performance of the detector generally.

By the end of the summer of 1996, with the stabilization of the detector, the author concentrated on the analysis of the data with the offsite high-energy group, working

on mu-decay (afterdk), particle ID (dochira), early studies of the absolute energy calibration, event-scanning, characterizing the differences between the two offsite monte carlos, and other data-quality studies. The author also wrote the first drafts of the offsite-analysis and detector sections of the high-energy group's sub-GeV atmospheric neutrino paper. A track fitter that he wrote became the basis for a muon fitter developed for the upward-going muon analysis by Shigenobu Matsuno.

The author was born in Massachusetts in 1964, and grew up in Vermont. After attending high schools in Vermont, Massachusetts and Winchester, England, he majored in Physics and Astronomy at Harvard University, where the topic of his undergraduate thesis was the temperature distribution of the Perseus cluster of galaxies, under the tutelage of Dr. Christine Jones. After graduating in 1987, he worked as research assistant and then as programmer for the Extreme Ultraviolet Explorer satellite at UC Berkeley, as part of the team developing the analysis suite which generated skymaps and point-source fluxes in real-time from the satellite telemetry. In 1992, he began graduate studies at UH, and worked part-time on cable stress (snap-loading) simulations for the deployment of the DUMAND undersea neutrino detector project under Dr. John Learned. (That project ultimately faced too many technical difficulties and was terminated, though they did leave a legacy of solutions to some of the great and unusual problems of deep-ocean experimentation, which have been put to use by marine researchers in other fields.)

In the fall of 1997, the author married Mika Masuzawa, whom he had met while she was working as a post-doc on Super-Kamiokande and who is now working for the accelerator division at KEK. At the end of 1997 he will be joining her there on a JSPS fellowship for two years.

# Bibliography

- [1] W. Pauli, *Handbuch der Physik*, Berlin, (1933).
- [2] E. Fermi, *Z. Physik*, **88**, 161 (1934).
- [3] F. Reines, C.L. Cowan, Jr., *Science* **124**, 3212 (1956).
- [4] F. Reines, C.L. Cowan, Jr., *Phys. Rev.* **90**, 492 (1953).
- [5] F. Reines, C.L. Cowan, Jr., *Phys. Rev.* **92**, 830 (1953).
- [6] G. Danby *et al.*, *Phys. Rev. Lett.* **9**, 36 (1962).
- [7] M.L. Perl *et al.*, *Phys. Rev. Lett.* **35**, 1489 (1975).
- [8] T.K. Gaisser, F. Halzen and T. Stanev, *Physics Reports* **258**, 173 (1995).
- [9] M. Honda *et al.*, *Phys. Rev.* **D52**, 4985 (1995).
- [10] M. Honda *et al.*, *Phys. Lett.* **B248**, 193 (1990).
- [11] H. Lee and Y.S. Koh, *Nuovo Cimento* **105B**, 883 (1990).
- [12] G. Barr, T.K. Gaisser, and T. Stanev, *Phys. Rev. D* **39**, 3532 (1989).
- [13] V. Agrawal, T.K. Gaisser, P. Lipari, and T. Stanev, *Phys. Rev. D* **53**, 1314 (1996).
- [14] T.K. Gaisser, M.Honda, K.Kasahara, H.Lee, S.Midorikawa, V.Naumov, and T.Stanev, *Phys. Rev.* **D54**, 5578 (1996).
- [15] F. Reines *et al.*, *Phys. Rev.* **D4**, 80 (1971).
- [16] M.R. Krishnawamy *et al.*, *Proc. Roy. Soc. Lond.* **323**, 489 (1971).
- [17] T.J. Haines, *et al.*, *Phys. Rev. Lett.* **57**, 1986 (1986).
- [18] R. Becker-Szendy *et al.*, *Phys. Rev. D* **46**, 3720 (1992).
- [19] T. Kajita *et al.*, *Frontiers of Neutrino Astrophysics*, Proceedings of the International Symposium on Neutrino Astrophysics, Takayama/Kamioka, Japan, 1992, edited by Y. Suzuki and K. Nakamura (Universal Academy Press, Tokyo, 1993), p. 293.
- [20] R. Becker-Szendy *et al.*, *Phys. Rev. D* **46**, 3720 (1992).
- [21] D. Casper *et al.*, *Phys. Rev. Lett.* **66**, 2561 (1991).
- [22] K.S. Hirata *et al.*, *Phys. Lett.* **B205**, 416 (1988).

- [23] K.S. Hirata *et al.*, Phys. Lett. **B280**, 146 (1992).
- [24] Ch. Berger *et al.*, Phys. Lett. **B227**, 489 (1989).
- [25] Daum *et al.*, *Z. Phys.* **C66**, 417 (1995).
- [26] M. Aglietta *et al.*, *it Europhysics Letters*, **8**, 611 (1989).
- [27] D.M. Roback, Ph.D. Thesis, U. Minnesota (1992).
- [28] M. Goodman (Soudan 2 Collaboration), ICRC, (1997), p. 77.
- [29] M. Mori *et al.*, *Proceedings of Hawaii AGN meeting*, (1992).
- [30] M.M. Boliev *et al.*, *Proceedings of Neutrino Telescopes*, (1991), p.235.
- [31] C. Okada, preprint for the MACRO collaboration, presented at DPF in Minneapolis, August 1996 (BU, 1996).
- [32] R. Becker-Szendy *et al.*, Phys. Rev. Lett. **69**, 1010 (1992).
- [33] W. Frati, T.K. Gaisser, A.K. Mann, and Todor Stanev, preprint UPR-0218E (1992).
- [34] W.A. Mann, T. Kafka, and W. Leeson, Phys. Lett. **B291**, 200 (1992).
- [35] A.Sakai, Ph.D. Thesis, University of Tokyo (1997).
- [36] J.Breault, Ph.D. Thesis, University of California at Irvine (1997).
- [37] A. Suzuki *et al.*, NIM **A329**(1993) 299.
- [38] Toshiba K.K., *ATM TKO Module*, company manual, (1992).
- [39] M. Shiozawa, Master's Thesis, University of Tokyo, (1994).
- [40] *TKO Specifications*, KEK Report 85-10, (1985).
- [41] T. Hayakawa, *TKO GONG Shiyousho*, TKO GONG specifications, (internal document) (1993).
- [42] J. Flanagan, M. Masuzawa, Study of the Super-Kamiokande Inner Detector Front End Electronics, Super-Kamiokande memo (1995)
- [43] R. Becker-Szendy *et al.*, *Calibration of the IMB Detector*, NIM **A326**, 1 (1994).
- [44] C.McGrew, Ph.D. Thesis, University of California at Irvine (1994).
- [45] Particle Data Group, Phys. Rev. **D50**, 1173 (1994).
- [46] T.Suzuki, D.F.Measday, and J.P.Roalsvig, Phys. Rev. **C 35**, 2212 (1978).
- [47] Z.Conner, Ph.D. Thesis, University of Maryland (1997).
- [48] M. Yamada *et al.*, Phys. Rev. D **D 44**, 617 (1991).

- [49] F. Goebel, Master's thesis, SUNY Stony Brook (1996).
- [50] Y. Fukuda *et al.*, Phys. Lett. **B335**, 237 (1994).
- [51] T.K. Gaisser, private communication to Super-Kamiokande collaboration (1996).
- [52] D. Rein and L.M. Seghal, Ann. Phys. **133**, 79 (1981).
- [53] Superkamiokande Collaboration, "Measurement of a small atmospheric neutrino  $\nu_\mu/\nu_e$  ratio," in preparation.
- [54] O.G. Ryazhskaya, JETP Lett. **60**, 617 (1994).
- [55] O.G. Ryazhskaya, JETP Lett. **61**, 237 (1995).
- [56] Y.Fukuda *et al.*, submitted to Phys. Rev. Lett (1996)
- [57] J.Flanagan, J.G. Learned, S. Pakvasa, "Up-down asymmetry: A diagnostic for neutrino oscillations," (submitted to *Phys. Rev. D* September 1997).
- [58] T.Mori, Ph.D. Thesis, University of Rochester (1988).
- [59] H.-J.Behrend *et al.*, Phys. Lett. **B183**, 400 (1987).
- [60] D.Casper, Ph.D. Thesis, University of Michigan (1990).
- [61] T.Haines, Ph.D. Thesis, University of California at Irvine (1986).
- [62] G.L. Fogli and G. Nardulli, Nucl. Phys. **B160** 116(1979).